GALACTIC PROPAGATION OF COSMIC RAYS

Driaan Bisschoff

Galactic propagation of cosmic rays

Driaan Bisschoff

20056950

Dissertation submitted in partial fulfillment of the requirements for the degree *Master of Science in Physics* at the Potchefstroom Campus of the North-West University

Supervisor: **Prof. M. S. Potgieter**

Co-supervisor: **Dr. I. Büsching**

Potchefstroom

December 2011

Abstract

The widely used steady-state, rotational symmetric models (2D models) of cosmic ray (CR) propagation, assume smeared-out sources, which do not necessarily result in the same local CR flux as the real local point sources. This suggests that the 2D models may not be adequate to describe the CR primary component originating from point-like CR sources. By means of 3D time-dependent calculations, it has been shown that the secondary CR component is not affected by local point-like sources. When working with 2D models, concentrating on secondary, tertiary and higher CR nuclei may thus yield a better description of galactic CR propagation, as the flux of these nuclei does not depend on the local source history. Taking advantage of this fact and looking at CR primaries and secondaries separately, evidence of nearby CR point sources might be found with a 2D code. Conducting a parameter study, this should be seen in the different best fit values for CR primaries and secondaries. The 2D version of the GALPROP code was adapted to a compute-cluster environment using the MPI framework and used to perform parameter studies comparing CR spectra with mainly primary and secondary CR data separately. The force field approximation was implemented to account for heliospheric modulation. At Earth the approximation is valid, as only nuclei are studied and time-dependence is not considered, thus the disadvantages of the force field are largely avoided. Using the GALPROP code to model CR propagation through the Galaxy, three of the parameters in the 2D plain diffusion model were varied in the parameter study: the source spectral index (α), the spectral index of the diffusion coefficient (δ) and the magnitude of the diffusion coefficient at particle rigidity 4 GV (K_0). The LIS produced by the models were compared to experimental CR data by means of a χ^2 test. For each set of data from different experiments, the LIS was inferred using the force field approximation and the individual CR species were divided up into three groups according to the fraction of secondary and primary nuclei in each. The parameter values for the best fit models were found to differ between these Primary, Mixed and Secondary CR component groups. The secondary CRs were found to be more easily fit to data than the Primary component or the Mixed component group, implying that the 2D GALPROP model as used is indeed better suited for CR secondaries than for primaries. The results, together with the manner in which the 2D model handles CR sources, imply that there maybe local point sources of CRs that, so far, are not being taken into account.

Opsomming

Rotasie-simmetriese modelle (2D-modelle) vir die voortplanting van kosmiese strale (KS) in die Galaksie onder die aanname van 'n stasionêre toestand, neem gewoonlik net die egalige verspreiding van KS-bronne in ag. Dit gee egter nie noodwendig dieselfde vloed van KS as wanneer 'n meer realistiese beskrywing van lokale puntbronne gebruik word nie. Dit dui daarop dat 2D-modelle waarskynlik nie voldoende is vir die beskrywing van die primêre komponent van KS wat voortspruit uit 'n puntbronverdeling van KS nie. Dit is deur middel van 3D-tydsafhanklike berekeninge bepaal dat die sekondêre komponent van KS nie beïnvloed word deur meer plaaslike puntagtige bronne nie. Dit is dus moontlik dat wanneer met 2D-modelle gewerk word, waar die fokus op sekondêre, tersiêre en hoër-orde KS-kerne is, 'n beter beskrywing van die voortplanting van galaktiese KS verkry word, want die intensiteit van hierdie kerne hang nie af van die plaaslike bronne se geskiedenis nie. Met dit in ag geneem en deur afsonderlik te kyk na primêre en sekondêre KS, kan leidrade vir die bestaan van naby geleë KS-puntbronne gevind word deur 2D-modelle te gebruik. Indien 'n parameterstudie gedoen word, behoort leidrade gevind te word in die interpretasie van verskeie beste passingswaardes vir primêre en sekondêre KS. Die beskikbare 2D-weergawe van die bekende GALPROP numeriese program is vir hierdie studie aangepas vir gebruik in 'n rekenaarkluster-omgewing met behulp van die 'MPI' raamwerk. Dit is gebruik om parameterstudies uit te voer wat KS-spektra afsonderlik vergelyk met primêre en sekondêre KS-data. Daarmee saam is die kragveld-benadering vir heliosferiese modulasie geïmplementeer wat vir modulasie by die Aarde geldig is, omdat net KS-kerne bestudeer word en tydsafhanklikheid nie oorweeg word nie. Sodoende word die nadele van hierdie benadering grootliks vermy. Die voortplanting van KS deur die Melkweg is bestudeer deur gebruik te maak van die GALPROP-model. Vir hierdie modelleringstudie is drie van die parameters in die eenvoudige 2D-diffusiemodel verander, naamlik: Die bronspektraal-indeks (α), die spektraal-indeks van die diffusiekoëffisiënt (δ) en die grootte van die diffusiekoëffisiënt vir 'n deeltjiestyfheid van 4 GV (K_0). Die lokale interstellêre spektra (LIS) van KS wat met die modelle bereken is, is vergelyk met die eksperimentele KS-data deur middel van 'n χ^2 toets. Vir elke stel van eksperimentele waarnemings, is die LIS aangepas met behulp van die kragveld-benadering en die individuele KS-spesies is in drie groepe volgens die fraksie van sekondêre en primêre kerne in elkeen verdeel. As resultaat is gevind dat die parameterwaardes vir die beste passingsmodelle verskille toon tussen die primêre, die gemengde en die sekondêre KS-komponente. Die sekondêre KS het makliker op die data gepas as die primêre of die gemengde komponent wat aandui dat die 2D GALPROP-model, soos toegepas, inderdaad meer geskik is vir sekondêre KS as vir primêre KS. Die resultate, tesame met die wyse waarop die 2D-model KS-bronne hanteer, impliseer dat daar waarskynlik plaaslike KS-puntbronne voorkom wat tot dusver nog nie in ag geneem is nie.

Nomenclature

Listed are the acronyms used in the text. For the purpose of clarity, the acronym is written out in full when it appears for the first time in the text.

AU	astronomical unit
CR	cosmic ray
HCS	heliospheric current sheet
HMF	heliospheric magnetic field
ISM	interstellar medium
ISRF	interstellar radiation field
LIS	local interstellar spectra
MPI	message processing interface
SNR	supernova remnant
VLIS	very local interstellar spectra
1D	one-dimensional
2D	two-dimensional
3D	three-dimensional

Contents

Chapter 1

Introduction

Cosmic rays (CRs) are fully charged energetic particles that originate in discrete sources in the Galaxy and then propagate from these sources through the galactic interstellar medium (ISM). The chemical composition of the CRs measured at Earth allows insights into the properties of the galactic ISM. All stable and long-lived isotopes in the periodic table can be observed in a wide range of energies by means of satellite, balloon and ground-based detection experiments. Those elements which are produced in large abundances in the sources are called primary CR species, while those which are principally produced by spallation in the interstellar gas are called secondary CR species (Longair, 2004a).

The main sources of CRs are believed to be supernovae and supernova remnants (SNRs), pulsars, compact objects in close binary systems, and stellar astrospheres. Supernovae meet the energetic requirements and provide the assumed process of galactic CR acceleration, Fermi I acceleration at supernova blast shocks (Büsching, 2004). Supernovae are thus the most plausible source of galactic CR nuclei. Observational evidence, such as the discovery of the acceleration of highly energetic charged particles at the shell of supernova remnant, RXJ1713.7-3946 (Aharonian et al., 2004), also supports this assumption.

Time-dependent calculations (taking into account all three spatial dimensions and assuming the bulk of the galactic CRs to originate in transient, point-like sources like supernovae and their remnants) have shown that the flux of the CR primary component measured at Earth strongly depends on the local source history (Büsching et al., 2005). This emphasises the need of a 3D, time-dependent treatment of the galactic CR propagation, as only those models are able to properly describe transient, point-like sources like SNRs.

The widely used steady-state, rotational symmetric models (2D models) of CR propagation assume sources distributed evenly over the whole Galaxy in the angular direction, which do not necessarily result in the same local CR flux as produced by real local point-sources. This suggests that the 2D models may not be adequate to describe the CR primary component originating

from point-like CR sources. The 3D time-dependent calculations also show that the secondary CR component is not affected by local point-like sources. When working with 2D models, concentrating on secondary, tertiary and higher CR nuclei may thus yield a better description of galactic CR propagation, as the flux of these nuclei does not depend on the local source history (Büsching et al., 2005).

In this work, the fact that 2D models do not describe CR primaries and secondaries equally well, is used to look for evidence of nearby CR point sources. Doing a parameter study, one may thus expect different best fit values for the relevant parameters determining particle propagation, looking at the primary and secondary CR components separately, as it is unlikely that the source history mimicked by the 2D models coincides with the real local source history.

For this study the 2D version of the GALPROP code, a self consistent CR propagation numerical model mainly used to estimate local interstellar spectra and to produce skymaps for diffuse γ-rays and synchrotron emission, was adapted to a compute-cluster environment using the Message Processing Interface (MPI) framework. It was then used to perform parameter studies that compare CR spectra with mainly primary and secondary CR data separately. The following objectives outline this study:

(1) Study the physics contained within the GALPROP code and the numerical scheme used.

(2) Test and validate the GALPROP code, by reproducing existing results of Ptuskin et al. (2006).

(3) Investigate the possibility of accounting for heliospheric modulation with a 2D modulation code.

(4) Use the GALPROP code in a parameter study to separately fit calculated local interstellar spectra (LIS) to Primary and Secondary CR data.

(5) Compare the results for primaries and secondaries to look for signatures of a local or nearby point source of CRs in their chemical composition.

This work is structured as follows:
In **Chapter 2** an overview of the basic features of the Galaxy, the heliosphere and of CRs propagating in these structures is given. The focus of this study is on the modelling of the physical processes in the Galaxy that affect the propagation of CRs. The equations describing CR transport in the Galaxy and the heliosphere are discussed, as well as CR origins and detection. Additionally, the importance and challenges of studying LIS are highlighted.

The Galactic Propagation code (GALPROP), as described in **Chapter 3**, is a numerical code for calculating the propagation of relativistic charged particles and the diffuse emissions produced during their propagation (Ptuskin et al., 2006; Strong et al., 2007). The relevant features

and capabilities of the code are presented. Some features not considered in this study (such as diffuse γ-ray skymaps and dark matter calculations) are mentioned as well, as these may be necessary for future studies. The numerical scheme used in the code is also briefly presented.

Before the GALPROP code can be used to perform a parameter study, the code needs to be implemented and tested by comparing its output with known results. In **Chapter 4** results for LIS as calculated with the GALPROP code by Ptuskin et al. (2006) are reproduced. The effect of different grid spacings is tested, the prospect of using the 3D case in the GALPROP code is examined, as well as discussing the shortcomings in the current 3D implementation.

Modulation studies in the heliosphere are conducted with various approximations of the CR transport equation, first derived by Parker (1965). **Chapter 5** investigates two of these approximations, the widely used force field approximation and a 2D drift model. The full description of the modulation problem requires the determination of the CR intensity as a function of three spatial coordinates, time and energy. Because of the complexity, the full numerical solution of the transport equation is rarely used. Various levels of approximations can be made to simplify the numerical solution, not all of which are equally suited for heliospheric CR transport problems, thus the simplified numerical models cannot be applied to each situation.

The main study is conducted in **Chapter 6**, the purpose of which is to compare the results obtained from the 2D GALPROP code for primary and secondary CR species, respectively. Fitting the local LIS to experimental data seperately for primaries and secondaries, should show whether the 2D GALPROP code can consistently describe both CR components. To accomplish this goal a parameter study was done by varying three of the parameters in the 2D plain diffusion model used by Ptuskin et al. (2006). The details of these models, parameter space and data fitting are discussed. The best fit LIS found in the parameter study are compared to the LIS obtained by Ptuskin et al. (2006). The parameters giving the best fit LIS are also compared to parameter values found by Maurin et al. (2002) and Putze et al. (2009, 2010).

A summary of the main results and conclusions are given in **Chapter 7**.

Chapter 2

Cosmic Rays in the Galaxy

2.1 Introduction

Cosmic rays are a valuable tool for astrophysical studies, as the particles can directly be sampled at or near Earth, and not just observed indirectly via electromagnetic radiation. Understanding the processes by which these CRs are produced, accelerated and propagated through the Galaxy, will give great insight into the Galaxy, such as its matter content and magneto-hydrodynamic properties (Maurin et al., 2002).

Studying the CRs measured at Earth requires insight into the properties and physical processes in the heliosphere, the Galaxy and the sources of CRs. The focus of this study is on the modelling of physical processes in the Galaxy that affect the propagation of CRs. This requires not only a background knowledge on the properties of CRs and the Galaxy, but also on the heliosphere, as CRs have to traverse the heliosphere before being detected at Earth.

This chapter gives an overview of the basic features of the Galaxy, the heliosphere and of CRs. The properties and processes of the Galaxy and the heliosphere, pertaining to the propagation of CRs, are presented here. The equations describing the propagation for CR transport through the Galaxy and the heliosphere are discussed, as well as CR origins and detection methods.

2.2 Cosmic rays

It was found in the early 1900s that electroscopes discharged even if kept in the dark, well away from sources of natural radioactivity. The origin of this behaviour was unknown at that time and various experiments were conducted to discover the cause behind the ionising radiation. In 1912 and 1913 Victor Hess performed manned balloon flights of up to an altitude of 5 km to measure the ionisation of the atmosphere with increasing altitude. Hess discovered that the average ionisation increased unexpectedly with altitude for heights above about 1.5 km and therefore the

source of the ionising radiation had to be extraterrestrial, rather than within the Earth. This source was later called 'cosmic radiation' and 'cosmic rays' by Millikan in 1925 (Longair, 2004a).

Cosmic rays are energetic charged particles with energies larger than about 1 MeV to about 10^{21} eV, that arrive at Earth from space. Unlike photons, CRs are deflected and isotropised by the magnetic fields in space and arrive in the solar system from all directions. The arrival directions of the CRs thus do not point back to the actual positions of their acceleration (Gabici, 2008).

2.2.1 Cosmic ray spectra

The differential energy spectra of various CR species can be represented by power-law distributions for the energy range $E \geq 20\,\mathrm{GeV/nuc}$. In this range modulation by the solar wind (see Section 2.4) in the heliosphere can be neglected. The power-law is given by:

$$N(E)dE = KE^{-x_{sp}}dE \tag{2.1}$$

where the energy E is expressed in terms of the kinetic energy per nucleon and $x_{sp} \approx 2.5$ to 2.7. This relation is found to be applicable to protons, nuclei and electrons ($x_{sp} \approx 3.0$) with energies between 1 GeV/nuc and 10^5 GeV/nuc (Longair, 2004a). Cosmic ray spectra are mostly steep, this means most of the particles and energy carried by CRs are concentrated in the lower energy end of the spectrum, in particles with kinetic energy of less than 1 GeV/nuc (Stanev, 2004).

As seen in Figure 2.1, at approximately $E > 4{\times}10^6\,\mathrm{GeV/nuc}$ the CR spectrum exhibits a break and becomes steeper with $x_{sp} \approx 3.1$. This break is known as the knee of the spectrum. The reason for the occurrence of the knee is believed to be a less efficient mechanism of CR acceleration in supernova shocks. At these energies the gyroradius of the particle exceeds the size of the shock. Additional breaks are observed at about $10^8\,\mathrm{GeV}$, called the second knee, and at about $5{\times}10^9\,\mathrm{GeV}$, called the ankle. The ankle has been reported convincingly by a number of experiments, but there is still no consensus about the existence of a second knee. This is because the structure is unpronounced, making it difficult to detect and because of the sparse experimental data. The ankle is traditionally explained in terms of the transition from galactic CRs to extragalactic CRs. It is expected that the galactic magnetic field loses its efficiency of keeping particles contained at about this energy, as the gyroradius of a particle at these energies becomes comparable to the thickness of the galactic disk. Extragalactic CRs, that penetrate into the Galaxy, then start to dominate the flux at higher energies (Kampert, 2007).

2.2.2 Cosmic ray detection and data

Information on the flux of CRs comes from satellite, balloon and ground-based detection experiments. Experiments carried out using cloud chambers and detector arrays showed that

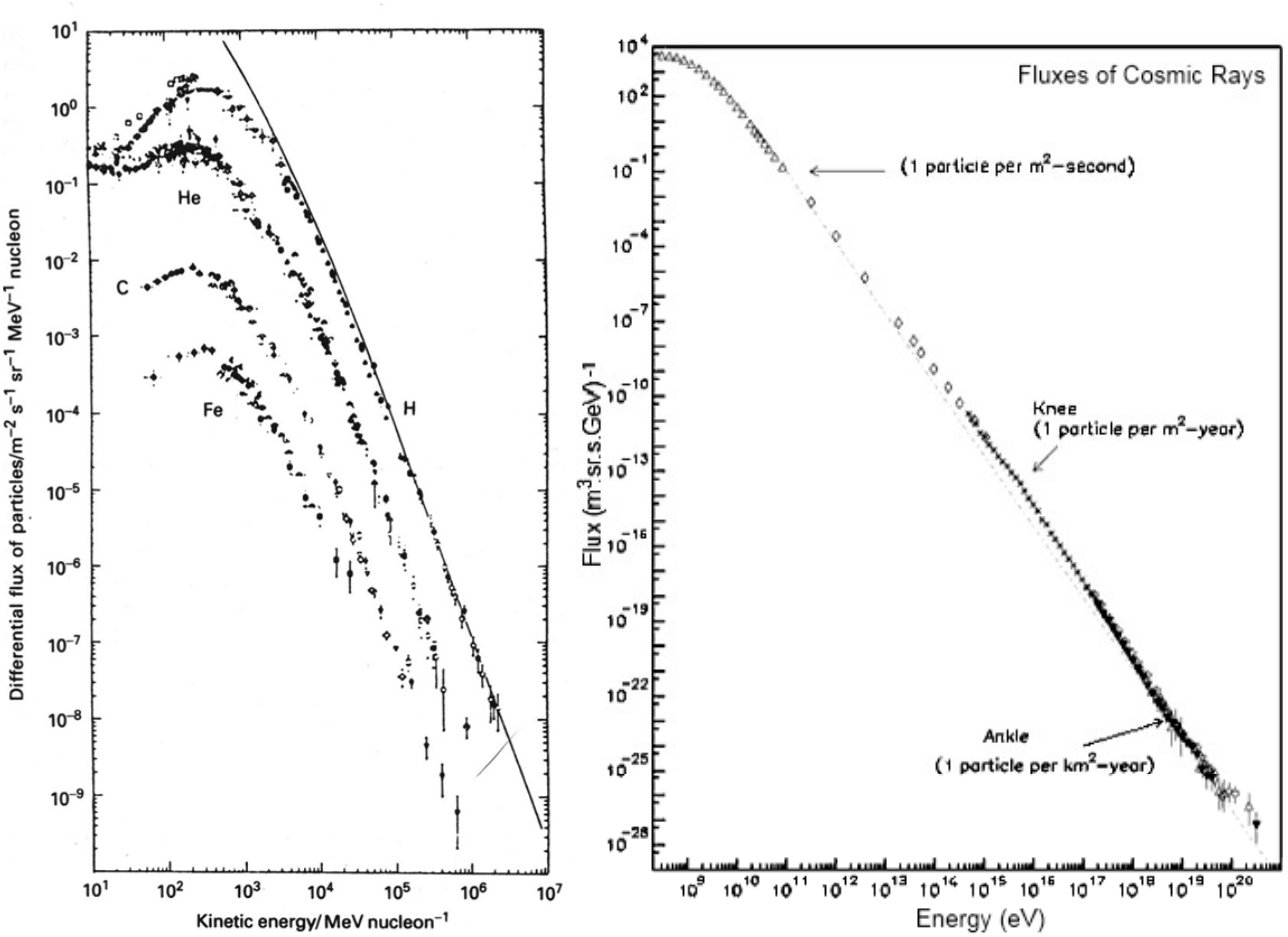

(a) Spectra of CRs measured at Earth.

(b) Compilation of various CR data.

Figure 2.1: Differential energy spectra of CRs as measured at Earth. Panel (a) shows measurements made above the Earth's atmosphere. The spectra for H, He, C and Fe are shown here. The solid line indicates the estimated spectra outside the heliosphere (Longair, 2004a). Panel (b) shows the compilation of various measurements of the differential energy spectrum of CRs. The dotted line shows a power-law with $x_{sp} = 3.0$. Two features of the spectrum, the knee and the ankle, are indicated (Cronin et al., 1997).

showers of CR particles are more often observed than individual particles. Most CR particles observed at the surface of the Earth are secondary, tertiary or higher products of very high energy CRs entering the atmosphere and undergoing inelastic collisions with atmospheric ions, atoms and molecules. At energies greater than about 10^{14} GeV, CRs are detected by large air-shower arrays on the surface of the Earth. The arrival rate of the most energetic particles is very low, but nevertheless particles of up to about 10^{20} eV have been detected. Ground-based air-shower observations have the advantage of having long exposure times and large effective detection areas. The disadvantage is that the shower measurements can only be analysed with numerical models and thus the quality of the measurements depends on the accuracy of the models. Air-shower observations also cannot distinguish between different CR isotopes. The disturbing effects of the Earth's atmosphere disappear when CR experiments are flown outside of it. Due to the logistics involved with such satellite experiments, the detectors are limited in size and weight. The observation time is also limited in most cases, thus these experiments

cannot measure weak CR intensities. For particles of up to about 10^4 GeV/nuc, the best data are derived from space experiments, whereas at higher energies $\geq 10^4$ GeV/nuc information on CRs is provided by ground-based detectors and in the intermediate energy range balloon born experiments also provide valuable data (Longair, 2004a; Schlickeiser, 2002).

The experimental data for CRs are diverse and values can vary between different experiments, due to the systematics applied. Some of the differences are significantly bigger than the combined statistical and systematic errors derived by the experimental groups, indicating that some systematic errors are not fully understood. Cosmic ray experiments are designed with a specific objective, measuring CRs of a certain type at a certain energy range. Thus not all detectors give the same quality of data when detecting a specific CR element. In the region below 20 GeV/nuc, the data may be affected by solar modulation for which it is not fully corrected, because few measurements are made in exactly the same epoch of the solar cycle. Above 20 GeV/nuc solar modulation is assumed to be insignificant (Stanev, 2004).

2.2.3 Cosmic ray origins and acceleration

CRs are accelerated far outside the heliosphere and propagate through the Galaxy before penetrating the heliosphere. The lower energy CRs are then modulated inside the heliosphere by the solar wind and magnetic field perturbations before reaching the Earth. Cosmic ray sources in the Galaxy have to provide the steady power of 10^{33} W needed to sustain the observed density of CRs (Ginzburg and Syrovatskii, 1964) and account for the nearly uniform and isotropic distribution of CR nucleons and electrons with energies below 10^6 GeV over the Galaxy. Also to be accounted for is the power-law energy spectra that is observed for all CR species and over large energy ranges (see e.g., Schlickeiser, 2002).

Supernovae are the most widely accepted candidates for CR acceleration. Supernova remnants (SNRs) are attractive candidates for CR acceleration because they release enough energy to supply the necessary CR power. Also, Fermi I acceleration at supernova blast wave shocks, that form during the expansion of SNRs, is believed to be the acceleration mechanism for CRs as it can produce the observed power-law spectra. SNRs are also large and last long enough to carry the acceleration process to high energies and have stronger magnetic fields than the average interstellar medium (ISM) (e.g., Stanev, 2004; Gabici, 2008).

2.2.4 Cosmic ray chemistry and abundances

At Earth, about 98% of the particles of the total CR flux detected are protons and nuclei, while about 2% are electrons. Of the protons and nuclei, about 87% are protons, 12% are helium nuclei and the remaining 1% consists of heavier nuclei. This composition stays approximately the same over the range of energies from a few hundred MeV to over 10^5 GeV (Longair, 2004a).

The elemental abundances of CR nuclei are compared to those of the solar system abundances in Figure 2.2. When normalising the abundances with respect to Silicon, the CR abundances are seen to be similar to the solar system abundances, with exceptions. The light elements Lithium, Beryllium and Boron, and the sub-Iron group, Scandium, Titanium, Vanadium, Chromium and Manganese are over-abundant by up to several orders of magnitude, while Hydrogen and Helium are seen to be under-abundant in CRs. (Gombosi, 1998; Schlickeiser, 2002; Longair, 2004a).

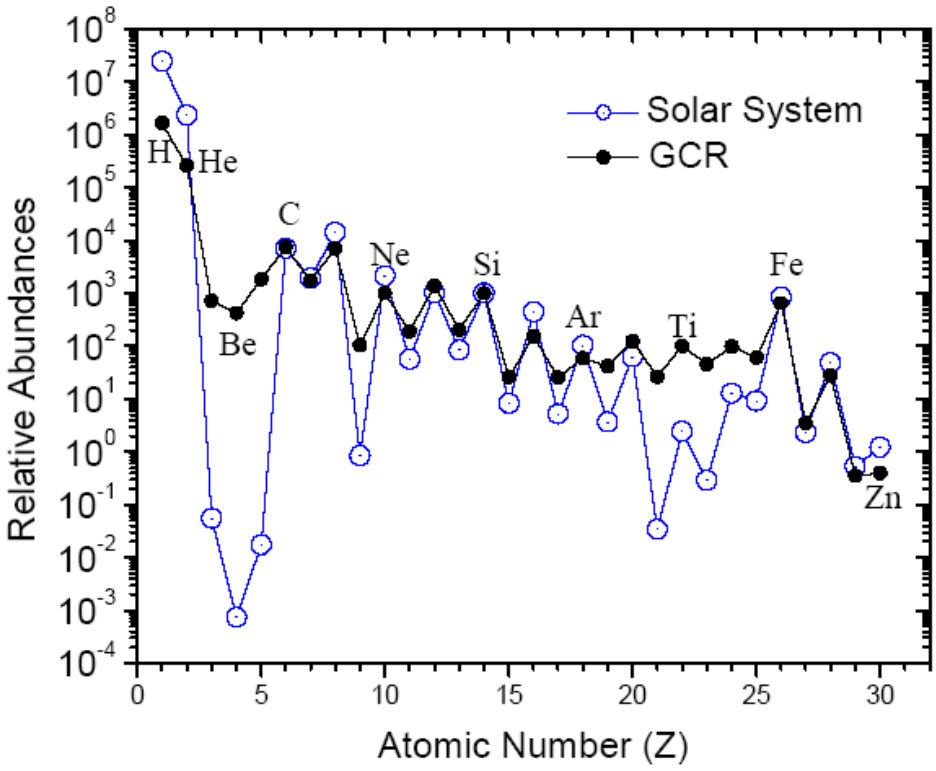

Figure 2.2: Relative abundances of both CR and solar system material at 150 to 550 MeV/nuc normalized to Si = 10^3. The abundances of the CR nuclei are shown with the closed circles and for elements such as Li, Be, B, Sc, Ti, V, CR and Mn are seen to be larger than for the solar system abundances (Schlickeiser, 2002).

This significant change in chemical composition, as seen in Figure 2.2, is attributed to spallation processes in the ISM. Spallation, the process in which a heavier nucleus collides with matter and the resultant expulsion of a large number of nucleons (protons and/or neutrons), result in CRs being produced as fragmentation products of heavier elements. Cosmic ray elements accelerated in sources of high energy particles such as supernovae remnants in the Galaxy, are referred to as primary CRs. These primaries have a large abundance in both CR and solar system abundances. Elements resulting from the fragmentation of the primary CRs during the propagation through the ISM are referred to as Secondary CRs and have a high relative abundance compared to their solar abundances (Schlickeiser, 2002). Protons, Carbon and Iron are examples of primary species while ^{2}H, ^{3}He, Beryllium, Boron, Potassium, Titanium and Vanadium are secondary CRs (Longair, 2004a).

2.3 The Galaxy

Our solar system is located in the Milky Way galaxy, a barred spiral galaxy. The luminous matter of the Galaxy is organised in spiral arms that join in the inner Galaxy to form the galactic bulge. Viewed from the side the matter is distributed in a disk with height h of about 100-150 pc (a total thickness of $2h$) in the vicinity of the solar system, which is located about 8.5 kpc from the galactic centre. The radius of the galactic disk is approximately 20 kpc, as illustrated in Figure 2.3 (Stanev, 2004).

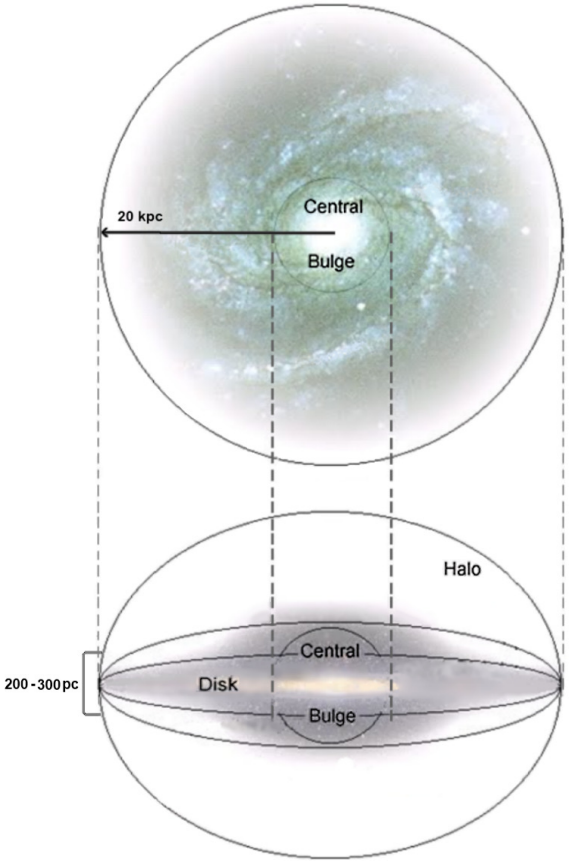

Figure 2.3: Diagram of the Milky Way galaxy showing the disk, halo and central bulge. The Galaxy is a barred spiral galaxy, with the luminous matter organised in spiral arms that join in the inner Galaxy to form the galactic bulge. The radius of the galactic disk is approximately 20 kpc. Viewed from the side the matter is distributed in a disk with total height of about 200-300 pc. (Adapted from `http://web.njit.edu/~gary/321/Galaxy.jpg`.)

2.3.1 Galactic structure and features

The galactic structure directly affects the propagation of CRs. The most important galactic features are the gas content, which influences the production of secondary CRs, as well as the interstellar radiation field (ISRF) and magnetic field that influences the energy loss processes. Also important are the turbulence properties of the magnetic field as these determine the particle diffusion (Strong et al., 2007).

Once accelerated at supernova shocks, CRs have to propagate through the ISM before reaching the solar system. The ISM contains matter, magnetic fields and radiation fields, all of which interact with CRs. Cosmic rays scatter off irregularities in the magnetic field and slowly diffuse away from their sources (Berezinskii et al., 1990). Observations show that CRs at Earth are isotropic to a very large degree, an anisotropy of about 10^{-3} for energies $E = 10^{12} - 10^{14}\,\mathrm{eV}$ (Amenomori et al., 2005; Abbasi et al., 2010). Cosmic ray nuclei interact mostly with the interstellar matter and produce secondary particles. CR electrons interact with the magnetic and radiation fields, as well as with the interstellar matter. In magnetic fields they generate synchrotron radiation and in radiation fields they produce γ-rays via the inverse Compton effect (Stanev, 2004).

Interstellar matter

The interstellar matter is made up of dust and gas, with the gas composed mainly of Hydrogen (70%), Helium (28%) and a 2% contribution from heavier elements. Most of the gas in the Galaxy is confined to the galactic plane and moves in circular orbits about the galactic centre. Hydrogen is present in different states in the interstellar gas: HI, HII and molecular hydrogen. The neutral atomic HI hydrogen is either clumped in HI clouds or distributed diffusely as intercloud medium. Molecular hydrogen can only exist in dark cool gas clouds where it is protected against the ionising stellar ultraviolet radiation. Roughly 40% of the mass of the interstellar hydrogen appears in this form. A tracer for the spatial distribution of molecular hydrogen is the $\lambda = 2.6\,\mathrm{mm}$ emission line of carbon monoxide (CO), since collisions between the CO and molecular hydrogen in the gas clouds are responsible for the excitation of the CO. The neutral and molecular hydrogen are closely confined to the plane of the Galaxy, with typical half-widths being about 120 pc and 60 pc, respectively. They have very different distributions with distance from the galactic centre. The neutral hydrogen extends from about 3 kpc to beyond 15 kpc from the centre, whereas the molecular component appears to form a thick ring between radii of about 3 and 8 kpc. Regions in the vicinity of young, bright O and B stars are called HII regions due to the interstellar gas being ionised by intense ultraviolet radiation from these stars. Their radial distribution is similar to that of molecular hydrogen, but their mass contribution is negligible. HII regions are a good tracer of the spiral structure of the Galaxy (Schlickeiser, 2002; Longair, 2004b).

Interstellar dust is an important constituent of the ISM since it absorbs ultraviolet and optical photons, then re-emits the radiation at infrared wavelengths and also emits electrons to heat the ISM. The dust is generally well mixed with the total interstellar gas, and its density correlates well with the total gas density. The dust is believed to be formed in the atmospheres of cool stars and ejected into the ISM by radiation pressure (Schlickeiser, 2002). The ISRF comes from stars of all types and is processed by absorption and re-emission by the interstellar dust. It extends from the far-infrared to the ultraviolet (Strong et al., 2007).

Magnetic and electric fields

The distribution of the rotation measures of pulsars, extragalactic radio sources and optical polarisations vectors convincingly proves the existence of some large-scale order in the galactic magnetic field. In the vicinity of the Sun, the uniform component of the field runs roughly along the local spiral arm (Han and Wielebinski, 2002). Studies so far indicate that the magnetic fields in the Galaxy are directed along the spiral arms, thus azimuthal and any deviations of the pitch-angle of the field from the spiral arms are small. The magnetic field also includes a wide range of random components and the structure of the magnetic field is not the same in different regions of the ISM (Berezinskii et al., 1990). Polarisation measurements have shown that the field lines in the galactic disk run exactly perpendicular to the galactic plane. Estimates of the strength of the magnetic field lie in the range $10^{-9} - 10^{-10}$ T. Zeeman spectral line splitting experiments, sampling photons from structures in the Galaxy, indicate that stronger magnetic fields are present in gas clouds (Schlickeiser, 2002; Longair, 2004b).

In contrast, large-scale steady electric fields cannot exist in the Galaxy. The high electrical conductivity of non-stellar cosmic media would immediately short-circuit any steady electric field. Transient electric fields may well be generated during non-stationary cosmic induction processes, such as stellar flares or pulsars (Schlickeiser, 2002).

2.3.2 Cosmic ray propagation in the Galaxy

There are general laws that can be used to study the propagation of charged particles in the Galaxy, even though interstellar conditions, such as the strength of the magnetic field and the density of matter, are dependent on the position in the Galaxy and can show strong fluctuations (Stanev, 2004).

Source spectra

Supernovae explosions eject stellar matter at high velocities, giving rise to the formation of SNRs. The expanding SNR forms shock waves when interacting with the ISM. Cosmic rays traveling repeatedly across the shock waves are accelerated to high energies through the process of Fermi I acceleration. Cosmic ray primaries are injected into the ISM from an individual SNR with a power-law spectrum:

$$q(P) \propto P^{-\alpha} \tag{2.2}$$

above a minimum rigidity[1] and below a maximum rigidity P_{max}, with $P_{max} = 10^{15}$ V generally used. The sum of the total energy in each spectra has to add up to 10^{42} J, the total amount of energy from a supernovae transfered to energetic particles (Ginzburg and Syrovatskii, 1964). In

[1]Rigidity is defined as the momentum per charge for a given species of particles. It is given by $P = pc/q$ where p is the particle's momentum, q the particle's charge and c the speed of light in vacuum

spiral galaxies like ours it is estimated that supernova explosions occur with a frequency of one event every 50 years. Supernovae are stochastic events and each SNR source of CRs is active up to 10^4 to 10^5 years (Schlickeiser, 2002).

Diffusion

The concept of diffusion explains why energetic charged particles have highly isotropic distributions and why they are well retained in the Galaxy. On a microscopic level, the diffusion of CRs results from particle scattering on random plasma waves and discontinuities. Waves arise in magnetised plasmas in response to instabilities. The resulting spatial diffusion is strongly anisotropic locally and goes predominantly along the magnetic field lines. However, strong fluctuations of the magnetic field on large scales ($L \approx 100\,\mathrm{pc}$) where the strength of the random field is several times larger than the average field strength, lead to the isotropisation of global CR diffusion in the Galaxy (Strong et al., 2007).

Convection

Galactic winds perpendicular to and away from the galactic disk are common in galaxies and can be CR driven. Convection not only transports CRs, but can also produce adiabatic energy losses as the wind accelerates expands away from the disk (Strong et al., 2007).

Reacceleration

In addition to spatial diffusion, the scattering of CR particles at randomly moving plasma waves leads to stochastic acceleration, which is described in transport equations as diffusion in momentum space with diffusion coefficient K_{pp}. Reacceleration in the entire galactic volume cannot serve as the main mechanism of acceleration of CRs, at least not in the energy range 1-100 GeV/nuc. In this case the particles of higher energy would spend a longer time in the system, which would result in an increase of the relative abundance of secondary nuclei as energy increase, contrary to observation. This argument does not hold at low energies, where reacceleration may be strong, and it may explain the existence of peaks in CR spectra and the Boron to Carbon (B/C) ratio (Strong et al., 2007).

Interactions and energy losses

High energy particles are subject to a number of energy loss processes as they propagate from their sources through the ISM. Different interactions and mechanisms are important for CR electrons and CR nuclei. For CR electrons these loss processes involve interactions with matter, magnetic fields and radiation: ionisation losses, bremsstrahlung, adiabatic losses, synchrotron radiation and inverse Compton scattering (Longair, 2004b). These energy loss processes are

explained as follows: bremsstrahlung (or braking-radiation) is the radiation associated with the acceleration of electrons in the electrostatic fields of ions and the nuclei of atoms. Adiabatic energy loss, also known as adiabatic cooling, is the loss of energy of particles due to the expansion of the volume within which the particles are contained. Synchrotron radiation is the loss process where particles radiate photons due to spiralling around magnetic field lines. Coulomb scattering is the interaction of particles due to Coulomb forces and influences only low energy particles. High energy electrons can also scatter low energy photons to higher energies, so that in the Compton interaction the electrons lose energy to the photons. This process is called inverse Compton scattering (Longair, 2004a).

Due to the higher mass of CR nuclei, the cross-sections for electromagnetic interactions of CR nuclei are much smaller than those for CR electrons of the same Lorentz factor. The electromagnetic interactions thus contribute negligibly to the loss processes for CR nuclei. The remaining important processes are ionisation losses, the inelastic reactions of CR nuclei with atoms and molecules of interstellar matter, including Coulomb interactions, and losses due to adiabatic cooling (Schlickeiser, 2002). Interactions of CR nuclei with photons in the Galaxy, the ISRF, are only relevant for nuclei with very high energies of about 10^{18} eV and above. Three types of photon interactions are of importance for relativistic nuclei: pair production, photo-production of hadrons and photo-disintegration of the nucleus (Schlickeiser, 2002).

Fragmentation and decay

Lighter nuclei can be produced as fragmentation products of the interactions of heavier high energy nuclei with interstellar matter and at high energies through photo-disintegration (Longair, 2004b). The fragmentation losses are catastrophic losses described by a loss time, thus they do not conserve the total number of particles of the considered nuclei. The fragmentation loss time τ_f can be obtained by:

$$\tau_f = [1.3(n_{HI} + 2n_{H_2})c\beta\sigma_{tot}]^{-1}\,\mathrm{s} \tag{2.3}$$

where n_{HI} and n_{H_2} are the densities of the respective forms of Hydrogen and σ_{tot} the energy dependent total cross-sections for inelastic collisions. The factor of 1.3 comes from the inclusion of collisions with Helium in the ISM.

To estimate the yield of fragmentation products from inelastic reactions and calculating the transformation of chemical and isotropic composition, a large number of individual fragmentation cross-sections are needed. Direct measurements, numerical model calculations and semi-empirical formulae are used to obtain these cross-sections. Compilations of partial cross-sections for the collisions of various nuclei with Hydrogen are tabulated by e.g. Mashnik et al. (1998) and Silberberg et al. (1998).

In the case of the decay of unstable particles, such as Be^{10} and Al^{26}, the timescale is determined by:

$$\tau_r = \gamma T^0 \tag{2.4}$$

where T^0 is the radioactive half-life at rest and γ the Lorentz factor (Schlickeiser, 2002). The two catastrophic losses are combined as:

$$\frac{1}{\tau_c} = \frac{1}{\tau_f} + \frac{1}{\tau_r}. \tag{2.5}$$

A decay process also of importance is K-capture. An electron from the K electron shell is captured by a proton in the nucleus, forming a neutron and a neutrino. Thus decreasing the atomic number. Because these atoms have only one K-shell electron, the K-capture decay half-life must be increased by a factor of two, compared with the measured half-life value. K-capture works only for β^+ unstable isotopes. When the decay energy is to low to produce an electron-positron pair, K-capture is the only decay channel. Should these particles be fully ionised, they remain stable.

2.3.3 Modelling galactic propagation

To accurately model the propagation of CRs through the Galaxy, a model needs to take into account the processes mentioned in Sections 2.3.1 and 2.3.2. Three such propagation models are discussed: the leaky box model, the weighted slab model and the diffusion model. These models vary in the amount of physical processes included and how thoroughly the processes are implemented.

The leaky box model

The leaky box model is the simplest model to describe the propagation of CRs. It assumes a volume, a box, in which CRs are injected by uniformly distributed sources and propagate freely, with a certain chance to escape the box. This chance is represented by the timescale T_{escape}, the average time the CR particles spend in the Galaxy. The escape time may be a function of particle energy, charge and mass number, but does not depend on the spatial coordinates as the leaky box model does not take into account spatial dependences at all. Loss process due to spallation and energy losses can also be included, as well as uniformly distributed gas and radiation fields (Büsching, 2004; Strong et al., 2007).

In the leaky box model, the density $N_j(t, p)$ of one CR species depending on the time t and particle momentum p, is given by the relation:

$$\frac{\partial N_j}{\partial t} - Q_j = -\frac{N_j}{T_{escape}} - \frac{N_j}{T_{spallation}} - \frac{\partial (b_{avg} N_j)}{\partial p} \tag{2.6}$$

for each particle of type j produced, where $T_{spallation}$ is the average time before a particle is lost due to spallation, Q_j is the source strength and b_{avg} the rate of energy loss. All three quantities are averaged over the volume of the Galaxy and may depend on the particle momentum p. The first term on the right hand side thus gives the loss of particles escaping from the box due to diffusion or convection. The second term gives the catastrophic particle loss due to spallation, and the last term gives the momentum changes for the particles (Büsching, 2004).

The source term Q_j can be written as:

$$Q_j = S_j + \sum_{i>j} N_i v n_{gas} \sigma_{j \to i} \tag{2.7}$$

with the first term accounting for sources of primary CRs, such as SNRs. The second term describes the the source of the secondary CRs due to spallation in the ISM (Ginzburg and Syrovatskii, 1964), with N_i being the density of the particle type i, v the velocity of the particles, n_{gas} the gas density and $\sigma_{j \to i}$ the partial cross-section for particles of type j to become particles of type i. Equations (2.6) and (2.7) give a set of coupled equations that needs to be solved in order to calculate the spectra for the CR species at Earth.

The leaky box model is popular because of its mathematical simplicity and its ability to describe the measured secondary to primary ratios, but fails to account for any spatial inhomogeneities. This model is appropriate for stable secondaries and global estimates, but not suitable for investigations involving the spatial distribution of sources or the distribution of CR in the Galaxy (Büsching, 2004).

The weighted slab model

The weighted-slab technique splits the problem of solving a system of coupled transport equations for all isotopes involved in the process of nuclear fragmentation, into astrophysical and nuclear parts. The nuclear fragmentation problem is solved in terms of a slab model, wherein the CR beam is allowed to traverse a thickness x_{slab} of the interstellar gas and these solutions are integrated over all values of x_{slab}, weighted with a distribution funtion $G(x_{slab})$ derived from an astrophysical propagation model. The weighted-slab method can also be applied to the solution of the leaky-box equations. The weighted-slab method breaks down for low-energy CRs, where one has strong energy dependence of nuclear cross-sections, strong energy losses and energy-dependent diffusion (Strong et al., 2007).

The diffusion model

Cosmic ray propagation can be described as a diffusive process within the Galaxy and the transport equation (Ptuskin et al., 2006) for the differential intensity N_j of CRs can be written as:

$$\frac{\partial N_j}{\partial t} = Q_j + \nabla \cdot (K_{xx} \nabla N_j - \mathbf{V} N_j) + \frac{\partial}{\partial p} \left[p^2 K_{pp} \frac{\partial}{\partial p} \left(\frac{N_j}{p^2} \right) + \frac{p}{3} (\nabla \cdot \mathbf{V}) N_j - \dot{p} N_j \right] - \frac{N_j}{\tau_c} \quad (2.8)$$

The production of CRs of a certain species in the Galaxy is described by the source term $Q_j(\mathbf{r}, p, t)$. The source term is given by Equation (2.7) (includes both primary and secondary CR sources) and defined as the number of particles of type j produced (accelerated) per cm^3 at time t with momentum between p and $p+\delta p$ in a given location $\mathbf{r}$ in the Galaxy. These particles diffuse in the Galaxy and their number changes with time. The time evolution of the density $N_j(\mathbf{r}, p, t)$ of CRs of a given type j and with momentum p at a given location $\mathbf{r}$ in the Galaxy depends on the following six processes in the propagation equation:

- CR diffusion, characterised by the spatial diffusion coefficient K_{xx} in the term $\nabla \cdot (K_{xx} \nabla N_j)$.
- CR momentum diffusion, characterised by the coefficient K_{pp} in the term $\frac{\partial}{\partial p} \left[p^2 K_{pp} \frac{\partial}{\partial p} \left(\frac{N_j}{p^2} \right) \right]$.
- CR convection, characterized by the convection velocity $\mathbf{V}$ in the term $\nabla \cdot (\mathbf{V} N_j)$.
- The rate of change of the particle momentum given by $\dot{p} = dp/dt$.
- Particle losses due to nuclear interactions or decays, where particles of type j have turned into particles of type k and their number has to be subtracted from the density $N_j(\mathbf{r}, p, t)$.
- Particle gains due to interactions, where particles of type i have turned into particles of type j and have to be added to the density $N_j(\mathbf{r}, p, t)$. This term is a weighted sum of all interactions and decays that create particles j. See Equation (2.7).

All these processes affect the CR propagation and determine the CR density as a function of time and energy. The momentum change can be positive or negative. Negative $\dot{p}$ is provided by all forms of energy losses, mostly by synchrotron radiation for electrons or ionisation loss for protons and heavier nuclei. Momentum can also be gained in additional forms of acceleration (such as adiabatic heating) during propagation in the galactic magnetic fields away from the original acceleration site.

Particle losses are determined by the timescale for fragmentation τ_f, with τ_f being dependent on the total spallation cross-section, the gas density and the timescale for radioactive decay τ_r. These catastrophic losses are included in the propagation equation by τ_c with the relation in Equation (2.5) (Moskalenko and Strong, 1998; Stanev, 2004).

The GALPROP model (Ptuskin et al., 2006; Strong et al., 2007) used in this study is based on the diffusion model and is described further in the next chapter.

2.4 Heliospheric modulation

Measurements by various particle detectors have shown that the CR intensity measured at Earth varies with time, space and energy. Cosmic rays entering the region surrounding the Sun are increasingly modulated as they traverse the space dominated by the Sun, called the heliosphere (Heber and Potgieter, 2006).

2.4.1 The Sun and solar activity

The Sun is not a uniform, timeless sphere but a changing and active system, cycling through periodic stages of varying activity. The best known indicator of solar activity is the sunspot number. The number of sunspots on the Sun changes over time in an approximately 11-year cycle. This cycle can be seen in Figure 2.4, along with larger scale variation in the sunspot number such as the so-called Grand Minima and a general increase over time. The variation in sunspot number was the first measurement used to identify the solar cycle (see Hanslmeier, 2002; Stix, 2002).

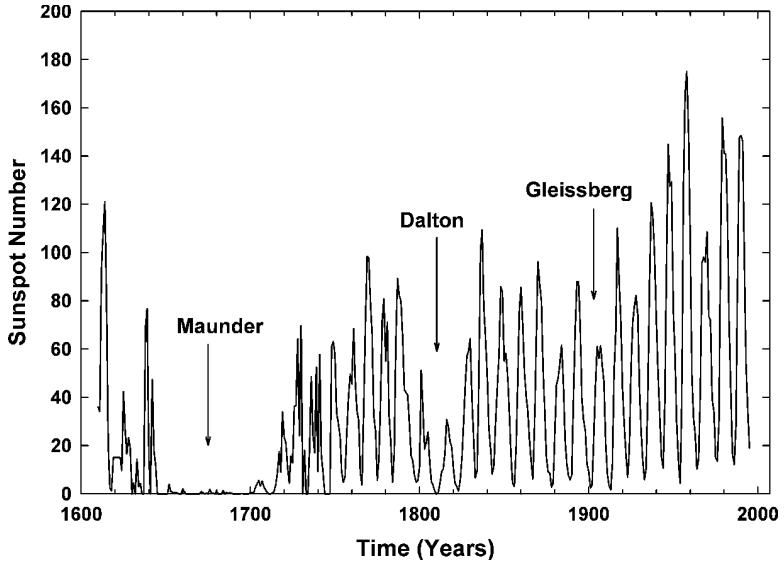

Figure 2.4: The yearly average sunspot number from 1600 until present. Three of the so-called Grand Minima are also indicated. Data taken from the Solar Influences Data Analysis Center (figure adapted from Strauss, 2010).

Solar wind

The solar wind is a supersonic and fully ionised plasma moving approximately radially away from the Sun. The first indications for the existence of a continuously outflowing solar wind came from the study of the orientation of comet tails and as an explanation of geomagnetic storms.

The solar wind originates from the hot solar corona as it expands out into space supersonically. The Sun continuously loses mass, approximately 10^{-14} solar masses per year, by means of this outflow (Hanslmeier, 2002; Balogh et al., 2008).

A consequence of changing solar activity is a changing solar wind speed. During the solar cycle two types of solar wind are observed, a fast solar wind (up to about 750 km.s^{-1}) and a slow solar wind (about 400 km.s^{-1}). Other properties of the solar wind, such as density (seen in Figure 2.5), temperature and composition, also change (Heber and Potgieter, 2006; Balogh et al., 2008).

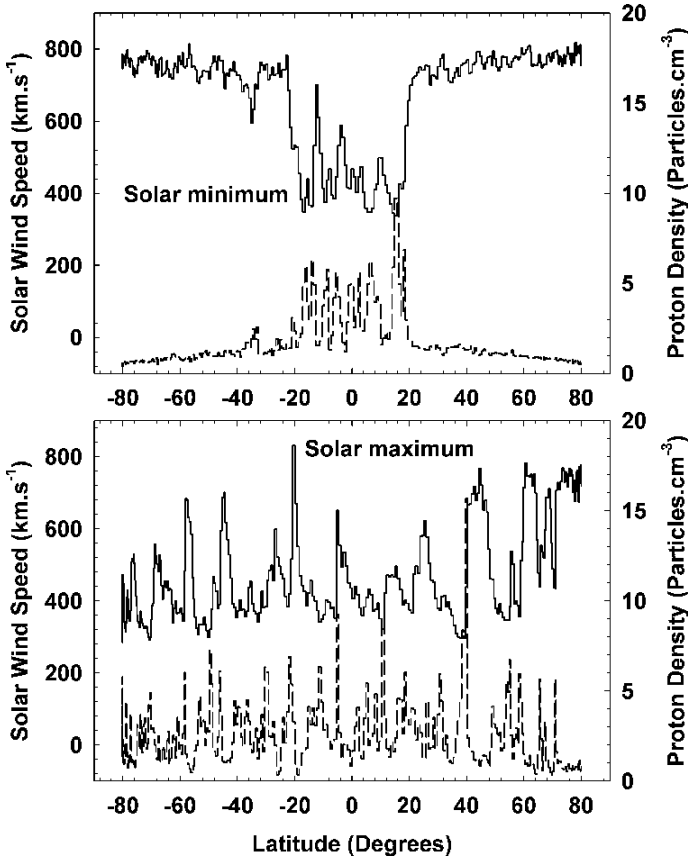

Figure 2.5: The solar wind speed (solid line) and the solar wind proton density (dashed line) as measured by the Ulysses spacecraft during solar minimum conditions (top panel) and solar maximum conditions (bottom panel). The solar equator is located at 0^o latitude (Strauss, 2010).

During solar minimum the solar wind is clearly structured, with a slow solar wind near the equator and a fast solar wind at higher latitudes, as seen in the top panel of Figure 2.5. The fast solar wind comes from the two large polar coronal holes as the solar wind flows faster along open magnetic field lines. The slow solar wind originates from above the equatorial regions where the magnetic field remains closed. Even though the coronal holes around the poles generally have only an angular extent of about 30^o away from the poles, the fast solar wind fills the heliosphere to much lower heliolatitudes. During solar maximum the solar wind speed is on average slow at all latitudes, but it is not as clearly structured as the speed varies greatly with small changes

in latitude. This is illustrated in the bottom panel of Figure 2.5. The coronal holes are small and can be found everywhere on the Sun, not just near the poles. They are generally short-lived, appearing and disappearing within a single solar rotation (Hanslmeier, 2002; Balogh et al., 2008).

The heliospheric magnetic field

Electric currents within the Sun generate a complex magnetic field that extends far out into the heliosphere. In its simplest form the heliospheric magnetic field (HMF) is an extended dipole, with the dipole axis close to the Sun's rotation axis. Portions of the solar field extend up into the corona where the solar wind originates. The perfectly conducting solar wind plasma then carries the magnetic field along with it to completely fill the heliosphere (Ferreira, 2002; Langner, 2004; Krüger, 2005).

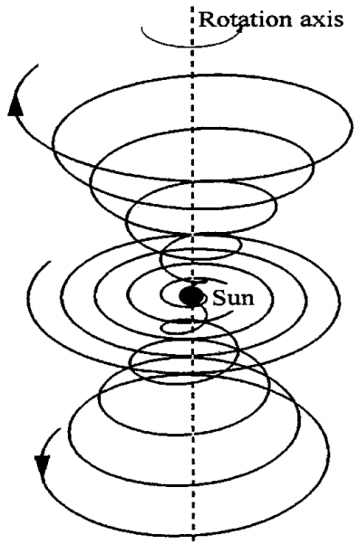

Figure 2.6: The HMF spiral structure according to (Parker, 1958) with the Sun at the origin of the spirals. Spirals rotate around the polar axis at 45^o, 90^o (equatorial plane) and 135^o (Langner, 2004).

The structure and orientation of the solar magnetic field change over the 22-year cycle, with the polarity reversing and returning over this time. The solar magnetic field is generated and modulated by the Sun's differential rotation and convection processes. During solar minimum the magnetic field is well ordered and resembles that of a dipole. As the Sun approaches solar maximum it becomes magnetically less organized. When it reaches solar minimum again, 11 years since the previous minimum, the dipole field is restored and reversed. The dipole field now has opposite polarity. After another solar maximum the Sun is at solar minimum again and the magnetic field has returned to the same polarity as 22 years ago (e.g., Ferreira, 2002; Moldwin, 2008). Although the solar wind moves out almost radially from the Sun, the rotation of the Sun gives the magnetic field the form of an Archimedean spiral that became known as the Parker spiral (Parker, 1958). This structure is illustrated in Figure 2.6.

The heliospheric current sheet

The north and south polarities of the large-scale solar magnetic field extend far outward into the heliosphere. Near the ecliptic plane the hemispheres of opposite polarity are separated by a thin current sheet. This heliospheric current sheet (HCS) has a wavy structure that originates from the fact that the Sun's magnetic axis is tilted relative to the rotational axis. The current sheet changes with the 11-year cycle as the solar magnetic field changes polarity across the current sheet. During high solar activity the tilt angle increases to as much as 70^o, beyond which it becomes indeterminable. With low solar activity the magnetic equator and the heliographic equator are nearly aligned, causing a small tilt angle of 5^o. The wavy structure, seen in Figure 2.7, is carried outward by the solar wind, which can be observed on Earth and is used as a reliable index of solar activity. In Figure 2.8 the tilt angle α_{tilt} as recorded from 1975 to 2009 as a function of time and shows the change with the 11-year cycle.

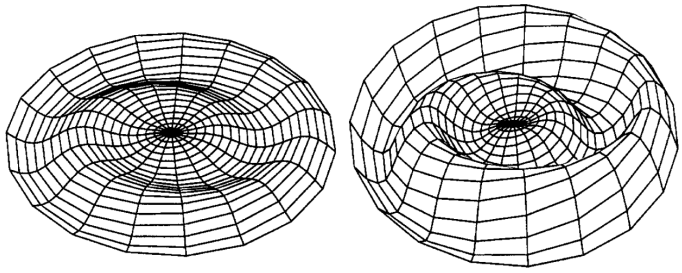

Figure 2.7: The wavy heliospheric current sheet to a radial distance of 10 AU with the Sun is at the centre and a tilt angle of $\alpha = 5^o$, low solar activity (left panel) and $\alpha = 20^o$, moderate solar activity (right panel) (Langner, 2004).

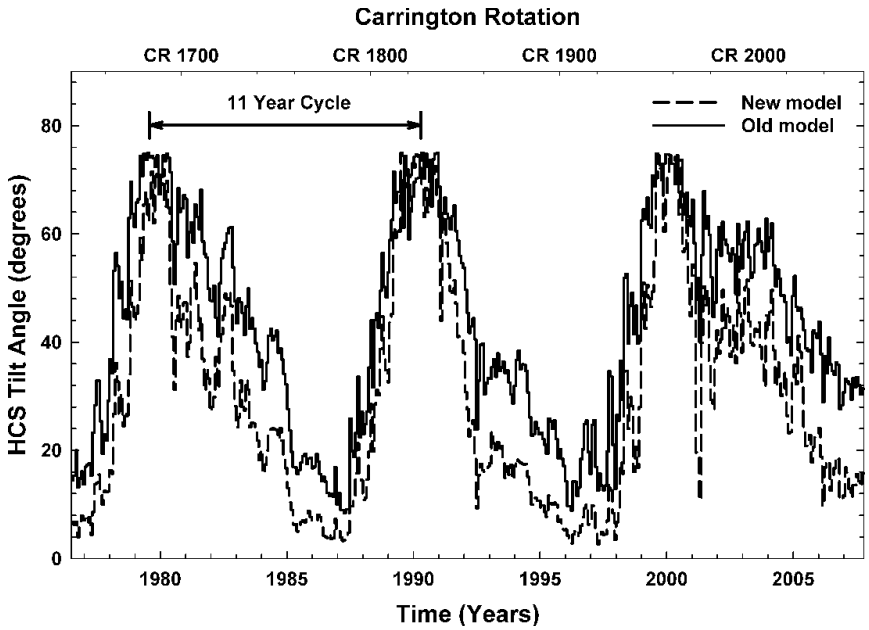

Figure 2.8: The tilt angle α as recorded from 1975 to 2009 as a function of time (bottom axis) and Carrington rotation number (top axis). The tilt angle is shown for the old (solid line) and new models (dashed line). Data from the Wilcox Solar Observatory (Strauss, 2010).

The background HMF, represented by the Parker spiral field, affects the CR transport by contributing drift motions associated with the gradients in field magnitude, the curvature of the field and any abrupt changes in the field direction, such as the HCS. Because the HMF above and below the HCS is oppositely directed, particle drift is caused along the HCS.

During an A $>$ 0 polarity cycle, the HMF is directed outward in the northern hemisphere and inward in the southern hemisphere. The drift direction for positively charged particles is directed from the polar region of the heliosphere, down to the equatorial regions where they get trapped in the HCS and drift along it towards the outer boundary as seen in the right panel of Figure 2.9. The particles are largely insensitive to the conditions in the equatorial region and to changes in the HCS. For the oppositely directed HMF in the A $<$ 0 polarity cycle, the drift direction is towards the inner heliosphere along the HCS and outwards over the polar regions as seen in the left panel of Figure 2.9. This causes the particles to be sensitive to changes in the tilt angle of the HCS. For negatively charged particles the drift is necessarily in the opposite direction (e.g., Potgieter, 1984; Ferreira, 2002).

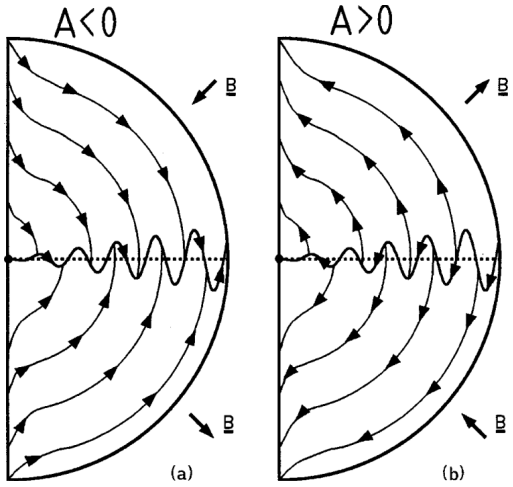

Figure 2.9: The drift directions of electrons due to gradients and curvature in the HMF for Panel (a) the A $<$ 0 HMF polarity epoch when the HMF is directed inward in the northern hemisphere, and Panel (b) the A $>$ 0 HMF polarity epoch when the HMF is directed outward in the northern hemisphere. The proton drift directions are the opposite of the electron drift directions (Langner, 2004).

2.4.2 The heliosphere

The heliosphere exists because of the solar wind that continuously expands into the ISM and excludes this from the vicinity of the Sun and the planets. The size and the boundaries of the heliosphere are thus determined by the interaction between the ISM and the solar wind (Heber and Potgieter, 2006).

The solar system is located in a low density interstellar cloud and moves through it with a velocity of about 26 km.s^{-1}. The heliosphere would be shaped spherically without this relative

speed it has with the ISM. The heliosphere thus has a ellipsoid shape; it is compressed in the upwind direction and elongated in the downwind direction forming an extended heliotail. Therefore the distance to the heliopause is not the same in each direction (Fahr et al., 2000). Its geometry and structure, resulting from axial-symmetric hydromagnetic models, can be seen in Figure 2.10.

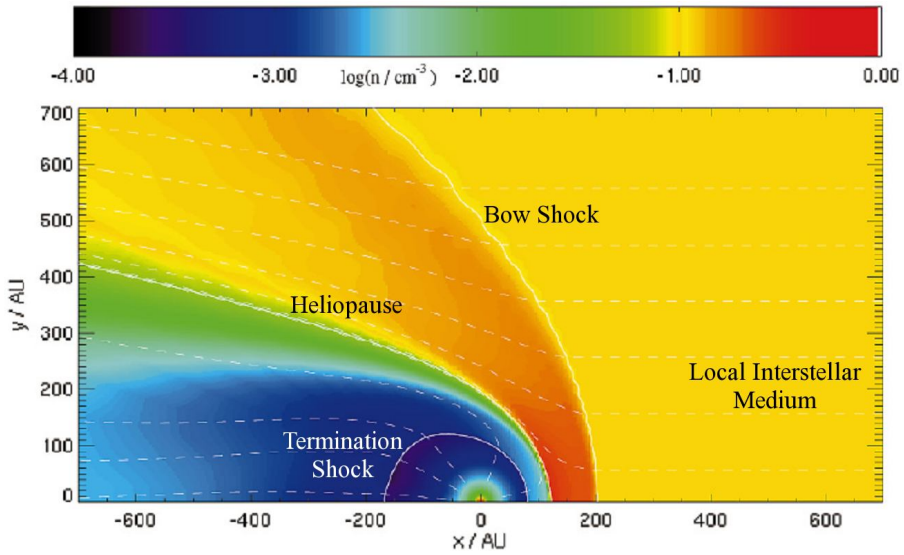

Figure 2.10: A hydrodynamically modelled heliosphere, where the solar wind number density is shown as a meridional cut. The Sun is located at the origin, with the ISM flow directed from the right in the rest frame of the Sun. The solid white lines indicate the different regions of the heliosphere (with the bow shock, heliopause and termination shock labelled), while the dashed line indicate streamlines of the ISM and solar wind respectively. Figure adapted from Strauss (2010) and data from Fahr et al. (2000).

As the solar wind expands into the ISM it must eventually stop at a point where the solar wind pressure becomes comparable to that of the ISM. The heliopause is the contact surface at which the radially decreasing solar wind pressure becomes equal to the back pressure of the ISM. Flow lines of the interstellar plasma do not penetrate the heliosphere, but diverts around the heliopause. This is because space plasmas of different origins do not easily mix due to the entrained magnetic fields in each of the plasmas. Neutral atoms, however, can still easily penetrate into the heliosphere. At the nose of the heliosphere the interstellar gas is nearly stagnating and a density pile-up is expected. The heliopause is generally considered the outer boundary of the heliosphere (Heber and Potgieter, 2006).

The relative motion through the cold ISM is most likely supersonic and therefore an upstream bow shock where the medium decelerates is expected. The presence of a bow shock is also dependent on the parameters of the heliosphere and ISM, such as temperature and density. Between the bow shock and the heliopause there is likely a hydrogen wall, a region in which there is a significant increase in the density of interstellar neutral hydrogen atoms (Fahr et al., 2000; Balogh et al., 2008).

The radially expanding solar wind has to be diverted into the downstream direction or else it would intersect the heliopause. The diversion can only take place in subsonic flow and therefore the supersonic flow must be terminated to form the termination shock. In the downwind direction the shock is likely formed by the expansion of the supersonic solar wind into a low pressure medium. The volume of space between the termination shock and the heliopause is called the inner heliosheath (Fahr et al., 2000; Foukal, 2004).

The best indication of the minimum size of the heliosphere so far is the measurements made by the Voyager 1 and 2 spacecraft when they crossed the termination shock; Voyager 1 in December 2004 and Voyager 2 in October 2007. The distance observed for the termination shock by the spacecraft is about 94 AU for Voyager 1 and about 83 AU for Voyager 2. The location of the termination shock is thus very dynamic. The heliopause is expected to be at least 20 AU beyond the termination shock, depending on the direction. Voyager 1 is presently at 119 AU and closing in on the heliopause. Recent estimates of the heliospheric dimensions by Webber and Intriligator (2011) place it at 1.4 to 1.6 times the distance to the termination shock.

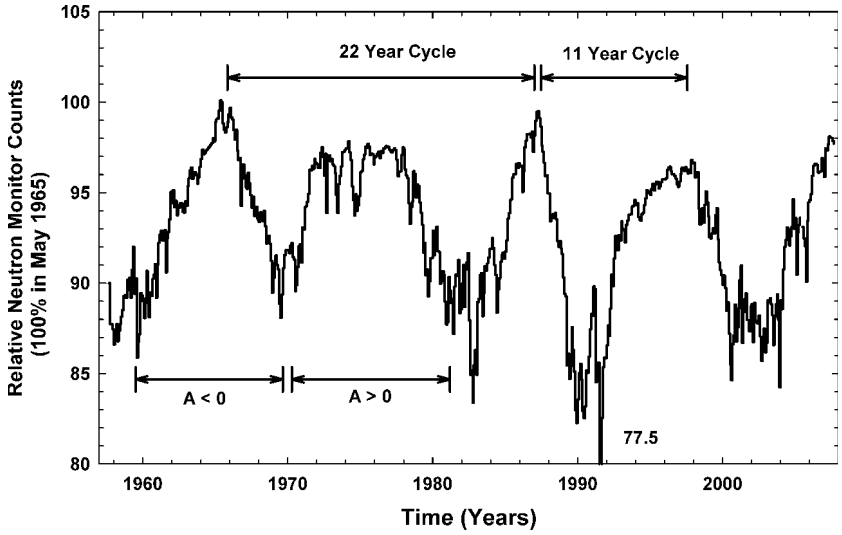

Figure 2.11: The Hermanus neutron monitor count rate (normalized to 100% in May 1965) as a function of time. The 11 and 22-year cycles are indicated and the polarity cycles labelled (A $>$ 0 and A $<$ 0) (Figure adapted from Strauss, 2010).

2.4.3 Solar cosmic ray modulation

Cosmic rays that enter the heliosphere encounter the outward flowing solar wind that carries a frozen-in turbulent magnetic field. These CR particles interact with this HMF, resulting in a reduction of the CR intensity compared to the local interstellar spectrum; this is what is known as the heliospheric modulation of CRs. The fact that the HMF influences the flux of CRs is best illustrated by the inverse correlation between the level of solar activity and the intensity of the CRs at the Earth, such as measured by neutron monitors in Figure 2.11. The effect of

the modulation during the solar cycle can also be seen in the changes in the spectra of CRs at different times during the solar cycle. Consecutive solar cycles can result in marked different CR modulation profiles (see reviews by Potgieter, 2008, 2011).

2.4.4 The transport equation in the heliosphere

The modulation of CRs in the heliosphere is described by the Parker transport equation developed by Parker (1965) and given in Equation (2.9):

$$\frac{\partial f}{\partial t} = \nabla \cdot (\mathbf{K} \cdot \nabla f - \mathbf{V} f) + \frac{1}{3p^2}(\nabla \cdot \mathbf{V})\frac{\partial}{\partial P}(P^3 f) + Q_{source} \tag{2.9}$$

where

$$\mathbf{K} = \begin{bmatrix} K_{\parallel} & 0 & 0 \\ 0 & K_{\perp} & K_A \\ 0 & -K_A & K_{\perp} \end{bmatrix} \tag{2.10}$$

is the HMF-aligned diffusion tensor explained further in Chapter 5.3. Here $\mathbf{V}$ is the solar wind velocity, P the rigidity and $f(\mathbf{r}, P, t)$ the distribution function of CRs at position $\mathbf{r}$ and at time t (see also e.g., Potgieter and Moraal, 1985; Langner, 2000; Ferreira, 2002; Strauss, 2010). The terms in Equation (2.9) are explained as follows:

- The term on the left describes the changes in the CR modulation with time. In a steady-state this term vanishes.
- The first term on the right describes the spatial diffusion parallel and perpendicular to the averaged magnetic field, as well as the particle drifts in the background magnetic field.
- The second describes the outward particle convection due to the radially outward blowing solar wind.
- The third term gives the adiabatic energy losses.
- The last term on the right specifies possible sources of CRs inside the heliosphere (such as Jovian electrons).

2.5 Intricacies in specifying the LIS

2.5.1 Purpose of LIS studies

The LIS relate CRs inside the heliosphere to those in the ISM and play an important role in the understanding of heliospheric modulation as they provide the input spectra for these studies. Inversely, heliospheric modulation is an important factor for galactic CR studies as it provides a way of comparing lower energy CR data measured in the heliosphere to LIS calculated in the Galaxy.

2.5.2 Challenges surrounding LIS modelling

Galactic propagation models, as described in Section 2.3.3, are used to approximate the LIS. These models only produce galactic interstellar spectra (GIS) and not what is commonly known as LIS. This is due to the fact that the propagation models are limited by the minimum grid spacing they can achieve, the accuracy of the local CR sources included and the implementation of local interstellar features, such as the Local Bubble. Specifying a LIS is thus not straightforward. The question is not only what the LIS looks like, but also where it should be specified.

Generally, heliospheric transport models consider the heliopause as the modulation boundary for CRs, meaning that CRs are only modulated inside the heliosphere. There are however several reasons why the modulation boundary cannot be identical with the heliopause. The CR diffusion cannot be expected to be isotropic because of the ordered local interstellar magnetic field and the heliosphere's orientation with respect to it. The magnetic field is not homogeneous, but wrapped around and piling up in front of the heliosphere, resulting in an effective increase in the local field strength and turbulence. If a bow shock exists in the upwind direction of the heliosphere, it should further enhance the turbulence region of disturbed interstellar flow beyond the heliopause. The process of modulation may thus well begin tens of AU beyond the heliopause. For a given CR species, the LIS might not be identical to the GIS everywhere on the heliopause, due to local ISM properties such as a scale-dependently structured interstellar magnetic field, enhanced turbulence and local CR sources (Nkosi et al., 2011; Scherer et al., 2011).

The location of the heliopause itself is not certain and is variable in time. Its location is determined by the pressure balance between the outward flowing solar wind (which varies with the solar cycle) and the plasma and magnetic field properties of the local ISM. Webber and Intriligator (2011) state that Voyager 1 could possibly soon cross the heliopause, thus it may already be measuring heliopause spectra. The Voyager 1 measured spectra are much lower than any predicted LIS at low energies. Assuming that the predicted LIS are reasonably correct, implies that outside the heliopause there are still important factors to consider that may affect the LIS before the spectra reach the heliosphere and eventually the heliopause.

For this work the GIS can be considered as upper limits of the LIS and the heliopause spectra as the lower limits.

2.6 Summary

Features of CRs, the Galaxy and the heliosphere were introduced and presented in this chapter. This serves as an overview of the physical processes that need to be considered when studying the propagation of CRs from their sources to where they are observed in the heliosphere, in

particular at Earth. The diffusion model (for CR propagation in the Galaxy) and the Parker transport equation (for CR propagation in the heliosphere) were introduced as background for the models used in this study and are discussed in the following chapters.

Chapter 3

The GALPROP Code

3.1 Introduction

The Galactic Propagation code (GALPROP[1]) is a numerical tool for calculating the propagation of relativistic charged particles and the diffuse emissions produced during their propagation. The code was created with the aim to enable simultaneous predictions of all observations relevant to CR physics, including CR nuclei, electrons, positrons, γ-rays and synchrotron radiation from CR propagation calculations (Ptuskin et al., 2006; Strong et al., 2007). GALPROP is meant to take advantage of the greater computing power available, as well as the increases in the accuracy of CR, γ-ray and other observations. It incorporates current information on galactic structure, source distributions, a full nuclear reaction network and as much realistic astrophysical input as possible.

This chapter describes the GALPROP code, detailing the features and capabilities of the code relevant for this study, but also mentioning features not considered in this study, as these may be necessary for future studies.

3.2 Features and abilities of GALPROP

The GALPROP code has been designed for the propagation of CRs on either a 2D or 3D spatial grid (Strong and Moskalenko, 2001). For the 2D case the model uses a rotationally symmetric cylindrical grid for the Galaxy. The CRs are propagated in three dimensions, two spatial dimensions and momentum, giving the basic coordinates (R, z, p) where R is the galactocentric radius, z the distance from the galactic plane and p the magnitude of the total particle momentum. The distance from the Sun to the galactic centre is taken as 8.5 kpc as is standard. The propagation region is bounded by $R = R_H$ and $z = \pm z_H$, giving the containment volume, beyond which free

[1] http://galprop.stanford.edu/

escape is assumed. This halo, with halo height H, is illustrated in Figure 3.1. The 3D model uses a Cartesian grid (with coordinates (x, y, z, p)) and unlike the 2D case, which is a steady-state model, the 3D case is time-dependent to account for transient CR sources like supernovae. For both the 2D and 3D cases symmetries can be assumed and the solution be limited to only a portion of the grid, 1/8th for 3D and one half for 2D, thus saving on the memory and CPU requirements of the code if necessary. The momentum grid for both cases is logarithmically spaced.

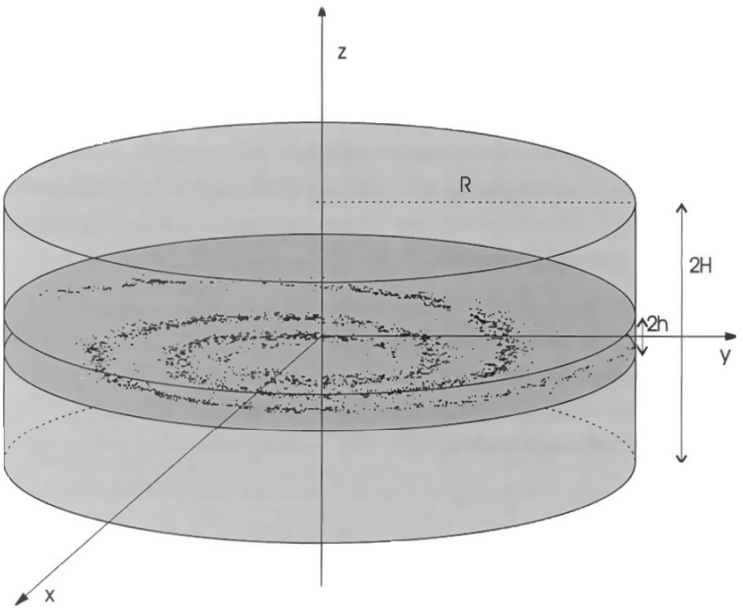

Figure 3.1: The containment volume for 2D case. The model uses a rotationally symmetric cylindrical grid, where R is the galactocentric radius and z the distance from the galactic plane. The containment volume, beyond which free escape is assumed, is bounded by $R = R_H$ and $z = \pm z_H$. Gas clouds, galactic magnetic fields and CR sources are concentrated in the volume with $z = z_h$ (Büsching, 2004).

Known limitations of GALPROP include only being able to do propagation calculations up to energies of 10^{15} eV (the energy limit assumed for acceleration of CR at SNRs), only scales larger than about 10 pc can be implemented (depending on computer power) and the magnetic field is treated as random for synchrotron emission (Strong et al., 2007). The diffusion coefficient is not spatially dependent and it is parameterised by a single coefficient instead of a tensor.

3.3 Physics in GALPROP

GALPROP solves the transport equations with a given source distribution and boundary conditions for all CR species taken into account. The basic spatial propagation mechanisms are diffusion and convection, while in momentum space energy loss and diffusive reacceleration are considered. Fragmentation, secondary particle production and energy losses are computed using realistic distributions for the interstellar gas and radiation fields (Moskalenko et al., 2002).

The propagation equation, described in Chapter 2.3 with Equation (2.8), is solved in the form:

$$\frac{\partial \psi}{\partial t} = Q(\mathbf{r}, p) + \nabla \cdot (D_{xx} \nabla \psi - \mathbf{V}\psi) + \frac{\partial}{\partial p}\left[p^2 D_{pp} \frac{\partial}{\partial p} \frac{1}{p^2}\psi + \frac{p}{3}(\nabla \cdot \mathbf{V})\psi - \dot{p}\psi\right] - \frac{1}{\tau_f}\psi - \frac{1}{\tau_r}\psi \quad (3.1)$$

where $\psi = \psi(\mathbf{r}, p, t)$ is the density per unit of total particle momentum, $Q(\mathbf{r}, p)$ is the source term, D_{xx} is the spatial diffusion coefficient, $\mathbf{V}$ is the convection velocity, $\dot{p}$ is the momentum loss rate, τ_f is the timescale for fragmentation and depends on the total spallation cross-section (Strong et al., 2007) and τ_r the timescale for radioactive decay. Reacceleration is described as diffusion in momentum space and is determined by the coefficient D_{pp} (Moskalenko and Strong, 1998). Catastrophic losses can be included via τ_f and Q (the loss of primaries due to spallation serves as the source of secondaries) (Strong et al., 2007). For electrons and positrons, the same propagation equation is valid when the appropriate energy loss terms (ionisation, bremsstrahlung, inverse Compton, synchrotron) are used (Moskalenko and Strong, 1998; Strong and Moskalenko, 1998).

The spatial diffusion coefficient is assumed to be independent of position. For the case where reacceleration is not considered, the spatial diffusion coefficient is taken as:

$$D_{xx} = \beta K_0 (\rho/\rho_0)^{\delta} \quad (3.2)$$

where $\delta = \delta_1$ for rigidity $< \rho_0$ (the reference rigidity), $\delta = \delta_2$ for rigidity $> \rho_0$ and the factor $\beta = v/c$ (Moskalenko and Strong, 1998).

The convection speed $V(z)$ is assumed to be parallel to the z-axis and to increase linearly with distance from the plane, $dV/dz > 0$ for all $z > 0$ and $z < 0$, this implies a constant adiabatic energy loss. The speed at $z = 0$ is considered to be $V(0) = 0$ (Moskalenko et al., 2002).

The source term Q includes both the direct production of primary energetic particles accelerated from the thermal background in galactic sources (such as SNRs) and the contribution to the nuclei via the processes of nuclear fragmentation and radioactive decay of heavier nuclei. The spallation part of the source term in the propagation equation depends on all progenitor species and their energy dependent cross-sections. In general, it is assumed that the spallation products have the same kinetic energy per nucleon as the progenitor. Cosmic ray sources are assumed to be concentrated near the galactic disk and to have a radial distribution similar to SNRs in the Galaxy. The distribution of CR sources is chosen to reproduce the CR distribution determined by analysing EGRET γ-ray data. The distribution is assumed to be the same for all CR primaries and is given by:

$$Q(R, z) = Q_0 \left(\frac{R}{R_\odot}\right)^{\alpha_{distr}} \exp\left(-\beta \frac{R - R_\odot}{R_\odot} - \frac{|z|}{0.2\,\mathrm{kpc}}\right) \quad (3.3)$$

where Q_0 is a normalisation constant, $R_\odot = 8.5\,\mathrm{kpc}$, $\alpha_{distr} = 0.5$ and $\beta = 1.0$ (Ptuskin et al., 2006; Strong et al., 2007).

The injection spectrum of nuclei is assumed to be a power-law in momentum, $Q(p) \propto p^{-\alpha}$ for the injected particle density and may contain a break in the power-law if required (Strong and Moskalenko, 2001; Strong et al., 2007).

Energy loss processes for nucleons, ionisation and Coulomb interactions, are included. Processes included for energy losses by electrons are ionisation, Coulomb interactions, as well as the production of bremsstrahlung, inverse Compton and synchrotron radiation. Also included are K-capture and electron stripping processes (via τ_f and Q). Synchrotron emission and γ-rays are computed using interstellar gas data (for pion decay and bremsstrahlung), the ISRF model (for inverse Compton radiation), and the magnetic field model (for synchrotron radiation) (Strong et al., 2007).

The interstellar hydrogen distribution used in the code is derived from HI and CO surveys and information on the ionized component. The molecular hydrogen and HI gas number densities in the galactic plane are defined in the form of tables, which are interpolated linearly. The extension of the gas distributions to an arbitrary height above the plane is performed using analytical approximations (Moskalenko and Strong, 1998).

Recent extensions to GALPROP include a dark matter package (Strong et al., 2007), however, this is beyond the scope of this study.

3.4 Numerical implementation in GALPROP

The numerical solution of the transport equation is based on a Crank-Nicolson implicit second-order scheme. The processes are described by differential operators in the propagation equation and these operators are implemented as finite differences in the numerical scheme. The processes given in the terms of Equation (3.1), diffusion, reacceleration, convection and energy loss, are all written as finite differences for each dimension (R, z, p) in order to use the Crank-Nicholson implicit method to solve the equations (Strong and Moskalenko, 1998, 2006). The finite differences for $\partial\psi_i/\partial t$ are given by:

$$\frac{\partial \psi_i}{\partial t} = \frac{\psi_i^{t+\Delta t} - \psi_i^t}{\Delta t} \tag{3.4}$$

with ψ_i^t the differential density at position i and time t. Discretising $\psi_i^{t+\Delta t}$ and ψ_i^t, to get the time averages for the Crank-Nicholson implicit method, then gives:

$$\frac{\psi_i^{t+\Delta t} - \psi_i^t}{\Delta t} = \frac{\alpha_1 \psi_{i-1}^{t+\Delta t} - \alpha_2 \psi_i^{t+\Delta t} + \alpha_3 \psi_{i+1}^{t+\Delta t}}{2\Delta t} + \frac{\alpha_1 \psi_{i-1}^{t} - \alpha_2 \psi_i^{t} + \alpha_3 \psi_{i+1}^{t}}{2\Delta t} + Q_i \tag{3.5}$$

with all terms functions of (R, z, p) and the α's are determined by the specific process for which the equation is computed. These finite-differencing coefficients are calculated and the propagation equation is then solved numerically. The coefficients for the finite-differencing scheme in two spatial dimensions and one momentum dimension are given in Table 3.1, where $P_i^j = p_i - p_j$, $V > 0$ for $z > 0$, $V < 0$ for $z < 0$ and $\frac{dV}{dz} > 0$.

Table 3.1: Finite-differencing coefficients for two spatial dimensions and one momentum dimension. Derivations for the coefficients can be found in Strong and Moskalenko (2006).

Process	Coordinate	$\alpha_1/\Delta t$	$\alpha_2/\Delta t$	$\alpha_3/\Delta t$
Diffusion	R	$D_{xx}\frac{2R_i-\Delta R}{2R_i(\Delta R)^2}$	$D_{xx}\frac{2R_i}{R_i(\Delta R)^2}$	$D_{xx}\frac{2R_i+\Delta R}{2R_i(\Delta R)^2}$
	z	$\frac{D_{xx}}{(\Delta z)^2}$	$\frac{2D_{xx}}{(\Delta z)^2}$	$\frac{D_{xx}}{(\Delta z)^2}$
Convection	$z > 0$	$\frac{V(z_{i-1})}{(\Delta z)}$	$\frac{V(z_i)}{(\Delta z)}$	0
	$z < 0$	0	$\frac{-V(z_i)}{(\Delta z)}$	$\frac{-V(z_{i+1})}{(\Delta z)}$
	p	0	$\frac{1}{3}\frac{dV}{dz}\frac{p_i}{P_i^{i+1}}$	$\frac{1}{3}\frac{dV}{dz}\frac{p_{i+1}}{P_i^{i+1}}$
Diffusive reacceleration	p	$-\frac{D_{pp,i}-D_{pp,i-1}}{(P_{i-1}^i)^2}$ $+\frac{2}{P_{i-1}^i}\left(\frac{D_{pp,i}}{P_{i-1}^{i+1}}+\frac{D_{pp,i-1}}{p_{i-1}}\right)$	$-\frac{D_{pp,i}-D_{pp,i-1}}{(P_{i-1}^i)^2}$ $+\frac{2D_{pp,i}}{P_i^{i+1}}\left(\frac{1}{P_i^{i+1}}+\frac{1}{P_{i-1}^i}\right)$ $+\frac{2D_{pp,i}}{P_{i-1}^i p_i}$	$\frac{2D_{pp,i+1}}{P_{i-1}^{i+1}P_i^{i+1}}$
Energy loss	p	0	$-\dot{p}_i/P_i^{i+1}$	$-\dot{p}_{i+1}/P_i^{i+1}$
Fragmentation	R, z, p	0	$1/3\tau_f$	0
Radioactive decay	R, z, p	0	$1/3\tau_r$	0

In the Crank-Nicholson implicit method used to solve Equation (3.1), the updating scheme is then:

$$\psi_i^{t+\Delta t} = \psi_i^t + \frac{\alpha_1}{2}\psi_{i-1}^{t+\Delta t} - \frac{\alpha_2}{2}\psi_i^{t+\Delta t} + \frac{\alpha_3}{2}\psi_{i+1}^{t+\Delta t} + \frac{\alpha_1}{2}\psi_{i-1}^t - \frac{\alpha_2}{2}\psi_i^t + \frac{\alpha_3}{2}\psi_{i+1}^t + Q_i\Delta t \qquad (3.6)$$

which gives the tridiagonal system of equations:

$$-\frac{\alpha_1}{2}\psi_{i-1}^{t+\Delta t} + (1+\frac{\alpha_2}{2})\psi_i^{t+\Delta t} - \frac{\alpha_3}{2}\psi_{i+1}^{t+\Delta t} = \frac{\alpha_1}{2}\psi_{i-1}^t - (1-\frac{\alpha_2}{2})\psi_i^t + \frac{\alpha_3}{2}\psi_{i+1}^t + Q_i\Delta t \qquad (3.7)$$

and the system of equations is then solved for $\psi_i^{t+\Delta t}$ by means of the Thomas algorithm (see e.g., Hattingh, 1998). This method applies to a one-dimensional case and is unconditionally stable for all α and Δt. The application to two or three spatial and one momentum dimension requires a generalisation, but a straightforward expansion to more dimensions implies solving large matrix equations. Instead, the altering direction implicit method (ADI) is used (see also

Potgieter, 1984), in which the implicit solution is applied to each dimension in turn. Each iteration then uses just the operator (see Table 3.1) for that dimension so the Thomas algorithm, solving the tri-diagonal system, can still be used.

The three spatial boundary conditions $\psi(R_h, z, p) = 0$, $\psi(R, +z_h, p) = 0$ and $\psi(R, -z_h, p) = 0$, are imposed on each iteration. According to Strong and Moskalenko (1998), no boundary conditions are required at $R = 0$ or in p. The grid intervals used are linear in R and z, but logarithmically spaced in p. Although the model is symmetric around $z = 0$ the solution is generated for $-z_h < z < z_h$ since this is required for the tri-diagonal system to be valid (Strong and Moskalenko, 1998).

The nuclear reaction network is solved starting at the heaviest nuclei considered, solving the propagation equation for this nucleus, computing all the resulting secondary source functions for the spallation products and proceeding to the next nucleus in the series to be propagated, namely $A - 1$. The procedure is repeated down to $A = 1$, then secondary electrons, positrons and lastly antiprotons. In this way all secondary, tertiary and higher reaction products are automatically accounted for. To be accurate for all isotopes, especially for the cases of β^- decay, the whole process loop is repeated twice or more (Strong and Moskalenko, 2001; Strong et al., 2007).

The solution of the propagation equation starts with a large timestep, corresponding to the largest timescales in CR propagation, then the size of the steps are reduced successively until the smallest timestep, corresponding to the shortest timescale, is reached. The criteria for progressing to the next smaller timestep is that the numerical solutions reach a steady solution. Each consecutive timestep is reduced by a fixed factor and this part of the timestep calculation is designated timestep mode 1. After the smallest timestep is reached, propagation can continue with this size timestep for a certain number of iterations. This allows for stochastic supernova events. This phase is designated timestep mode 2 (Strong and Moskalenko, 2006). Spectra of all species on the chosen grid and the γ-ray and synchrotron sky maps are output in a standard astronomical format, FITS[2], for presentation and comparison to data (Strong et al., 2007).

3.5 The Galdef file

The Galdef file is the main input file in the GALPROP code for specifying the adjustable parameters for the individual model runs. An example Galdef file, as used in this study, is given in Appendix A. The Galdef file consists of a list of parameters either specifying a certain value, indicating which models describing physical processes are to be used, turning on propagation or sources of CR species, or adjusting the accuracy and resource usage of the code. The following paragraphs describe the purpose of each parameter or parameter set as discussed by Strong

[2] `http://fits.gsfc.nasa.gov`

and Moskalenko (2006). The line numbers (as used in Appendix A) for each set of parameters discussed are given as well as the typical values used by Ptuskin et al. (2006).

Lines 5 to 18:

```
n_spatial_dimensions = 2
r_min                =00.0    min r
r_max                =20.00   max r
dr                   = 1.0    delta r
z_min                =-4.0    min z
z_max                =+4.0    max z
dz                   = 0.1    delta z
x_min                =  0.0   min x
x_max                =+15.0   max x
dx                   =  0.2   delta x
y_min                =  0.0   min y
y_max                =+15.0   max y
dy                   =  0.2   delta y
```

Lines 5 to 18 determine the number of the spatial dimensions and the size of the spatial grids. The 2D or 3D spatial grid is chosen by setting *n_spatial_dimensions* to either 2 or 3. For the 2D case (a rotationally symmetric cylindrical grid), the grid size is given by *r_min*, *r_max*, *z_max* and *z_min*, with *dr* and *dz* determining the size of the cells in the grid. For the 3D case (a Cartesian grid), the grid size is given by *z_max*, *z_min*, *x_max*, *x_min*, *y_max* and *y_min*, with cell size given by *dz*, *dx* and *dy*.

Lines 24 to 26:

```
Ekin_min             =1.0e1  min kinetic energy per nucleon (MeV)
Ekin_max             =1.0e7  max kinetic energy per nucleon
Ekin_factor          =1.3        kinetic energy per nucleon factor
```

Lines 24 to 26 determine the size and grid spacing of the kinetic energy per nucleon. *Ekin_min* and *Ekin_max* give the size of the grid and *Ekin_factor* gives the spacing on a logarithmic scale with $E_{kin}(0) = E_{kin\,min}$ and $E_{kin}(i) = E_{kin\,min} \times E^{i}_{kin\,factor}$.

Lines 30 to 44:

```
E_gamma_min          = 1.e0    min gamma-ray energy (MeV)
E_gamma_max          = 1.e8    max gamma-ray energy (MeV)
E_gamma_factor       = 1.4     gamma-ray energy factor
integration_mode     = 1       integr.over part.spec.: =1-old E*logE; 0=1-PL analyt.
nu_synch_min         = 1.0e6   min synchrotron frequency (Hz)
nu_synch_max         = 1.0e10  max synchrotron frequency (Hz)
nu_synch_factor      = 2.0         synchrotron frequency factor
long_min             =  0.50   gamma-ray intensity skymap longitude minimum (deg)
long_max             =359.50   gamma-ray intensity skymap longitude maximum (deg)
lat_min              =-89.50   gamma-ray intensity skymap latitude  minimum (deg)
lat_max              =+89.50   gamma-ray intensity skymap latitude  maximum (deg)
d_long               =  1.00   gamma-ray intensity skymap longitude binsize (deg)
d_lat                =  1.00   gamma-ray intensity skymap latitude  binsize (deg)
```

Lines 30 to 44 contain variables for adjusting the γ-ray and synchrotron skymaps produced by GALPROP, features not used in this study.

Lines 46 to 49:

```
D0_xx               = 2.2e+28         diffusion coefficient at reference rigidity
D_rigid_br          = 3.0e3           reference rigidity for diffusion coefficient in MV
D_g_1               = 0.000000e+00    diffusion coefficient index below reference rigidity
D_g_2               = 6.000000e-01    diffusion coefficient index above reference rigidity
```

Lines 46 to 49 determine the spatial diffusion coefficients over the rigidity range. *D0_xx* gives the diffusion coefficient, K_0, at the reference rigidity determined by *D_rigid_br*. The value at other energies are given by $D = \beta K_0(\rho/D_{rigid\,br})^{D_{g1}}$ for rigidity $<$ *D_rigid_br* and $D = \beta K_0(\rho/D_{rigid\,br})^{D_{g2}}$ for rigidity $>$ *D_rigid_br*. *D_g_1* and *D_g_2* are the diffusion coefficient indices below and above the reference rigidity respectively.

Lines 50 to 55:

```
diff_reacc          = 0       0=no reacc.; 1,2=incl.diff.reacc.; -1==beta^3 Dxx;
                                          11=Kolmogorov+damping; 12=Kraichnan+damping
v_Alfven            = 0.0     Alfven speed in km s-1
damping_p0          = 1.e6    MV -some rigidity (where CR density is low)
damping_const_G     = 0.02    a const derived from fitting B/C
damping_max_path_L  = 3.e21   Lmax~1 kpc, max free path
```

Lines 50 to 55 contain parameters for turning on diffusive reacceleration in the propagation, the value of the Alfvén speed, or the MHD wave damping model. These parameters were not used in this study.

Lines 57 to 59:

```
convection          =0       1=include convection
v0_conv             =0.      km s-1        v_conv=v0_conv+dvdz_conv*dz
dvdz_conv           =3.      km s-1 kpc-1  v_conv=v0_conv+dvdz_conv*dz
```

Lines 57 to 59 determine the inclusion of convection in the propagation, with *v0_conv* giving the convection velocity at $z = 0$ and *dvdz_conv* the gradient of the convection velocity assumed to be linear in z.

Lines 61 to 65:

```
nuc_rigid_br        =4.0e4       reference rigidity for nucleus injection index in MV
nuc_g_1             =2.30        nucleus injection index below reference rigidity
nuc_g_2             =2.15        nucleus injection index index above reference rigidity
inj_spectrum_type   = rigidity   rigidity||beta_rig||Etot nucleon injection spectrum type
```

Lines 61 to 65 control the nucleus injection spectrum, with *inj_spectrum_type* determining whether the spectrum is defined as a power-law in rigidity, $\beta\times$rigidity or total energy. The reference rigidity for a break in the power-law is given by *nuc_rigid_br*, with *nuc_g_1* and *nuc_g_2* giving the spectral indices of the nucleus injection spectrum below and above the reference rigidity, respectively.

Lines 67 to 71:

```
electron_g_0         =2.40     electron injection index below electron_rigid_br0
electron_rigid_br0   =4.0e3    reference rigidity0 for electron injection index in MV
electron_g_1         =2.40     electron injection index below reference rigidity
electron_rigid_br    =1.0e3    reference rigidity for electron injection index in MV
electron_g_2         =2.4      electron injection index index above reference rigidity
```

Lines 67 to 71 contain the electron injection spectrum with *electron_rigid_br0* and *electron_rigid_br* giving the two breaks in the power-law, *electron_g_0*, *electron_g_1* and *electron_g_2* giving the spectral indices of the electron injection spectrum below, between and above the reference rigidities respectively. These electron variables were not used in this study as only nuclei were considered.

Lines 73 to 79:

```
He_H_ratio           =0.11     He/H of ISM, by number
X_CO                 =0.4E20,0.4E20,0.6E20,0.8E20,1.5E20,10.0E20,10.0E20,10.0E20,10.0E20
       conversion factor from CO integrated temperature to H2 column density
       for CO rings  0.0 - 1.5 - 3.5  -  5.5 -  7.5 -  9.5  -  11.5 -  13.5 -  15.5  -  50 kpc
fragmentation        =1        1=include fragmentation
momentum_losses      =1        1=include momentum losses
radioactive_decay    =1        1=include radioactive decay
K_capture            =1        1=include K-capture
```

Lines 73 to 79 include parameters relating to additional factors that influence the propagation of CR in the Galaxy. These factors include the ratio of helium and hydrogen in the interstellar gas given by *He_H_ratio* and the radial dependence of $X_{CO} = N(H_2)/W_{CO}$, X_{CO} being the ratio of Hydrogen to CO in the interstellar gas, given by the nine values corresponding to each of the nine galactocentric CO rings. Fragmentation, momentum losses, radioactive decay and K-capture are also included by their respective parameters.

Lines 81 to 88:

```
start_timestep       =1.0e7
end_timestep         =1.0e2
timestep_factor      =0.25
timestep_repeat      =20     number of repeats per timestep in  timetep_mode=1
timestep_repeat2     =0      number of timesteps in timetep_mode=2
timestep_print       =10000  number of timesteps between printings
timestep_diagnostics =10000  number of timesteps between diagnostics
control_diagnostics  =0      control detail of diagnostics
```

Lines 81 to 88 determine the values for the timesteps in the model calculations. The solution of the propagation equation starts with a large timestep given by *start_timestep* (corresponding with the largest timescales in CR propagation), then the size of the steps are reduced successively until the smallest timestep given by *end_timestep* (corresponding to the shortest timescales) is reached. The factor by which each consecutive timestep is reduced is determined by *timestep_factor* and the amount of iterations of the timestep for each *timestep_factor* by

timestep_repeat. This part of the timestep calculation is designated by *timestep_mode = 1*. After the smallest timestep is reached, *timestep_mode = 2*, propagation can continue with this size timestep for a number of iterations determined by *timestep_repeat2*, which are important for time-dependent 3D calculations.

Line 90:

```
network_iterations   = 2      number of iterations of entire network
```

Line 90 gives the amount of times the entire nuclear network is calculated through in the model run. The nuclei fragmentation network starts with the largest atomic mass number, A, and works downwards in A. For the species of the same A, the largest Z is calculated first. A second or third iteration may be required to correctly model contributions, produced by β^- decay from unstable isotopes, to isotopes calculated earlier in the network.

Lines 92 to 100:

```
prop_r               = 1  1=propagate in r (2D)
prop_x               = 1  1=propagate in x (2D,3D)
prop_y               = 1  1=propagate in y (3D)
prop_z               = 1  1=propagate in z (3D)
prop_p               = 1  1=propagate in momentum
use_symmetry         = 0  0=no symmetry, 1=optimized symmetry, 2=xyz symmetry by copying(3D)
vectorized           = 0  0=unvectorized code, 1=vectorized code
```

Lines 92 to 100 control the propagation in the spatial directions and in momentum for the 3D and the 2D cases. Propagation can be limited to only certain dimensions or a combination of dimensions, with *prop_r* for radial direction, *prop_x* for the x direction, *prop_y* for the y direction, *prop_z* for the z direction and *prop_p* for propagation in momentum. For the 3D case symmetry can be assumed for the solution of the propagation equation and the solution limited to only 1/8th of the grid, thus saving on the memory and CPU requirements of the code.

Lines 102 to 119:

```
source_specification = 0     2D::1:r,z=0 2:z=0  3D::1:x,y,z=0 2:z=0 3:x=0 4:y=0
source_model         = 1     0=zero 1=parameterized  2=Case&B 3=pulsars 4= 5=S&Mattox 6=S&Mattox with cutoff
source_parameters_1  = 0.5   model 1:alpha
source_parameters_2  = 1.0   model 1:beta
source_parameters_3  = 20.0  model 1:rmax
n_cr_sources         = 0     number of pointlike cosmic-ray sources   3D only!
cr_source_x_01       = 10.0  x position of cosmic-ray source 1 (kpc)
cr_source_y_01       = 10.0  y position of cosmic-ray source 1
cr_source_z_01       = 0.1   z position of cosmic-ray source 1
cr_source_w_01       = 0.1   sigma width  of cosmic-ray source 1
cr_source_L_01       = 1.0   luminosity of cosmic-ray source 1
```

Lines 102 to 119 specify the CR sources in the model for the 3D case. With *source_model*, one of various source distributions can be chosen. Setting *source_model* to 1 produces a parameterised source described by $R^{\alpha}\exp(-\beta R)$ with cutoff at $R = r_{max}$ and r_{max} given by *source_parameters_3*, α by *source_parameters_1* and β by *source_parameters_2*. Point-like sources can also be included for the 3D case by specifying *n_cr_sources*. Their positions are given by *cr_source_x*, *cr_source_y* and *cr_source_z* for each point source, the σ width of the source by *cr_source_w* and its luminosity by *cr_source_L*.

Lines 122 to 128:

```
SNR_events           = 0         handle stochastic SNR events
SNR_interval         = 1.0e4     time interval in years between SNR in 1 kpc^-3 volume
SNR_livetime         = 1.0e4     CR-producing live-time in years of an SNR
SNR_electron_sdg     = 0.00      delta electron source index Gaussian sigma
SNR_nuc_sdg          = 0.00      delta nucleus  source index Gaussian sigma
SNR_electron_dgpivot = 5.0e3     delta electron source index pivot rigidity (MeV)
SNR_nuc_dgpivot      = 5.0e3     delta nucleus  source index pivot rigidity (MeV)
```

Lines 122 to 128 are used to generate CR sources in the form of SNRs. The parameter *SNR_events*, lets the model generate SNRs random in space and time, this is only for the 3D case and *timestep_mode* = 2. The spatial distribution of SNR follows *source_specification* and the time-dependence is determined by *SNR_interval*, giving the rate of SNRs produced, and *SNR_livetime*, giving the time in years for which a SNR remains a 'live' acceleration source for CRs. *SNR_electron_sdg* and *SNR_nuc_sdg* allow for the dispersion of the electron source spectral index and the nuclei source spectral index respectively. In the case of dispersion of the source spectral indices, *SNR_electron_dgpivot* and *SNR_nuc_dgpivot* define the rigidity about which the spectra pivot.

Lines 130 to 135:

```
HI_survey            = 9                  HI survey 8=orig 8 rings  9=new 9 rings
CO_survey            = 9                  CO survey 8=orig 8 rings  9=new 9 rings
B_field_model        = 050100020          bbbrrrzzz    bbb=10*B(0)  rrr=10*rscale zzz=10*zscale
ISRF_file            = MilkyWay_DR0.5_DZ0.1_DPHI10_RMAX20_ZMAX5_galprop_format.fits ,input ISRF file
ISRF_factors         = 1.0,1.0,1.0        ISRF factors for IC calculation: optical, FIR, CMB
```

Lines 130 to 135 add physical components of the Galaxy, such as HI and CO rings, the ISRF and the perpendicular component of the galactic magnetic field, to the code. *HI_survey* and *CO_survey* set the amount of rings assumed. Either eight or nine rings can be included. The choice of the ISRF dataset is given by *ISRF_file*, with *ISRF_factors* giving the scaling factors for inverse Compton radiation from three separate components: optical, FIR and CMB. *B_field_model* specifies the perpendicular component of the magnetic field according to the law $B = (b_0/10) \times \exp(R/(r_0/10) - z/(z_0/10))$ in microgauss, by specifying the scaling factors b_0, r_0 and z_0.

Lines 137 to 141:

```
proton_norm_Ekin     = 1.00e+5  proton kinetic energy for normalisation (MeV)
proton_norm_flux     = 4.90e-9  to renorm nuclei/flux of protons at norm energy (cm^-2 sr^-1 s^-1 MeV^-1)
electron_norm_Ekin   = 34.5e3   electron kinetic energy for normalisation (MeV)
electron_norm_flux   = .40e-9   flux of electrons at normalisation energy (cm^-2 sr^-1 s^-1 MeV^-1)
```

Lines 137 to 141 give the kinetic energy values, *proton_norm_Ekin* and *electron_norm_Ekin*, and the flux values, *proton_norm_flux* and *electron_norm_flux*, for the normalisation of the proton and electron fluxes to the measured flux values.

Lines 143 to 245:

```
max_Z                = 28     maximum number of nucleus Z listed
use_Z_1              = 1
.
.
.
use_Z_30             = 0
iso_abundance_01_001 = 1.06e+06   H
.
.
.
iso_abundance_28_064 =   0.3039
```

Lines 143 to 245 list the nuclei to be propagated in the model and used in the nuclear reaction network and the source abundance of each, respectively. The number of nuclei is given by *max_Z* and the nuclei to be used is specified by setting the appropriate *use_Z* to 1. The source abundance of the nuclei is given by the corresponding *iso_abundance* parameter. These abundances are relative values and the final CR fluxes are normalized so that the proton flux is specified by *proton_norm_flux*.

Lines 247 and 248:

```
total_cross_section  = 2      total cross section option: 0=L83 1=WA96 2=BP01
cross_section_option = 012    100*i+j  i=1: use Heinbach-Simon C,O->B j=kopt j=11=Webber, 21=ST
```

Lines 247 and 248 give options for choosing a method for determining total fragmentation cross-sections.

Lines 250:

```
t_half_limit         = 1.0e4 year - lower limit on radioactive half-life for explicit inclusion
```

Line 250 gives the lower limit on the radioactive half-life of species for explicit inclusion in the calculation.

Lines 252 to 257:

```
primary_electrons    = 1
secondary_positrons  = 1
secondary_electrons  = 1
secondary_antiproton = 2   1=uses nuclear scaling; 2=uses nuclear factors by Simon2008
tertiary_antiproton  = 1
secondary_protons    = 1
```

Lines 252 to 257 determine the inclusion of primary electrons, secondary electrons, positrons, secondary protons, secondary antiprotons and tertiary antiprotons in the propagation. Any of these species can be left out and will then not be propagated.

Lines 259 to 264:

```
gamma_rays           = 0    1=compute gamma rays, 2=compute HI,H2 skymaps separately
pi0_decay            = 0    1= old formalism 2=Blattnig et al.
IC_isotropic         = 1    1,2= compute isotropic IC: 1=compute full, 2=store skymap components
IC_anisotropic       = 1    1,2,3= compute anisotropic IC: 1=full, 2=approx., 3=isotropic
bremss               = 0    1=compute bremsstrahlung
synchrotron          = 0    1=compute synchrotron
```

Lines 259 to 264 include options for calculating additional effects and skymaps. These effects include computing γ-rays, secondary positrons and electrons from pion decay, as well as isotropic and anisotropic inverse Compton scattering. Skymaps for diffuse galactic γ-rays, bremsstrahlung, synchrotron radiation and diffuse γ-rays can also be calculated.

Lines 266 to 292:

```
comment              = the dark matter (DM) switches and user-defined parameters
DM_positrons         = 0   1=compute DM positrons
.
.
.
DM_int9              = 1
```

Lines 266 to 292 list the parameters controlling the dark matter calculations included in GALPROP. These considerations may be useful for studying CRs produced by dark matter in the Galaxy, but are beyond the scope of this study.

Lines 294 to 298:

```
output_gcr_full      = 0  output full galactic cosmic ray array if 1, only at earth for 0
warm_start           = 0  read in nuclei file and continue run
verbose              = 0  verbosity: 0=min,10=max <0: selected debugs
test_suite           = 0  run test suite instead of normal run
```

Lines 294 to 298 contain some output and run-time options such as verbosity and testing.

3.6 Summary

The GALPROP code is designed for modelling of the propagation of CRs in the Galaxy. The code incorporates a vast set of astrophysical input and is considered the most complete model of its type to date. The parameters in the code can easily be specified and implemented without changing the numerics of the model itself. New developments and alternative theories can be included as required.

Throughout this study the GALPROP code is used to model CR propagation through the Galaxy. Three parameters of specific importance for the parameter study, presented in Chapter 6, were described in this chapter: the source spectral index (α), the spectral index of the diffusion coefficient (δ) and the magnitude of the diffusion coefficient at a given reference rigidity (K_0).

Chapter 4

Verification of 2D GALPROP Code

4.1 Introduction

Before a parameter study using the GALPROP code is to be conducted, the code has to be implemented and tested by comparing the output with known results. In this chapter results obtained by Ptuskin et al. (2006), using the GALPROP code to calculate LIS, are reproduced and presented. The effect of different grid spacings is also tested. The results from examination into the prospective use of the 3D case of the GALPROP code are discussed and shortcomings in the current 3D implementation highlighted.

4.2 Reproduction of published GALPROP results

The GALPROP code presented by Moskalenko and Strong (1998) and discussed in Chapter 3 was used, among others, by Strong and Moskalenko (2001) and Ptuskin et al. (2006) to model the propagation of CRs in the Galaxy in the 2D case to produce LIS. The set of LIS found by Ptuskin et al. (2006) using a plain diffusion model in their study is reproduced here. The GALPROP code was run using the same parameter set (defined by the Galdef file 999726 as given in Appendix A) and LIS for protons, electrons, Carbon, positrons and anti-protons were calculated, as well as the CR ratios B/C and Be^{10}/Be^{9}.

The free parameters, adjusted in the parameter study of the next chapter, were also kept at the same values as chosen by Ptuskin et al. (2006). These parameters are the source spectral index ($\alpha = 2.15$ above the reference rigidity and $\alpha = 2.30$ below) the spectral index of the diffusion coefficient ($\delta = 0.6$ above the reference rigidity and $\delta = 0.0$ below) and the magnitude of the diffusion coefficient at particle rigidity 4 GV ($K_0 = 2.2{\times}10^{28}\,\mathrm{cm^2 s^{-1}}$). Figures 4.1 and 4.2 give the resulting LIS and CR ratios obtained by using these parameters. The results were found to be identical to those presented by Ptuskin et al. (2006) for the plain diffusion model.

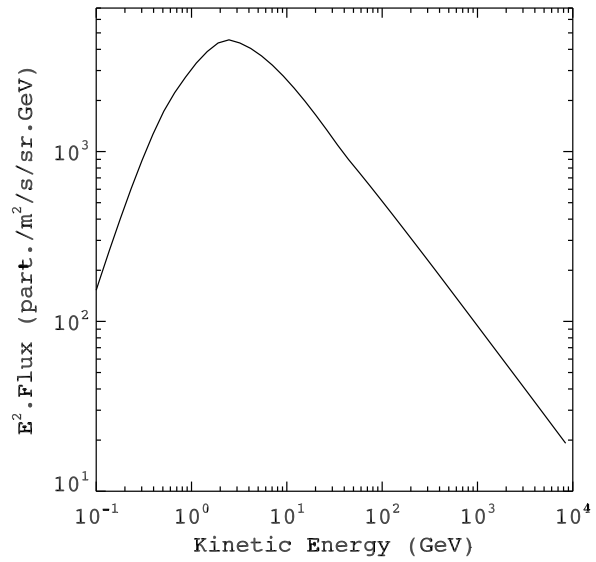

(a) Proton LIS

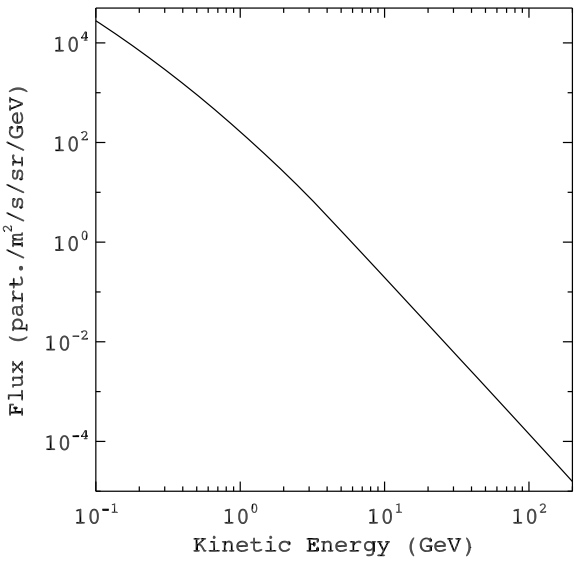

(b) Electron LIS

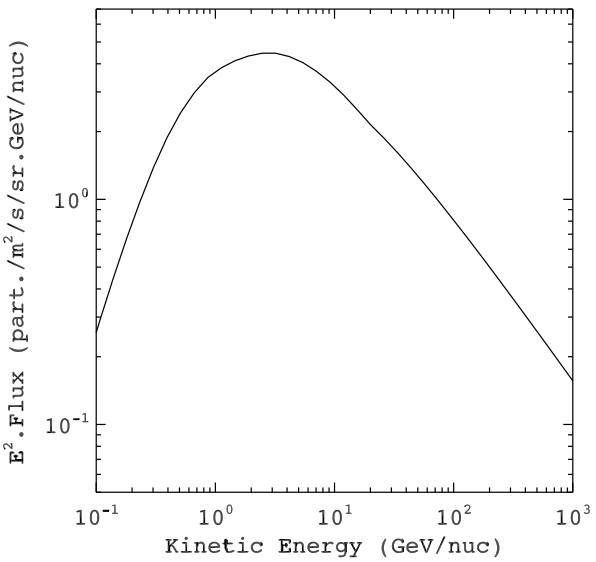

(c) Carbon LIS

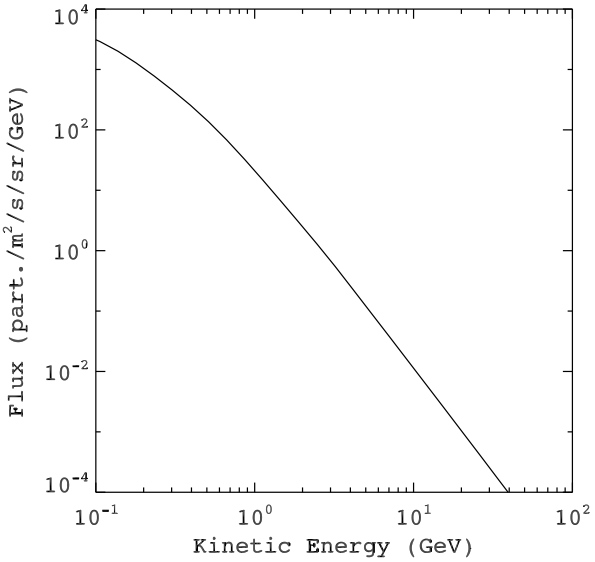

(d) Positron LIS

Figure 4.1: The proton, electron, Carbon and positron LIS respectively reproduced for comparison with Ptuskin et al. (2006) using the GALPROP code and the plain diffusion model defined by the Galdef file in Appendix A. The LIS are found to be identical to those by Ptuskin et al. (2006).

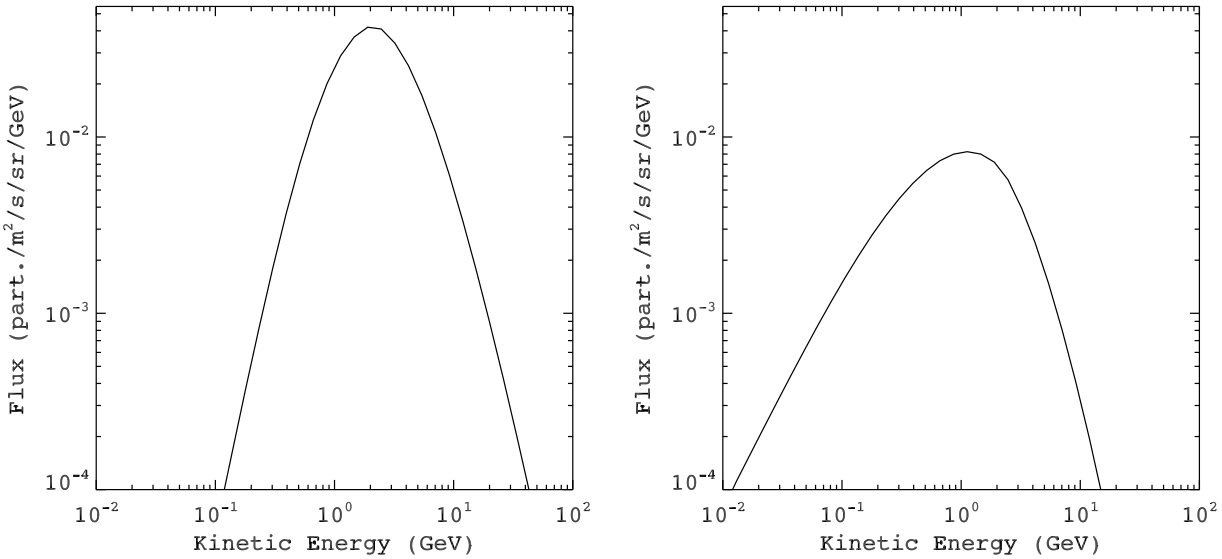

(a) Secondary antiproton LIS

(b) Tertiary antiproton LIS

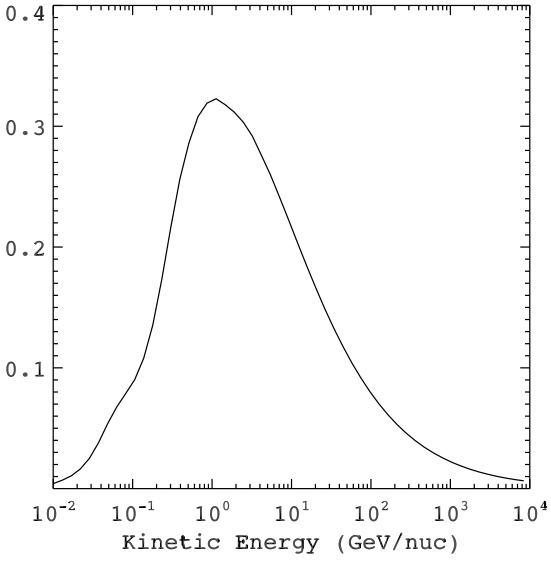

(c) B/C ratio

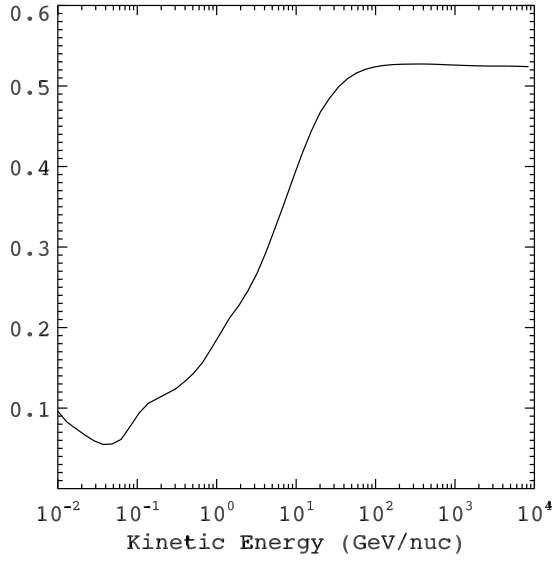

(d) Be^{10}/Be^{9} ratio

Figure 4.2: The secondary and tertiary antiproton LIS and the B/C and Be^{10}/Be^{9} CR ratios respectively reproduced for comparison with Ptuskin et al. (2006) using the GALPROP code and the plain diffusion model defined by the Galdef file in Appendix A. The LIS are found to be identical to those by Ptuskin et al. (2006).

4.3 Numerical stability test

The numerical stability of the GALPROP code was tested for the 2D case by using different grid sizes in the r-axis and the z-axis, respectively. The code was run with the same physical parameters as described above in Section 4.2. The first set of models were run with changed grid sizes in r, default size being dr = 1.00 kpc, by setting dr = 1.00, 0.50, 0.25, 0.10 and 0.05 kpc for the r-axis with keeping dz = 0.100 kpc for the z-axis. The second set of models were run with changed grid sizes in z, default size being dz = 0.10 kpc, by setting dz = 0.100, 0.050, 0.025 and 0.010 kpc for the z-axis while keeping dr = 1.00 kpc for the r-axis.

The differences in the resulting LIS were compared by calculating the ratios between the default grid size runs and the varied grid size runs. The ratios calculated in this manner for these two sets of models are presented in Figures 4.3 and 4.4, showing that decreasing the grid sizes does not significantly change the flux values obtained. The differences are all within 2% of the default values, except for the B/C ratios calculated with smaller z-axis grid sizes, which show at most a 4% change at lower energies. Decreasing the grid size does not seem to affect the stability of the numerical method, nor does it improve the accuracy of the model further as the effect on the flux values is insignificant.

4.4 3D Implementation

Ideally, studying the effect of CR point sources on the primary and secondary CR components requires a 3D galactic propagation code, as the 2D case cannot be used to specify CR point sources. Before applying the 3D GALPROP code to the CR point source problem, the feasibility of using the 3D implementation had to be tested. The behaviour of a single CR point source was investigated by comparing the output of the code at different times in the time-dependent solution of the propagation equation. It is expected that a single point source, switched on for some initial timesteps, may show a spherical spread of CR intensity out into the Galaxy over time.

The standard data output from GALPROP is not sufficient to compare the CR distribution, produced by the point source, at different times. Therefore an addition was made to the code to print out the appropriate values at the required time intervals.

The CR distribution due to the point source is found not to be spherical, but pyramidal in shape. This effect is illustrated in Figure 4.5, where a single point source placed arbitrarily in the plane of the galaxy (placed at $z = 0$ kpc, $y = 0$ kpc, and $x = 5$ kpc using a Cartesian coordinate system in the 3D code). The propagation of the CR intensity on the x-y plane is shown. The CR intensity can be seen to propagate outward from the source over time. As seen in the figures the CR flux decreases in a pyramidal shape as one moves away from the source

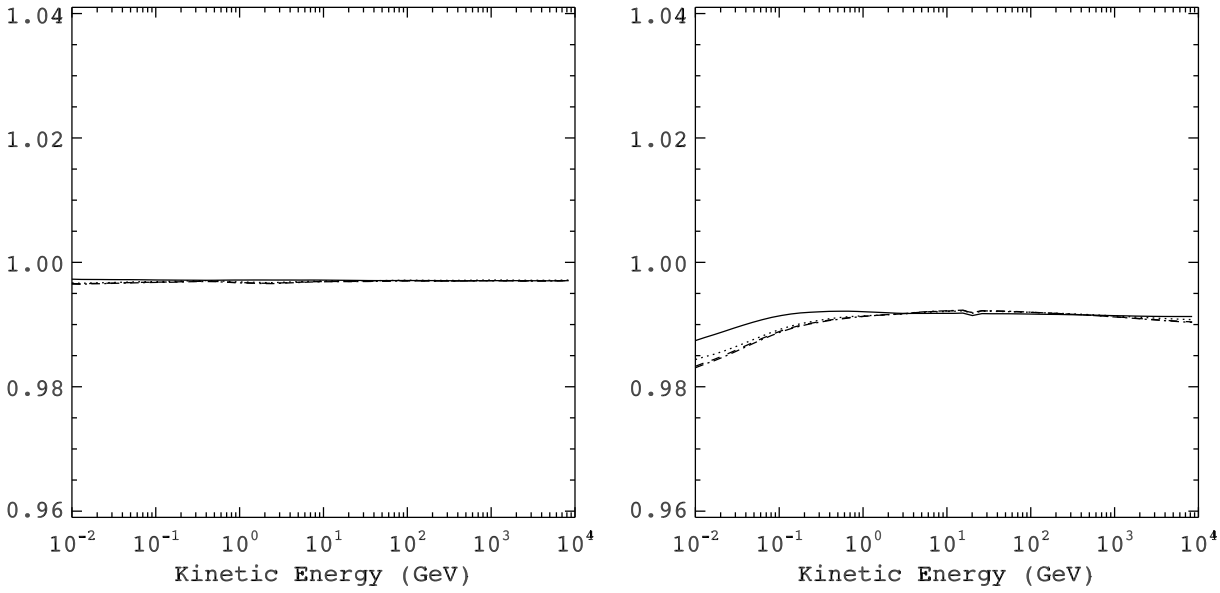

(a) Proton LIS

(b) Electron LIS

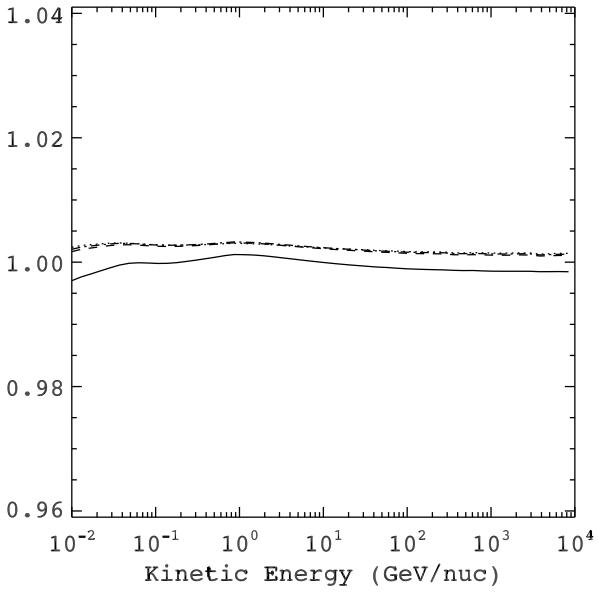

(c) B/C ratio

Figure 4.3: Ratio between the flux obtained by the default gird sizes and the values obtained from different sized r-axis grids, for proton and electron LIS and the B/C CR ratio. The lines show the flux value ratios between the default r-axis grid size run (dr = 1.00 kpc) and the values from the varied r-axis grid size runs. Solid line: dr = 0.50 kpc, dotted line: dr = 0.25 kpc, dashed line: dr = 0.10 kpc and dot-dash line: dr = 0.05 kpc.

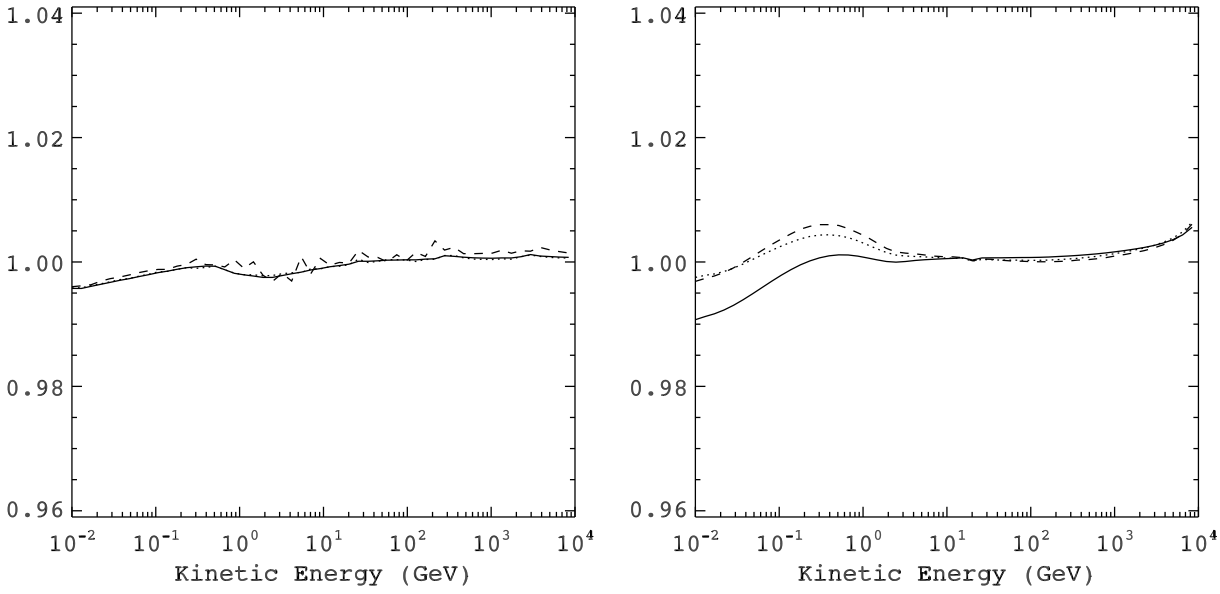

(a) Proton LIS

(b) Electron LIS

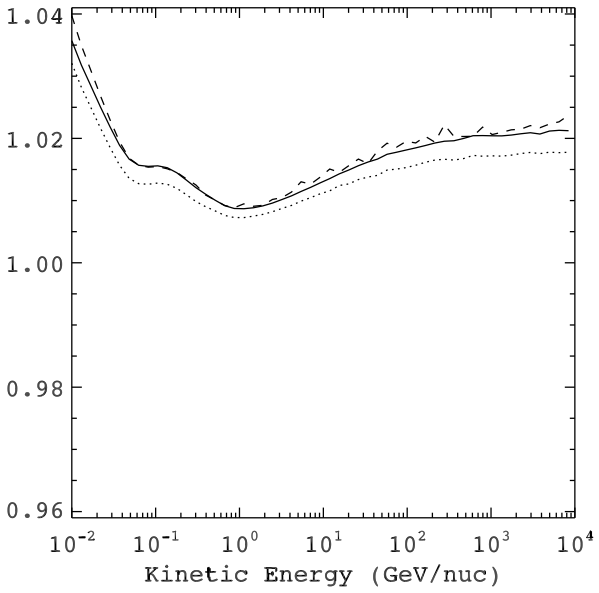

(c) B/C ratio

Figure 4.4: Ratio between the flux obtained by the default gird sizes and the values obtained from different sized z-axis grids, for proton and electron LIS and the B/C CR ratio. The lines show the flux value ratios between the default z-axis grid size run (dz = 0.10 kpc) and the values from the varied z-axis grid size runs. Solid line: dz = 0.050 kpc, dotted line: dz = 0.025 kpc and dashed line: dz = 0.100 kpc.

point. This spread is sharply pyramidal after only a few timesteps (Figures 4.5 (a) and (d)) and becomes more rounded after more timesteps (Figures 4.5 (b), (c), (e) and (f)), but remains far from spherical for the entire time interval considered. This is likely due to the Cartesian coordinate system and the ADI method used with the Crank-Nicholson implicit method in the numerical scheme. The current numerical scheme is thus unsuited to calculate the 3D case of galactic propagation accurately, as it does not give the correct spherical propagation of CRs in the Galaxy as is expected. Future releases of GALPROP may implement a different numerical method, such as a fully explicit scheme, that will not give this inaccuracy.

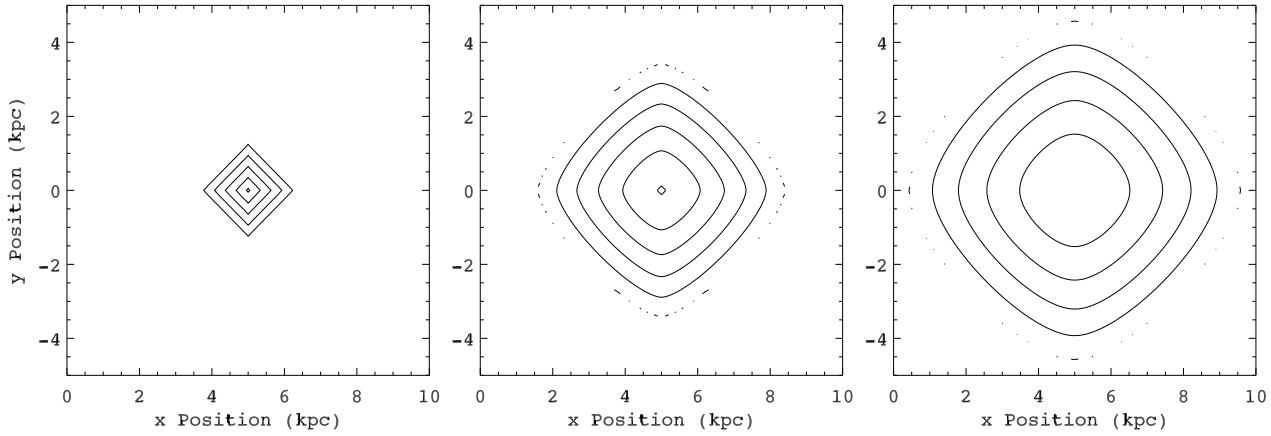

(a) First timestep: 1.526×10^2 yrs **(b)** 300th timestep: 4.578×10^4 yrs **(c)** 920th timestep: 1.404×10^5 yrs

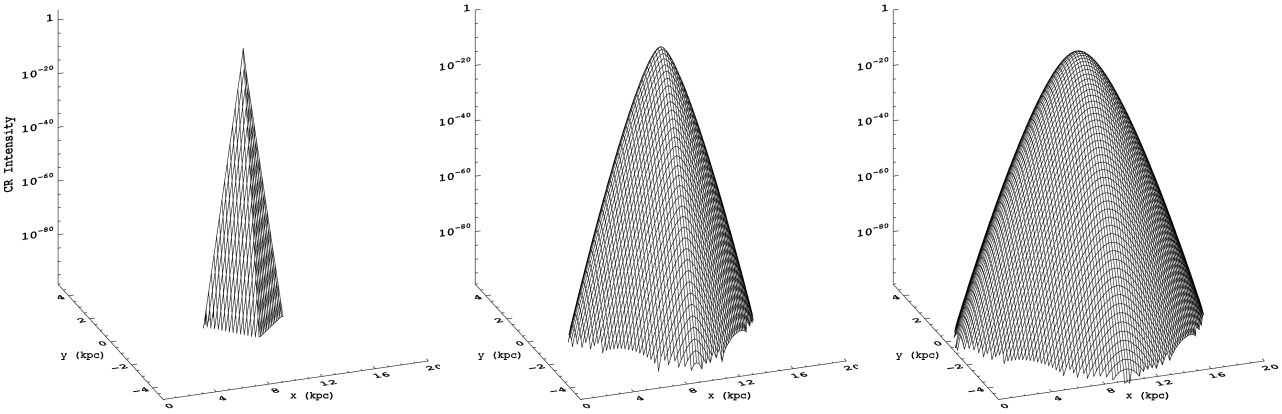

(d) First timestep: 1.526×10^2 yrs **(e)** 300th timestep: 4.578×10^4 yrs **(f)** 920th timestep: 1.404×10^5 yrs

Figure 4.5: Contour and surface plots showing CR intensity for propagation from a single point source after three time periods: a timestep of 152.6 yr (panels (a) and (d)), halfway through the propagation after 4.578×10^4 yrs (panels (b) and (e)) and at the end of the considered propagation time, 1.404×10^5 yrs (panels (c) and (f)). The point source is placed arbitrarily in the plane of the galaxy, at $z = 0$ kpc, $y = 0$ kpc, and $x = 5$ kpc. Propagation on the x-y plane is shown, with the x-axis and y-axis having the same scale in kpc.

4.5 Summary and conclusions

The LIS obtained by Ptuskin et al. (2006) using the GALPROP code were reproduced. Using the same parameter and code set, identical LIS were produced and it can thus be assumed that the code was implemented correctly. The GALPROP code was tested by decreasing the grid sizes to determine the numerical stability. The variations due to the smaller grid sizes were found to be negligible and also did not improve the accuracy of the model.

The 3D implementation of the GALPROP code was also tested with the aim of using the 3D code for this and further studies. Unfortunately, the present version (v.50.1p) of the 3D code was found to be insufficient, leading to the non-spherical spread from a single CR point source. The 2D implementation will thus be used for the rest of this study, but future studies are recommended with the 3D code when GALPROP has been updated to address these shortcomings.

Chapter 5

Aspects of Heliospheric Modulation

5.1 Introduction

Modulation studies in the heliosphere are done with various approximations of the CR transport equation, first derived by Parker (1965), and discussed in Section 2.4.4. The full description of the modulation problem requires the determination of the CR intensity as a function of three spatial coordinates, time and energy. Because of the complexity, the full numerical solution of the transport equation is seldom used. Various levels of approximations can be made to simplify the numerical solution. Not all approximations are equally suited for all problems in heliospheric CR transport and the simplified numerical models cannot be applied to every situation. This chapter compares the widely used force field approximation (see e.g., Caballero-Lopez and Moraal, 2004) and a 2D drift model (e.g., Potgieter, 1984; Potgieter and Moraal, 1985; Langner, 2000; Ferreira, 2002).

5.2 Force field approximation

The force field formalism was originally derived by Gleeson and Axford (1968a,b) (see also Gleeson and Urch, 1973). The equation for the evolution of the omnidirectional part of the CR distribution function f in terms of particle momentum p is a continuity equation of the form:

$$\frac{\partial f}{\partial t} + \nabla \cdot \mathbf{S} + \frac{1}{p^2}\frac{\partial}{\partial p}\left(p^2 \langle \dot{p} \rangle f\right) = Q \tag{5.1}$$

where

$$\mathbf{S} = 4\pi p^2 \left(C\mathbf{V}f - \mathbf{K} \cdot \nabla f\right) \tag{5.2}$$

is the differential current density, $\mathbf{V}$ is the solar wind velocity, C is the Compton-Getting coefficient with $C = -(1/3)\partial \ln(f)/\partial \ln(p)$. $\mathbf{K}(\mathbf{r}, P, t)$ is the diffusion tensor which contains elements $\kappa_{\parallel}(\mathbf{r}, P, t)$ and $\kappa_{\perp}(\mathbf{r}, P, t)$. The diffusion tensor also contains $\kappa_T = \beta P/(3B)$ which describes

gradient, curvature and neutral sheet drift effects. The adiabatic rate of momentum loss in the solar wind is given by $\langle \dot{p} \rangle = (p/3)\mathbf{V} \cdot \nabla f / f$. The transport equation can thus be written as:

$$\frac{\partial f}{\partial t} + \nabla \cdot (C\mathbf{V}f - \mathbf{K} \cdot \nabla f) + \frac{1}{3p^2}\frac{\partial}{\partial p}\left(p^3 \mathbf{V} \cdot \nabla f\right) = Q. \tag{5.3}$$

The force field approximation simplifies Equation (5.3) by assuming that there are no additional sources of CRs within the heliosphere; it is in a quasi-steady state; the adiabatic energy loss is approximated and there are no drifts (e.g., Herbst et al., 2010). Equation (5.3) thus reduces to:

$$C\mathbf{V}f - \mathbf{K} \cdot \nabla f = \text{const.} = 0 \tag{5.4}$$

and also assuming spherical symmetry gives:

$$CVf - \kappa \frac{\partial f}{\partial r} = 0 \tag{5.5}$$

where r is the heliocentric distance, V is the solar wind speed and the diffusion tensor $\mathbf{K}$ has been reduced to a single radial coefficient κ. This assumption of spherical symmetry removes the structure of the heliospheric magnetic field in the equation. The force field approximation is also a weak-modulation approximation that is mostly accurate only in the inner heliosphere (Caballero-Lopez and Moraal, 2004).

When C is introduced explicitly, Equation (5.5) becomes a first order partial differential equation:

$$\frac{Vp}{3}\frac{\partial f}{\partial p} + \kappa \frac{\partial f}{\partial r} = 0. \tag{5.6}$$

It can be written in the form:

$$\frac{\partial f}{\partial r} + \frac{VP}{3\kappa}\frac{\partial f}{\partial P} = 0 \tag{5.7}$$

where momentum p has been changed to rigidity P. The coefficient of the second term has the dimensions of potential per unit length, or a field, hence the name force field.

The rigidity $P_b = P_b(r, P)$ is obtained by integrating the characteristic equation from the initial phase space point (r, P) to the point (r_b, P_b) at the outer boundary of the heliosphere r_b. If the diffusion coefficient is separable in the form:

$$\kappa(r, P) = \beta \kappa_1(r) \kappa_2(P) \tag{5.8}$$

the solution is given by:

$$\int_P^{P_b(r,P)} \frac{\beta(P')\kappa_2(P')}{P'} dP' = \int_r^{r_b} \frac{V(r')}{3\kappa_1(r')} dr' = \phi(r) \tag{5.9}$$

called the force field parameter. When $\kappa_2 \propto P$ and $\beta \approx 1$ the solution reduces to the widely used form:

$$P_b - P = \phi \tag{5.10}$$

so that the force field parameter becomes a rigidity loss. Since it has the dimensions of a potential, it is also called the force field potential. Typical values of ϕ vary from 300 to 1000 MV, from solar minimum to solar maximum conditions. It can also be specified in eV according to: $\Phi = Ze\phi$. The force field rigidity loss in the form of Equation (5.10) applies only to the special case of relativistic particles ($\beta = 1$) and a rigidity dependent diffusion coefficient ($\kappa \propto P$), but in all other cases:

$$P_b - P = f(\phi, P). \tag{5.11}$$

For cases where κ must be independent of rigidity, ϕ is not a rigidity loss and Equation (5.9) gives a fractional loss of the form:

$$\frac{\Delta P}{P} = e^{\phi} - 1. \tag{5.12}$$

In such cases ϕ alone is insufficient to describe the modulation and does not have the dimensions of a potential. The full force field parameter from Equation (5.9) is given by:

$$\frac{\phi(r)}{\beta\kappa_2} = \frac{1}{3}\int_r^{r_b} \frac{V}{\kappa} dr \tag{5.13}$$

and is dimensionless.

Equation (5.3) can be written in the equivalent form:

$$\frac{\partial f}{\partial t} + \nabla \cdot (\mathbf{V}f - \mathbf{K} \cdot \nabla f) - \frac{1}{3p^2}(\nabla \cdot \mathbf{V})\frac{\partial}{\partial p}\left(p^3 f\right) = Q. \tag{5.14}$$

Using similar approximations as for Equation (5.3): $Q = 0$, $\partial f/\partial t = 0$, the last term on the right $= 0$ and spherical symmetry, results in the so called convection-diffusion equation:

$$Vf - \kappa\frac{\partial f}{\partial r} = 0. \tag{5.15}$$

The solution is given by:

$$f = f_b e^{-M}, \quad \text{where} \quad M = \int_r^{r_b} \frac{V}{\kappa} dr. \tag{5.16}$$

The integral M is called the modulation function and it follows from Equation (5.9) that it is related to the force field parameter ϕ by:

$$M = \frac{3\phi(r)}{\beta\kappa_2} \tag{5.17}$$

and M is a dimensionless quantity, while ϕ is a dimensional parameter (see also, Potgieter, 1984).

The relationship between the force field and the convection-diffusion formalisms provide two ways to describe the same process. Figure 5.1 (a) shows a boundary spectrum f_{LIS} that is modulated along a horizontal line as a rigidity loss of some function of ϕ, while the convection diffusion approach describes it as a vertical reduction in intensity given by M. Modulation actually consists of both intensity reduction and adiabatic energy loss, as represented by the inclined line in Figure 5.1 (a).

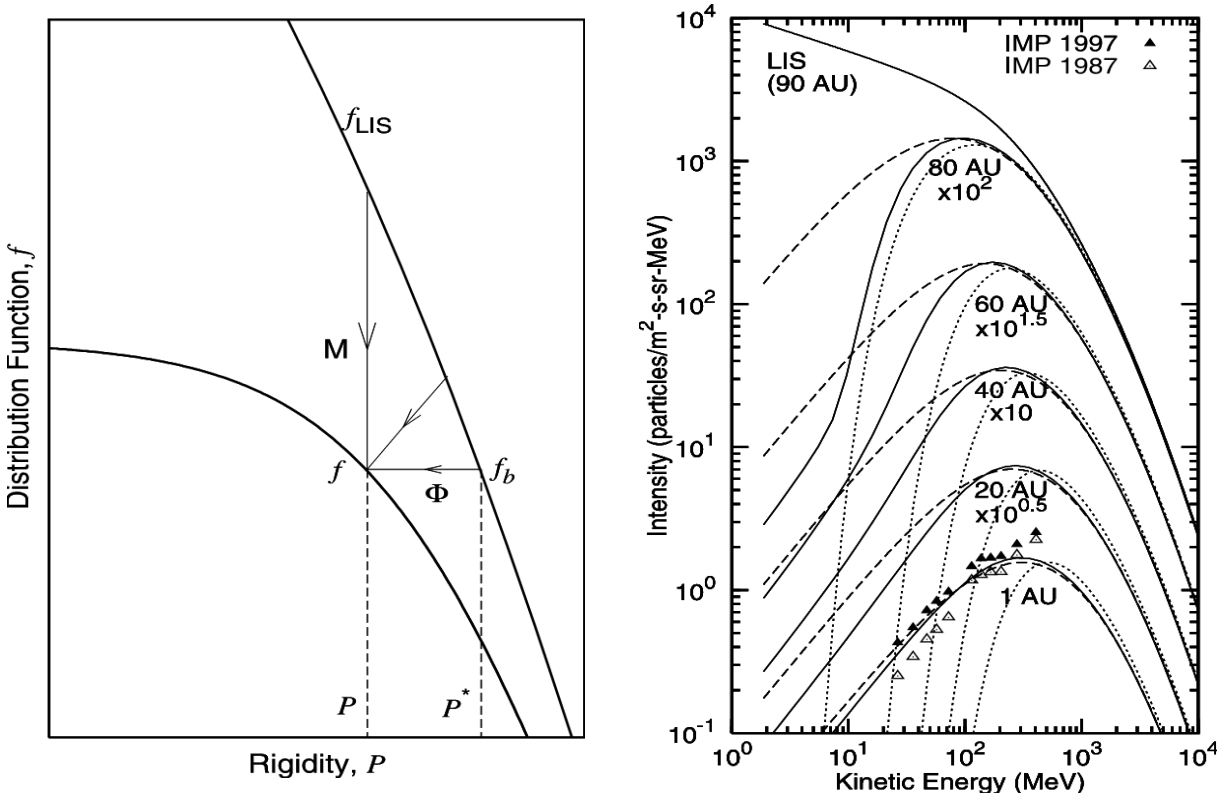

(a) Force field and convection-diffusion solutions.

(b) Comparing numerical solutions.

Figure 5.1: Panel (a) Graphical representation of the description of the modulation with the force field solution (horizontal line) and the convection-diffusion solution (vertical line). The sloped line represents the actual modulation as a combination of intensity reduction and energy loss. Panel (b) Full numerical solution of a 1D transport equation (solid lines), force field solution (dashed lines) and convection-diffusion solution (dotted lines) for CR protons in a heliosphere with $r_b = 90\,\mathrm{AU}$, $V = 400\,\mathrm{km/s}$, and $\phi\ (1\,\mathrm{AU}) = 407\,\mathrm{MV}$ (Caballero-Lopez and Moraal, 2004).

The comparison of the force field and the convection-diffusion approximations to a full numerical solution of 1D transport equation as done by Caballero-Lopez and Moraal (2004) is shown in Figure 5.1 (b). At 1 AU (Earth) this comparison shows that the force field solution is a better approximation to the full solution than the convection-diffusion solution, because the force field includes energy loss effects. With increasing radial distance the force field gets progressively worse, whereas the convection diffusion solution improves. The reason for this is that the force field increasingly under-estimates adiabatic energy loss at larger radial distances and the energy losses becoming smaller, increasingly favour the convection-diffusion approximation. However, both are not satisfactorily used from the Earth to the modulation boundary.

It is evident that even a 1D numerical approach is much better to use because it gives the full adiabatic energy loss at Earth (not just an approximation) and more realistic levels of modulation below a few hundred MeV with increasing radial distance. This 1D numerical model, based on the Crank Nicholson numerical scheme is in fact less cumbersome to solve than the full force field approach. However, the 1D approach does not describe any drifts (charge sign dependence) and is in this respect far inferior to drift models for the modulation of CRs in the heliosphere.

There is thus little reason to continue to use the force field approach in the Astrophysics and the Space Weather communities, when heliospheric modulation details are of importance. Ideally the force field approximation should be replaced with a drift model as described in the next section.

5.3 Drift approach

A more accurate approach of the numerical solution of the Parker transport equation is the 2D drift model. This approach includes an important aspect of CR transport in the heliosphere, namely particle drifts along the HMF. The background magnetic field in the heliosphere affects the CR transport by contributing drift motions associated with gradients and curvature in the HMF. It also contributes effects due to abrupt changes in the field's direction, such as the HCS (e.g., Potgieter, 1984; Ferreira, 2002; Langner, 2004; Potgieter, 2011).

2D Drift model

The Parker transport equation in Section 2.4.4 can be rewritten in terms of momentum p in the following form:

$$\frac{\partial f}{\partial t} = -\left(\mathbf{V} + \langle \mathbf{v}_D \rangle\right) \cdot \nabla f + \nabla \cdot (\mathbf{K} \cdot \nabla f) + \frac{1}{3}(\nabla \cdot \mathbf{V}) \frac{\partial f}{\partial \ln p} + \frac{1}{p^2} \frac{\partial}{\partial p} \left(p^2 K_p \frac{\partial f}{\partial p} \right) + Q_{source} \quad (5.18)$$

with $f(\mathbf{r}, p, t)$ the distribution function of the CRs at position $\mathbf{r}$, with momentum p and at time t. The term on the left gives time-dependent changes, the first term on the right is outward convection due to the solar wind with velocity $\mathbf{V}$, the second term describes the CR drifts in terms of pitch-angle averaged guiding centre drift velocity $\langle \mathbf{v}_D \rangle$, the third term describes the spatial diffusion through the diffusion tensor $\mathbf{K}$, the fourth term gives the adiabatic energy losses and gains through the solar wind divergence, the fifth term describes momentum diffusion determined by the momentum diffusion coefficient K_p and in the last term Q_{source} is for sources of CRs inside the heliosphere (Strauss, 2010). The following assumptions and approximations have to be made for the 2D implementation of the transport equation.

Assumptions and boundary conditions

In solving the transport equation it is assumed that time variations are slow and thus negligible, so that $\frac{\partial f}{\partial t} = 0$. Also it is assumed that there are no sources or sinks present inside the heliosphere, resulting in $Q_{source} = 0$.

The LIS is used as an initial condition for the entire heliosphere, described at the outer boundary of the heliosphere, $r = r_b$, as an input spectrum. At $r = r_0$ it is assumed that no particles enter or leave the Sun:

$$\left.\frac{\partial f}{\partial r}\right|_{r=r_0} = 0 \tag{5.19}$$

and at the poles it is assumed that:

$$\left.\frac{\partial f}{\partial \theta}\right|_{\theta=0,180^o} = 0 \tag{5.20}$$

The HCS is simulated in the 2D model by a 2D drift approximation. This is called the wavy current sheet model and is discussed in full by Burger and Hattingh (1995). The net flux of charged particles across the HCS is required to be zero.

The radial dependence of the solar wind for the solar minimum period is assumed as:

$$V_r(r) = 400\left\{1 - \exp\left[\frac{40}{3}(r_0 - r)\right]\right\}\,\mathrm{km.s^{-1}} \tag{5.21}$$

with r_0 the solar radius. The solar wind velocity varies with heliolatitudes as shown by Ulysses observations and this normalized latitude dependence can be described by:

$$V_\theta(\theta) = 1.5 \mp 0.5\tanh\left[\frac{2\pi}{45}(\theta - 90^o \pm \varphi)\right] \tag{5.22}$$

in the northern and southern hemisphere respectively with φ taken as 35^o. The average solar wind speed is taken as $800\,\mathrm{km.s^{-1}}$ in the fast solar wind region and as $400\,\mathrm{km.s^{-1}}$ in the slow solar wind region.

An equation for the spiral HMF derived by Parker (1958) is:

$$\mathbf{B} = \frac{B_0}{r^2}(\mathbf{e}_r - \tan\psi\mathbf{e}_\phi) \tag{5.23}$$

where $\mathbf{B}$ is the HMF with unit vector components $\mathbf{e}_r$ and $\mathbf{e}_\phi$ in the radial and azimuthal directions respectively. Here the symbol ψ gives the spiral angle which is the angle between the radial direction and the average HMF at a certain position. This spiral angle gives an indication of how tightly wound the HMF spiral is. A typical value of the spiral angle is $\psi = 45^o$ at Earth and it increases with r to about 90^o beyond 10 AU in the equatorial plane.

The magnitude of the HMF at Earth is B_0, with an average value of $B_0 \approx 5$ nT. The spiral angle is given by:

$$\psi = \tan^{-1} \frac{\Omega(r - r_0) \sin\theta}{V} \tag{5.24}$$

where Ω is the angular speed of the Sun and $r_0 = 0.005$ AU. Substituting this expression into Equation (5.23) yields the magnitude of the Parker HMF:

$$B = \frac{B_0}{r^2} \sqrt{1 + \left(\frac{\Omega(r - r_0) \sin\theta}{V} \right)^2}. \tag{5.25}$$

Several modifications to this expression have been considered (see e.g., Ferreira, 2002; Langner, 2004).

Diffusion coefficients and drifts

In a polar coordinate system the diffusion coefficient $\mathbf{K}$ in the transport equation is given by:

$$\mathbf{K} = \begin{bmatrix} K_{rr} & K_{r\theta} & K_{r\phi} \\ K_{\theta r} & K_{\theta\theta} & K_{\theta\phi} \\ K_{\phi r} & K_{\phi\theta} & K_{\phi\phi} \end{bmatrix}. \tag{5.26}$$

This can be written in a form that includes the HMF aligned diffusion coefficients $K_\parallel$, $K_\perp$ and K_A. For the full transformations see Strauss (2010):

$$\mathbf{K} = \begin{bmatrix} K_\parallel \cos^2\psi + K_{\perp r} \sin^2\psi & -K_A \sin\psi & (K_{\perp r} - K_\parallel) \cos\psi \sin\psi \\ K_A \sin\psi & K_{\perp\theta} & K_A \cos\psi \\ (K_{\perp r} - K_\parallel) \sin\psi \cos\psi & -K_A \cos\psi & K_{\perp r} \cos^2\psi + K_\parallel \sin^2\psi \end{bmatrix}. \tag{5.27}$$

The diffusion coefficients $K_\parallel$ and $K_\perp$ are the diffusion coefficients parallel and perpendicular to the HMF, respectively. $K_\perp$ is in fact two different coefficients, namely $K_{\perp r}$ and $K_{\perp\theta}$ which are perpendicular diffusion in the radial direction and perpendicular diffusion in the polar direction respectively, so that:

$$K_{rr} = K_\parallel \cos^2\psi + K_{\perp r} \sin^2\psi, \tag{5.28}$$

$$K_{\theta\theta} = K_{\perp\theta}. \tag{5.29}$$

For the perpendicular diffusion coefficient in the radial direction the simplification:

$$K_{\perp r} = aK_\parallel \tag{5.30}$$

can be made and for the perpendicular diffusion coefficient in the polar direction:

$$K_{\perp\theta} = bK_{\parallel} f(\theta) \tag{5.31}$$

with a and b constants and $f(\theta)$ a phenomenological function of θ. For a complete description see e.g., Langner (2004).

Under the assumption of weak scattering, K_A is given by:

$$K_A = \frac{\beta P}{3B} \tag{5.32}$$

where B is the average magnitude of the HMF, which is given by Equation (5.25). Sometimes a modification is applied at lower rigidities, this modified K_A is given by K_{drift}:

$$K_{drift} = (K_A)_0 \frac{\beta P}{3B} \left[\frac{(P/P_0)^2}{(P/P_0)^2 + 1} \right] \tag{5.33}$$

where $P_0 = 1$ GeV and $(K_A)_0$ is a dimensionless parameter with values between 0.0 and 1.0. This is a necessary expression to specify the guiding centre drift velocity $\langle \mathbf{v}_D \rangle$ in Equation (5.18) with:

$$\langle \mathbf{v}_D \rangle = \nabla \times K_{drift} \mathbf{e}_B. \tag{5.34}$$

Solving the equation

The transport equation simplified with the 2D drift approach is a parabolic differential equation and can be solved by the ADI method in a similar fashion as described in Chapter 3.4. For the 2D drift model the ADI method is used for two spatial and one momentum coordinate. The details of the numerical scheme and solution are discussed in full by Potgieter (1984), Potgieter and Moraal (1985), Ferreira (2002) and Langner (2004).

5.4 Features of the drift model

When comparing the features and capabilities of the force field approximation with the 2D drift approach, it is evident that the drift approach includes more physical processes than the force field. The more important process is the drift itself, which results in the modulation being charge-sign dependent and being able to handle particle charges, which is very important when considering electrons, positrons and anti-protons. It is also necessary for including the full effect of the solar polarity cycle, which has a significant impact on CRs especially during solar minimum conditions. This is denoted by A$>$ 0 and A $<$ 0, respectively (see Figure 2.9).

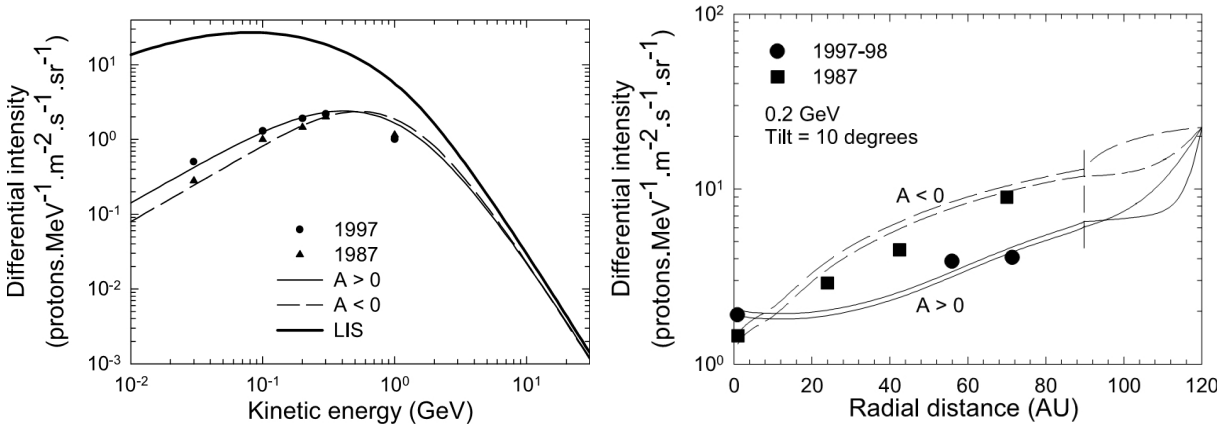

(a) Proton LIS, modulated spectra and solar minimum proton data.

(b) Proton radial intensities for both polarity cycles at solar minimum.

Figure 5.2: Panel (a) Computed differential intensities for protons as a function of kinetic energy for both polarity cycles at Earth for $\alpha_{tilt} = 10^o$ in comparison with solar minimum data for 1987 (triangles) and 1997 (filled circles). The LIS is at 120 AU, with a termination shock at 90 AU. Panel (b) Computed radial intensities for CR protons for both polarity cycles in the equatorial plane at 0.2 GeV and for a= 10^o. The LIS is specified at 120 AU. The filled circles represent A> 0 data, the squares represent A< 0 data of IMP, Pioneer 10, Voyager 1 and 2 for solar minimum conditions. The reference line denotes the position of the TS (Langner et al., 2003).

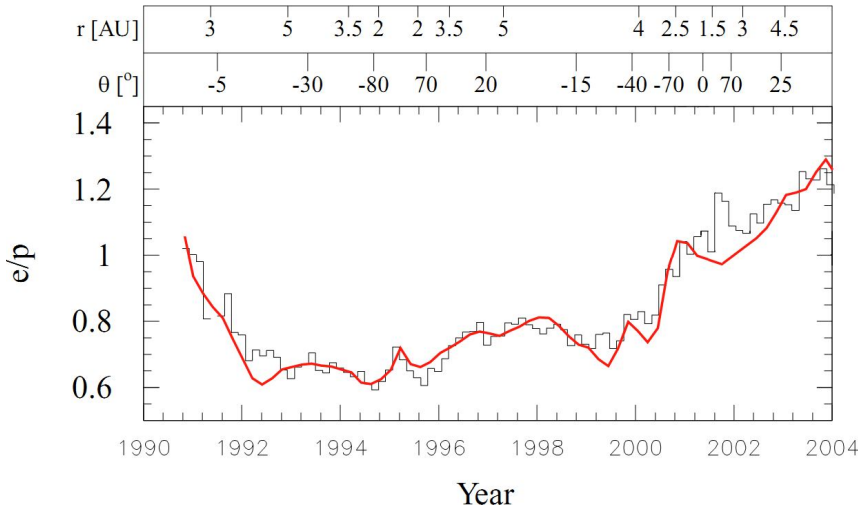

Figure 5.3: Variation of the electron to proton ratio at 2.5 GV over a 13 year time period. Binned observational data from Ulysses is overlaid with model data. The radial and latitudinal position of Ulysses is indicated in the top panel. Graph adapted from Heber and Potgieter (2006) with model results from Ferreira et al. (2003).

It follows from Figure 5.2 (a) that the CR intensities vary with consecutive solar minimum activity, giving different spectra during the two polarity periods. Drift effects become even more evident at greater radial distances, as seen in Figure 5.2 (b), where the CR profiles differ significantly between the polarity periods. The charge-sign dependence of CR modulation also has a significant effect, causing the drift directions of positive and negative particles being opposite in a given polarity period. The time varying effect on the ratio of electrons to protons is illustrated in Figure 5.3.

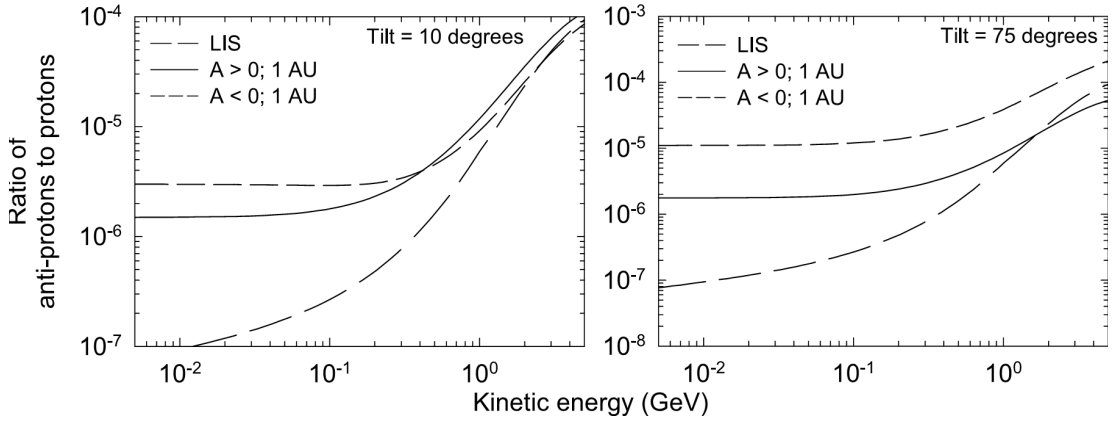

Figure 5.4: Ratio of antiprotons to protons ($\bar{p}/p$) as a function of kinetic energy in the equatorial plane at Earth for both polarity cycles (A > 0 and A < 0) with a tilt angle $\alpha_{tilt} = 10^o$ (left panel) and $\alpha_{tilt} = 75^o$ (right panel), respectively. All ratios are compared to a LIS $\bar{p}/p$ ratio (at 120 AU) as a reference (Langner and Potgieter, 2004).

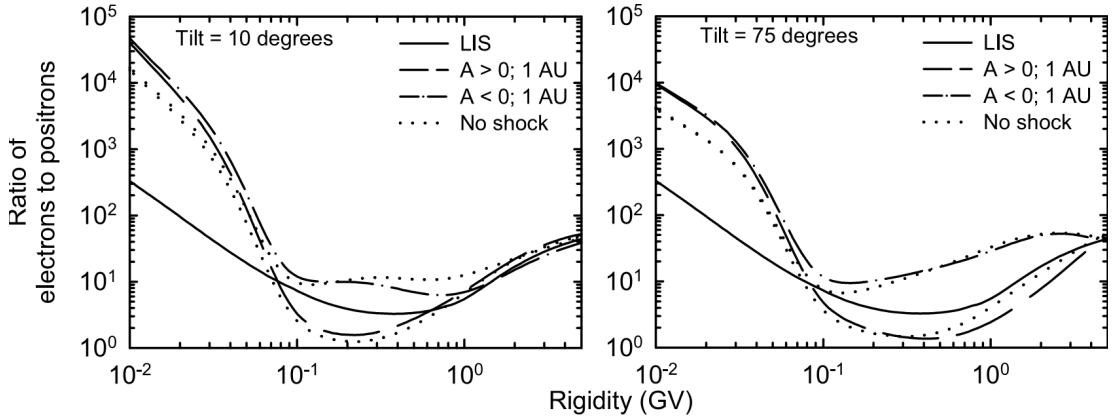

Figure 5.5: Ratio of electrons to positrons (e^-/e^+) as a function of rigidity in the equatorial plane at 1 AU for both polarity cycles (A > 0 and A < 0) and with a tilt angle $\alpha_{tilt} = 10^o$ (left panel) and $\alpha_{tilt} = 75^o$ (right panel), respectively. All ratios are compared to LIS values at 120 AU as a reference. Non-shock solutions (without a termination shock) are also shown as dotted lines (Potgieter and Langner, 2004).

Not only does the polarity cycle affect the charged particles, but solar activity also has an effect. In Figure 5.4 the difference between the ratio of antiprotons and protons during solar minimum (tilt angle $\alpha_{tilt} = 10^o$) and during solar maximum ($\alpha_{tilt} = 75^o$) are shown.

The effects on charged particles can also be seen in the ratio of positrons to electrons in Figure 5.5 which show large differences in the ratio between high and low energies. In this case it is shown how the drift effects reach a maximum between 50 MeV and a few GeV.

Unlike the force field model, the 2D drift approach has the advantage of being able to calculate the effects of modulation in the whole heliosphere and not just at 1 AU and in the equatorial plane of the solar system. Thus it can be used for data comparison from the Ulysses spacecraft as in Figure 5.6, which crossed the polar regions of the Sun, and the two Voyager spacecraft which measure heliosphere data at great radial distances, now even in the heliosheath.

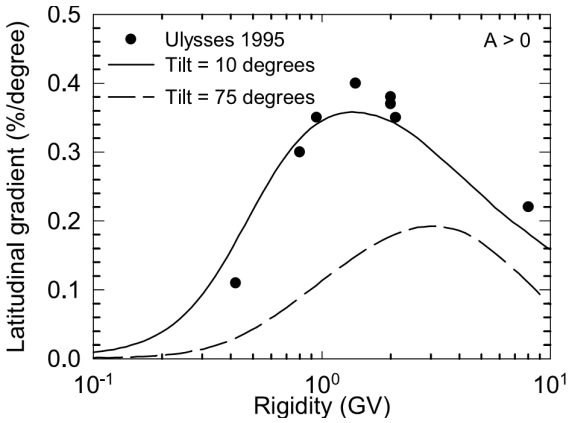

Figure 5.6: Computed latitudinal gradients, in %/degree, for the A > 0 polarity cycle at 3 AU for a= 10^o and a= 75^o between colatitudes 10^o and 90^o. Data obtained by Ulysses in 1995 (Langner et al., 2003).

5.5 Discussion and conclusions

For this study, initial attempts were made to add a 2D drift model to the GALPROP code, but because of compatibility issues (matching the Fortran code of the heliospheric drift model to the C++ code of GALRPOP), making the more complex drift model user friendly and the high numerical costs associated with separately modulating all the CR isotopes, the effort has taken much longer than anticipated. The force field approximation was chosen instead for this study, as the approximation is valid at Earth and the observations used in this study have been taken only from Earth orbiting satellites and balloon experiments. Only CR nuclei are studied and time-dependence is not considered, thus the disadvantages of the force field are largely avoided. In addition, the force field approximation has already been implemented by Strong and Moskalenko (2001) and packaged alongside the GALPROP code.

The advantage of using a force field approach is that it is very simple and straight forward to use together with the GALPROP code. The force field approximation still remains an elegant solution for modulation that works well for studies where heliospheric modulation details are of less importance.

The drift approach is considered beyond the scope of this study due to the complexity of adding it to the GALPROP code and is left for future studies. It is highly recommended for any future studies which include data or models for protons, anti-protons, electrons, positrons or CRs at lower energies, that at least the 2D drift approach is followed.

Chapter 6

Parameter Study

6.1 Introduction

Cosmic ray propagation in the Galaxy is usually numerically modelled using a 2D cylindrically symmetric model to obtain LIS for CR species (e.g., Büsching et al., 2005). Primary and secondary CR species are, however, produced by different physical processes in the Galaxy. The 2D model is limited in its capability to handle point sources of CR primaries adequately. This is due to the fact that a 2D model cannot include CR point sources, but only CR sources distributed evenly over the whole Galaxy in the angular direction ϕ, an important factor to consider for primary CR production. On the other hand, it has been shown that 2D models sufficiently describe the CR secondary component.

Therefore, if there are nearby point-like sources, the 2D code will not be adequate to describe the CR primary component originating from these sources. In this case, working with secondary, tertiary, or higher CR nuclei may thus yield a better description of galactic CR propagation than working with primary CR nuclei. Conducting a parameter study, this should be seen in the different best fit values for CR primaries and secondaries, as the flux of the secondary (and higher) CR component does not depend on the local source history (Büsching et al., 2005).

A parameter study is conducted to obtain best fit values separately for CR primaries and secondaries. This is done by using the GALPROP code to model CR propagation through the Galaxy. Three of the parameters in the 2D plain diffusion model used by Ptuskin et al. (2006) are varied: the source spectral index (α), the spectral index of the diffusion coefficient (δ) and the magnitude of the diffusion coefficient at a particle rigidity of 4 GV (K_0). This chapter gives the details of the models, parameter space and data fitting used. The best fit LIS found using the models in the parameter study are presented and compared to the LIS obtained by Ptuskin et al. (2006). The parameters giving the best fit LIS are also compared to parameter values found by Maurin et al. (2002) and Putze et al. (2009, 2010).

6.2 The GALPROP model and parameter space

The parameter study was conducted using the 2D plain diffusion model of the GALPROP code as described in Chapter 3. This model was chosen because it does not take into account reacceleration, thus simplifying the model and reducing the number of free parameters to consider. The plain diffusion model was used in cylindrical coordinates with two spatial dimensions, the galactocentric radius r and the height above the galactic plane z, with symmetry in the angular direction. The energy range over which the model was run was kept to the default range, but this study considered only data values above 4 GeV/nuc. This helps in reducing the complexity of the model by not requiring breaks in the source spectrum index or the spectral index of the diffusion coefficient at low energies. The effect of solar modulation is lower at these high energies thus any errors made in describing the modulation have less impact on the final results.

The free parameters adjusted in the model for this study are the source spectral index (α), the spectral index of the diffusion coefficient (δ) and the magnitude of the diffusion coefficient at a particle rigidity of 4 GV (K_0, with units $\mathrm{cm^2 s^{-1}}$). The parameter space over which the study was run is listed in Table 6.1. This range was chosen as to vary the free parameters over a wide range of possible values, but also to include the values obtained by Ptuskin et al. (2006).

Table 6.1: Range for the variation of the free parameters

Parameter	Min	Max	Units
α	1.5	3.5	
δ	0.1	1.0	
K_0	0.5	5.0	$10^{28}\,\mathrm{cm^2 s^{-1}}$

Initial tests have shown that the galactic wind gives only minor changes in the fluxes for rigidity above 4 GV. The velocity and gradient in the galactic wind can thus be set to zero, as to not include the effect of the wind, simplifying the model. As only values above 4 GeV/nuc were considered, no break was taken into account in the source spectral index and the reference rigidity for the diffusion coefficient was adjusted to 4 GV. The halo height of the model galaxy was fixed at 4 kpc and its radius at 20 kpc as done by Ptuskin et al. (2006). In accordance with the results of Section 4.3 on the effects of smaller grid sizes, the step size for the z-direction perpendicular to the galactic plane was kept unchanged at 0.1 kpc and at 1.0 kpc for the galactocentric radius in the numerical scheme. All the other quantities in the model were kept fixed at the values as used in the plain diffusion model defined by the Galdef file (numbered 999726) by Ptuskin et al. (2006), shown in Section 3.5 and Appendix A.

The model runs were calculated on the NWU-Potchefstroom institutional cluster using a MPI code to run the models in parallel. The full nuclear reaction network was solved over all isotopes implemented in GALPROP. Thus both primary and secondary CR species were run at the same time. Only one iteration was run over the whole nuclear network due to time constraints, thus

allowing for small errors in the computation of the nuclei produced in β^- decay as stated in Section 3.5. The error introduced by limiting the model to this one iteration was seen to be acceptably small for this study, as there would be only a small difference in the flux for some of the species. Individual CR isotope fluxes are also added to compare with the data, as most CR experiments give combined fluxes for groups of more than one isotope, resulting in a negligible change in the CR flux due to limiting the model to one iteration.

6.3 Data comparison and χ^2 test

The LIS produced by the models as described in Section 6.2 are compared to experimental CR data. The data used in this study were taken from the 11 Nov 2009 version of the CR database[1] maintained by Strong (2009). These data sets come from various CR experiments as listed in Appendix B. As explained above, only data above 4 GeV/nuc are compared to the model.

The GALPROP model calculates LIS for the different CR isotopes and not for different CR species (the different detected elements or element groups as listed in Table 6.3) and presents them separately. To be able to study the primary and secondary CRs separately, the individual CR species have to be divided up according to the fraction of secondary and primary nuclei in each species. Due to different experiments having different capabilities in measuring CR flux values, not all experiments can distinguish between different isotopes of the same element. In some cases distinction between elements of similar atomic number such as Carbon, Nitrogen and Oxygen is difficult with the instrument, therefore different isotopes of the same element cannot always be individually considered.

The restrictions imposed by the data and the mixture of secondary and primary nuclei in a given CR species have to be considered when dividing the CRs up into components of either primary or secondary CRs. To determine how the species are to be divided into different groups, the amount of secondaries and primaries in each CR isotope, as presented in Longair (2004b), is compared. The fraction of secondaries and primaries in the isotopes that make up each species are added up separately. The addition is weighted according to the known abundances of the isotopes in a species when detected at Earth, integrated over all energies. Using this method to differentiate between CR species, all the CR data and LIS can then be divided into one of three component groups: Primary CRs, Mixed CRs and Secondary CRs as described in Table 6.2 with their constituent species listed in Table 6.3.

The χ^2 test

The modelled LIS of the CR species in the three components are then compared to the experimental data using a χ^2 test. The χ^2 test is conducted by calculating χ^2 as given in Equation

[1] `http://www.mpe.mpg.de/~aws/propagate.html`

Table 6.2: CR component groups divided according to the fraction of CR secondaries

CR component group	Secondary CR fraction
Primary	$< 30\%$
Mixed	$> 30\%$ and $< 70\%$
Secondary	$> 70\%$

Table 6.3: Species composition of the three CR component groups

Primary component:	Mixed component:	Secondary component:
H	N	Be
He	C+N+O	B
C	Ne	F
O	Na	P
Mg	Al	Sc
Si	S	Ti
Ne+Mg+Si	Cl	V
Ca	K	Mn
Fe	Cr	
	Co	

(6.1), with the experimental data points given by (x_i, y_i), the model values by $F(x_i)$ and the error on y_i by Δy_i. The χ^2 values are calculated for each data point and then added up over all the considered data points for each LIS in the respective CR group.

$$\chi^2 = \sum_i \left[\frac{F(x_i) - y_i}{\Delta y_i} \right]^2 \tag{6.1}$$

At higher energies the LIS are described by power-laws. To be able to use the χ^2 test to compare the data to these calculated LIS, the model values had to be logarithmically interpolated to get values at energies corresponding to those of the data. The interpolation was done by using Equation (6.2) with x_i the energy value at which y_i is to be calculated. The two points between which the interpolation is done, are given by (x_1, y_1) and (x_2, y_2):

$$y_i = a x_i^b \tag{6.2}$$

$$\begin{aligned} \text{with} \qquad a &= \frac{y_1}{x_1^b} \\ b &= \frac{ln(y_1/y_2)}{ln(x_1/x_2)}. \end{aligned}$$

Solar modulation

The experimental data values also need to be adjusted to account for the modulation due to the solar cycle. It is an important factor to consider, as modulation has a large effect on the CR intensities at lower energies and the effect at the lowest energy considered in this study, 4 GeV/nuc,

is not negligible. A force field model with modulation parameter as described in Section 5.2 is implemented to include the effects of modulation. Modulation parameters for different periods in the solar cycle are estimated from comparing proton data, measured through out the solar cycle, to the proton LIS given by Langner (2004). By adjusting the modulation parameter, the experimental proton data are fitted to the proton LIS by Langner (2004). Thus, associating a modulation parameter for each data set, which is subsequently used with the remaining CR species in the data set. Each set of data from different experiments is demodulated (effect of the heliosphere removed) using a force field parameter estimated to roughly correspond to the period in the solar cycle when the data were measured. The force field parameters are listed in Table 6.4 and correspond to the data sets, obtained form the CR database (Strong, 2009), as listed in Appendix B.

After the interpolation and modulation have been implemented, the χ^2 values are calculated for the LIS of each CR species. The LIS of each model, described by an individual set of parameters in the parameter space given in Table 6.1, is compared to the corresponding demodulated data points for the CR species. The calculated χ^2 values were then added up separately according to the CR groups of Table 6.3. This results in three χ^2 values for each model in the parameter space, one for each CR component, given in Table 6.2, as a whole.

Table 6.4: Estimated force field parameters for the experimental data sets used

Data set	Reference	Parameter (MV)
AMS01	Aguilar et al. (2002)	680
ATIC2	Panov et al. (2007)	885
BESS	Sanuki et al. (2000)	750
CAPRICE98	Boezio et al. (2003)	950
CRN	Müller et al. (1991) and Swordy et al. (1993)	700
HEA03	Engelmann et al. (1990)	885
IMAX	Menn et al. (2000)	750
JACEE	Asakimori et al. (1998)	900
MUBEE	Zatsepin et al. (1994)	700
RUNJOB	Derbina et al. (2005)	885
SANKIRU	Kamioka et al. (1997)	700
SOKOL	Ivanenko et al. (1993)	700

6.4 Parameter study results

In this section the results of the parameter study are presented, the best fit values listed and compared to values obtained in studies by other authors.

6.4.1 Minimum χ^2 results

The resulting χ^2 values for the parameter space described in Section 6.2 were used to find the best fit model for each of the three CR component groups. This was done by finding a single model for each component that gives the minimum χ^2 value. These three best fitting models are presented in Table 6.5. The minimum χ^2 value for a fixed combination of two of the three parameters and varying the third, was also calculated. These minimum χ^2 values were plotted as contour plots in Figures 6.1 to 6.3. The best fit model values in Table 6.5 are marked on the contour graphs for comparison (a 4-point star for the primary component, a diamond for the secondary component and a square for the mixed component). Table 6.6 lists the total χ^2 obtained for the three best fit models (marked accordingly), but also includes the χ^2 values for all three components and the number of data points used. Table 6.7 similarly lists the reduced χ^2 values and the degrees of freedom[2].

Table 6.5: Best fit values obtained for the three components and the corresponding models

CR component group	K_0 ($10^{28}\,\mathrm{cm^2 s^{-1}}$)	α	δ	χ^2	# of data points	model #
Primary	2.86	2.66	0.10	2953.10	279	23105
Mixed	1.02	2.79	0.10	2005.60	115	09857
Secondary	1.92	2.21	0.77	182.31	47	17784

Table 6.6: Total χ^2 values for each model and the corresponding number of data points

CR component group	Primary model	Mixed model	Secondary model	# of data points
Primary	2953.10	20385.10	36362.40	279
Mixed	4488.60	2005.60	9329.04	115
Secondary	1584.26	7522.38	182.31	47

Table 6.7: Reduced χ^2 values for each model and the corresponding degrees of freedom

CR component group	Primary model	Mixed model	Secondary model	Degrees of freedom
Primary	10.74	74.13	132.23	275
Mixed	40.44	18.07	84.05	111
Secondary	36.84	174.94	4.24	43

As seen in the contour plots and Tables 6.5, 6.6 and 6.7, the parameter values for the best fit models differ between the three components. The χ^2 contours can also be seen to be quite different. The mutually exclusive best fit values and differing dependences on the parameters indicate that CR primaries and secondaries have different sensitivities to the model parameters and cannot be modelled simultaneously with the current model implementation.

In Figures 6.1 to 6.3, some of the contour lines are seen to be jagged. This is due to the relatively coarse grid chosen for the parameter study to decrease the computing time required.

[2]degrees of freedom = # of data points − # of parameters −1

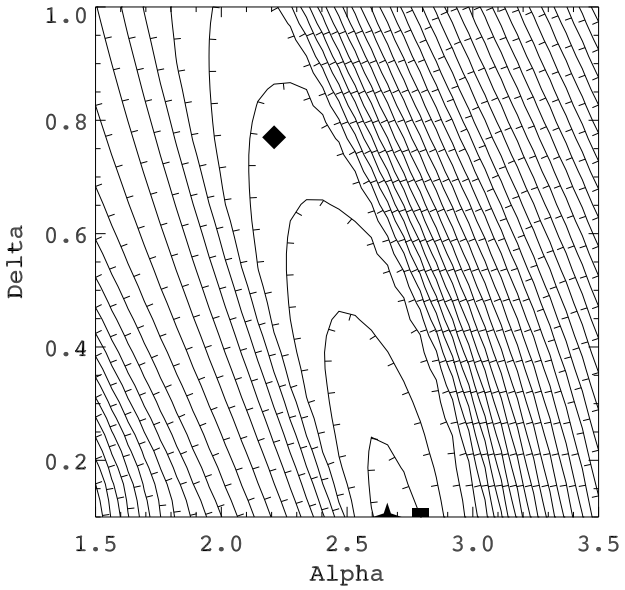

(a) χ^2 contours for variations in δ and α.

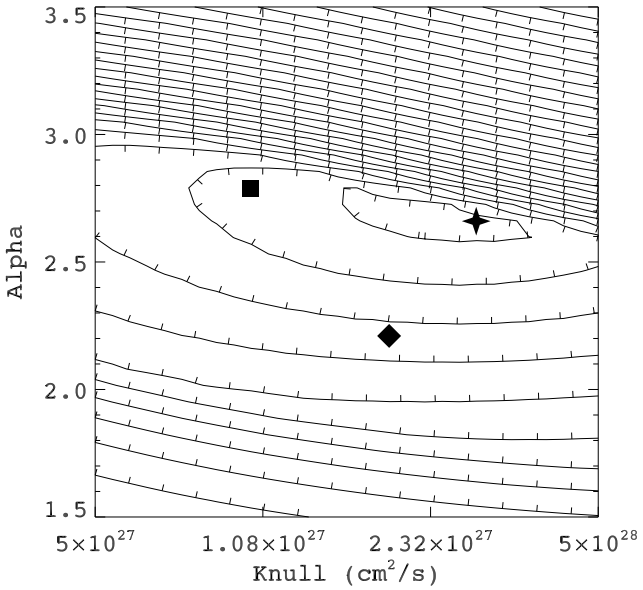

(b) χ^2 contours for variations in K_0 and α.

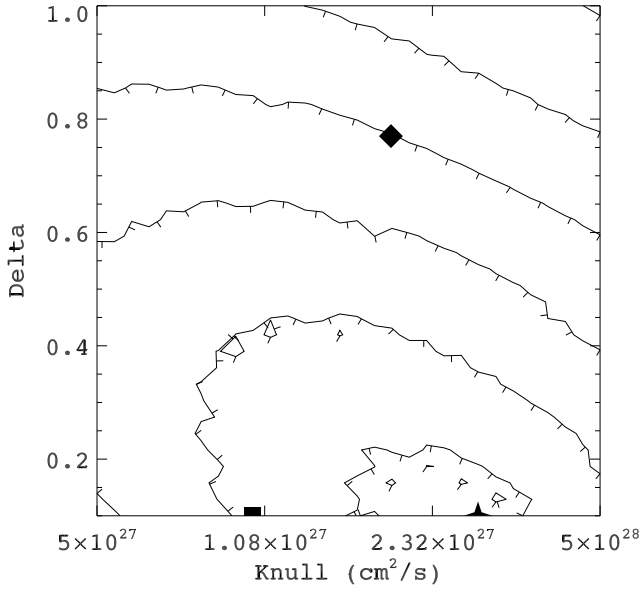

(c) χ^2 contours for variations in K_0 and δ.

Figure 6.1: χ^2 contours for parameter variations for the Primary CR component. Contours show the minimum χ^2 value of the third parameter for combinations of the two plotted parameters. The minimum value in each plane is marked as follows: a 4-point star for the primary component, a diamond for the secondary component and a square for the mixed component.

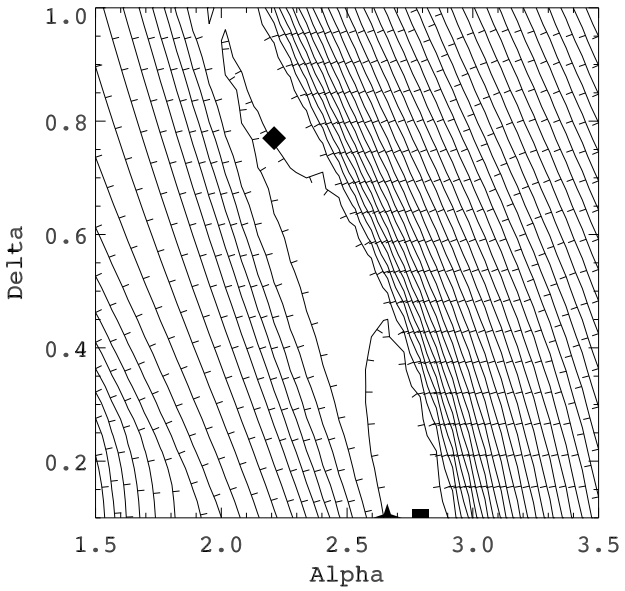

(a) χ^2 contours for variations in δ and α.

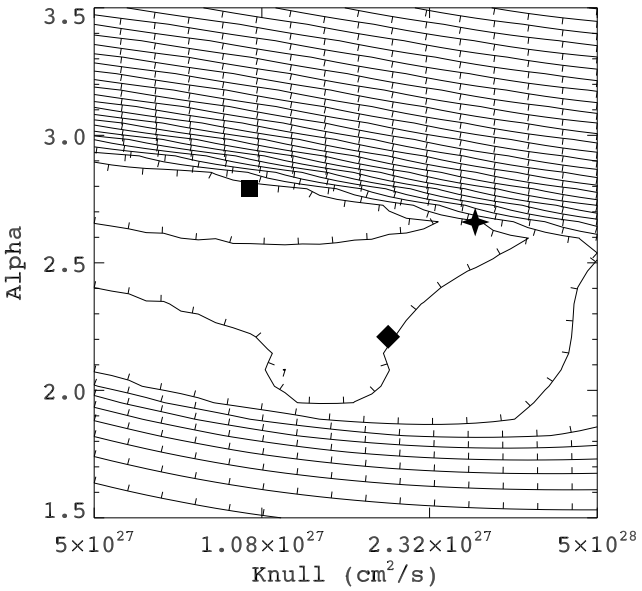

(b) χ^2 contours for variations in K_0 and α.

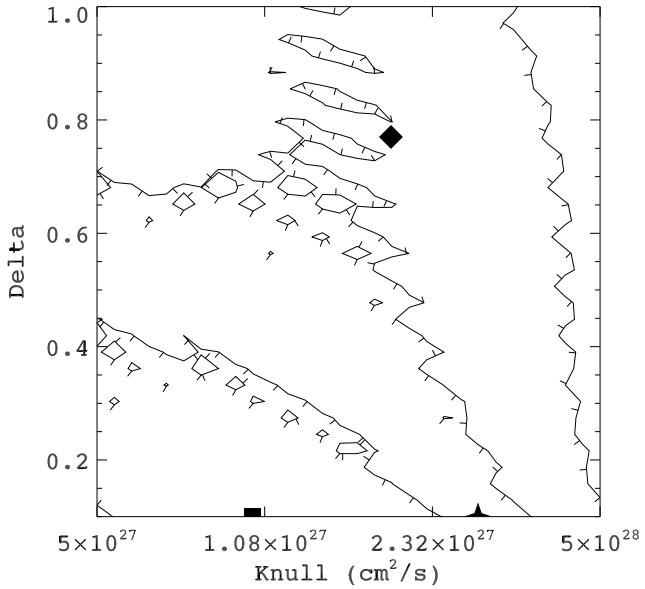

(c) χ^2 contours for variations in K_0 and δ.

Figure 6.2: Similar to Figure 6.1, but for the Mixed CR component.

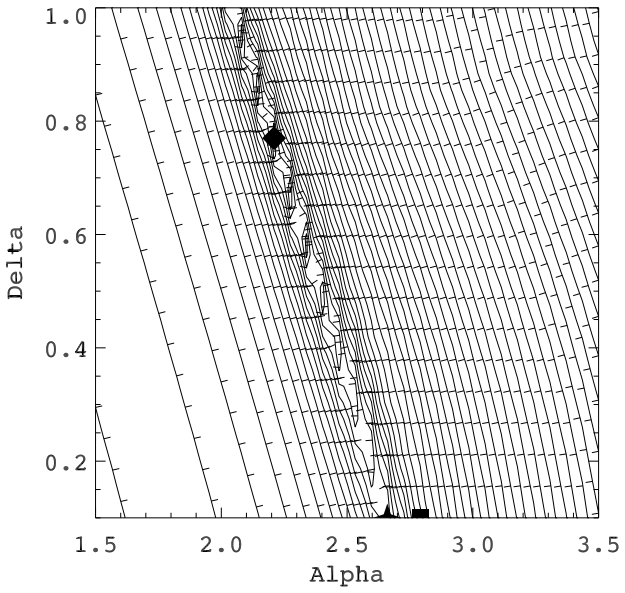

(a) χ^2 contours for variations in δ and α.

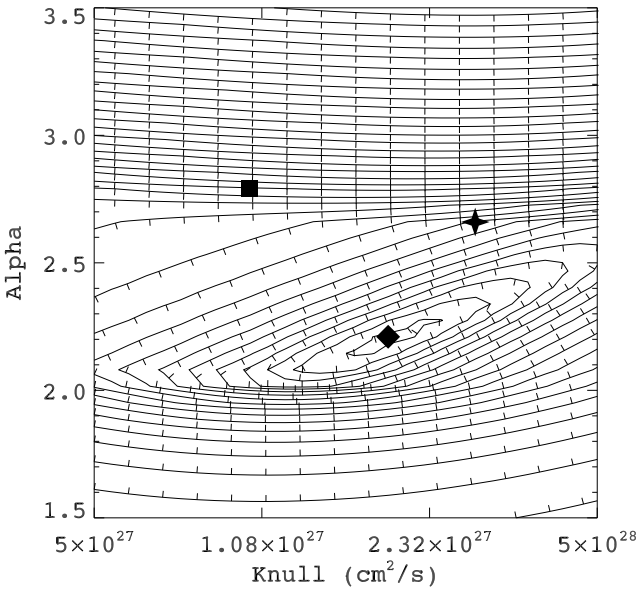

(b) χ^2 contours for variations in K_0 and α.

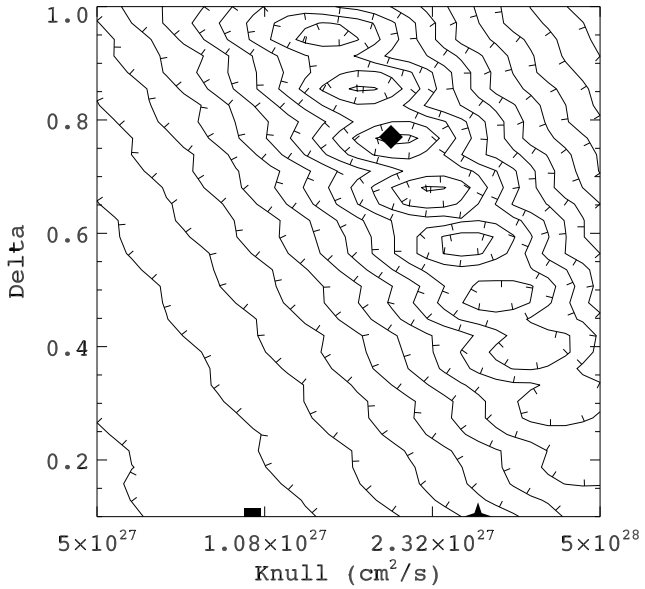

(c) χ^2 contours for variations in K_0 and δ.

Figure 6.3: Similar to Figure 6.1, but for the Secondary CR component.

The contour graphs of the secondaries and primaries show different features, but the mixed component shows features similar to both. This is expected since the mixed component includes both secondary and primary CRs. The relation between the three parameters can also be seen in the contour graphs. As examples, α and δ show an additive relation for all three components, K_0 and δ also show an additive relation for the secondary component. The high χ^2 values for models with α not in the range $2.0 < \alpha < 3.0$ indicate that values outside this range can be disregarded. For secondaries this range is smaller at about $2.0 < \alpha < 2.7$.

Taking only the χ^2 value as a measure for the fit of the model LIS to the experimental data, the secondary CRs are more easily fitted than the primaries or the mixed component group. This implies that the 2D plain diffusion model used is more suited to modelling secondary CRs than primary CRs.

6.4.2 Best fit LIS

The LIS produced by the best fit models with parameters listed in Table 6.5, are plotted in Figures 6.4 to 6.6. These figures show the LIS for selected CR species of the three component groups. The LIS for Carbon, Oxygen, Helium and Iron are shown for the primaries; Nitrogen, Sodium, Neon and Aluminium for the mixed group; and Boron, Phosphorus, Fluorine and Manganese for the secondaries. The experimental data and the corresponding demodulated data above 4 GeV used to calculate the χ^2 values as described in Section 6.3, are also shown.

The LIS for the four CR species in the Primary group shown in Figure 6.4 lie within the trend displayed by the data. The Helium and Iron LIS lie in the lower part of the trend. The LIS for the species in the Mixed group do not fit the data well. The Nitrogen and Sodium LIS fit at lower energies, but at energies above 10 GeV the LIS overshoot the data. The Neon LIS deviates at lower energies and the Aluminium LIS shows a poor fit to the data. The LIS for the Secondary group show good fits for all but the Manganese LIS.

Small deviations in the fit of any one CR species in a group are to be expected due to the fact that all the CR species in a component group were simultaneously fitted to the data. The individual fitting of a CR species may thus be lower or higher than expected to fit the data points, but for the group as a whole, a well defined minimum χ^2 value is still found. The fact that fitting each species at the same time is not always possible, points to either inconsistencies in the data or to an inadequate model.

Further, some data points of a given CR species are inconsistent between different experiments for CR species due to systematic errors; this can especially be seen for the primary component data. This results in a wider spread of data points and thus larger χ^2 values for species such as Iron and Helium, even though the LIS can be seen to lie within the trend displayed by the data.

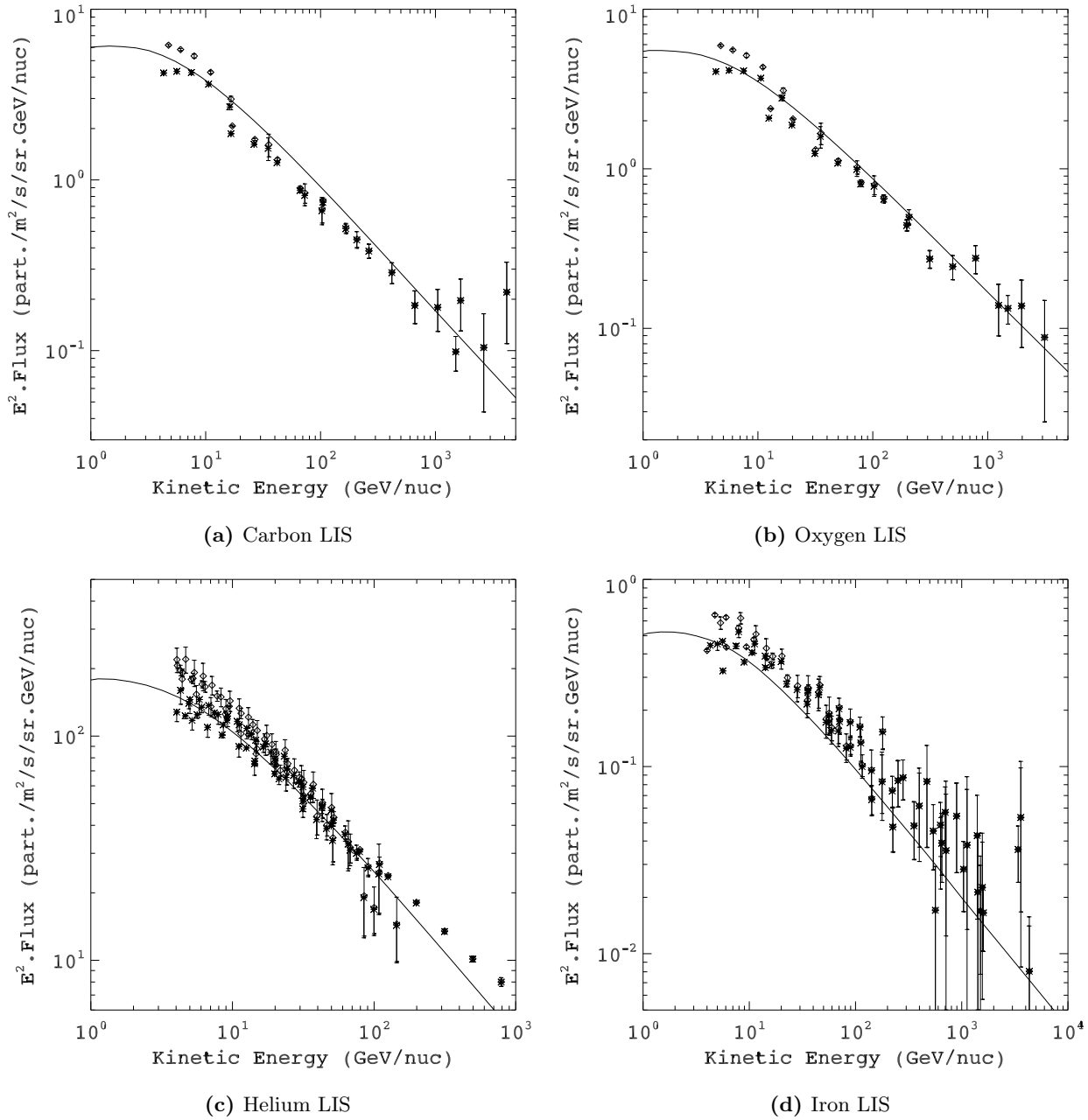

(a) Carbon LIS

(b) Oxygen LIS

(c) Helium LIS

(d) Iron LIS

Figure 6.4: LIS for the Primary CR component compared to experimental data (∗) and the demodulated experimental data (◇) used to calculate the χ^2 using only data points above 4 GeV. The LIS (solid curve) for Carbon, Oxygen, Helium and Iron are shown.

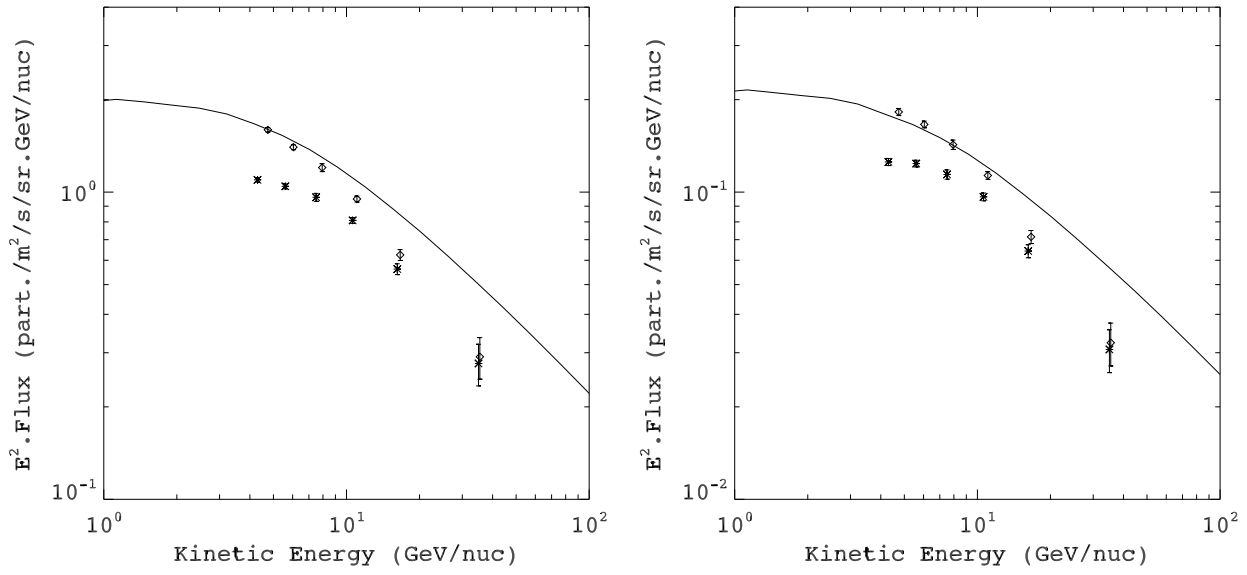

(a) Nitrogen LIS

(b) Sodium LIS

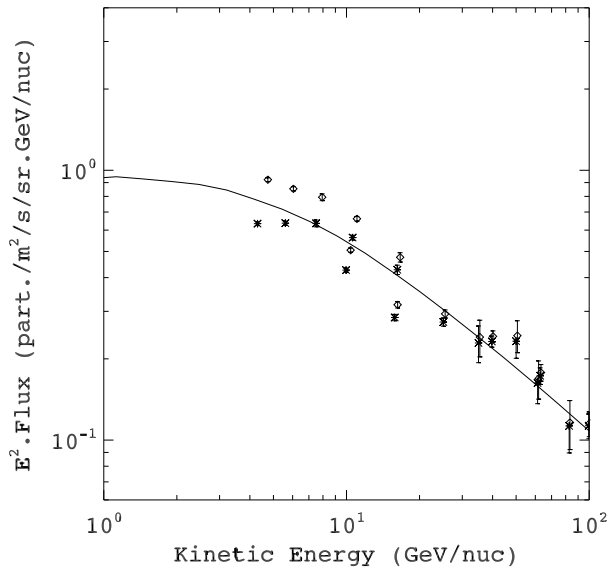

(c) Neon LIS

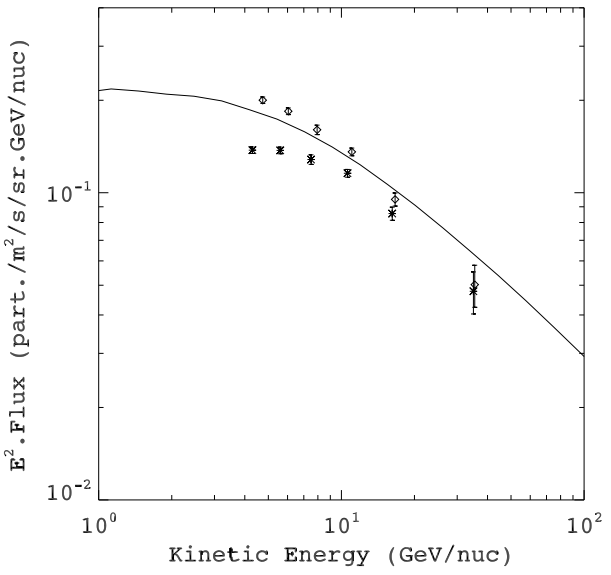

(d) Aluminium LIS

Figure 6.5: Similar to Figure 6.4, but showing the Mixed CR component LIS: Nitrogen, Sodium, Neon and Aluminium.

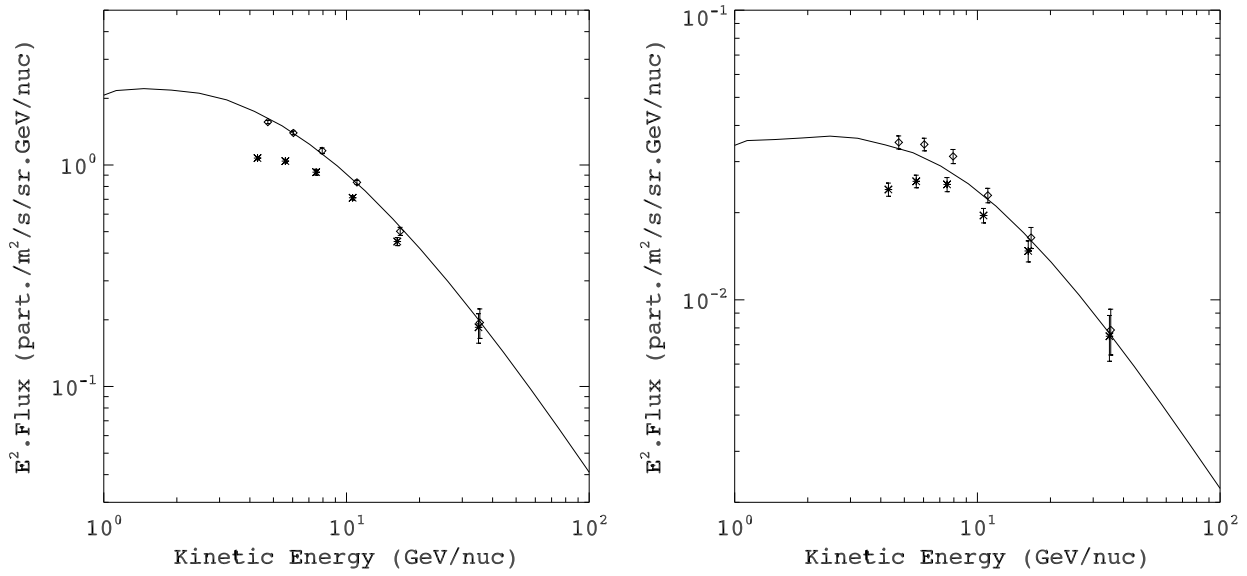

(a) Boron LIS

(b) Phosphorus LIS

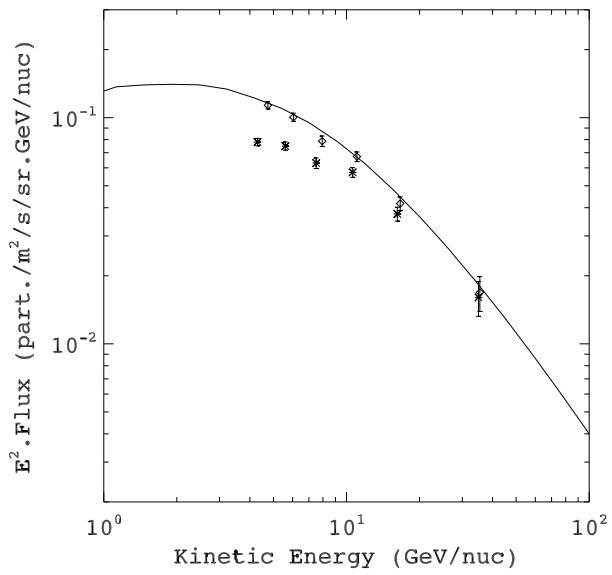

(c) Fluorine LIS

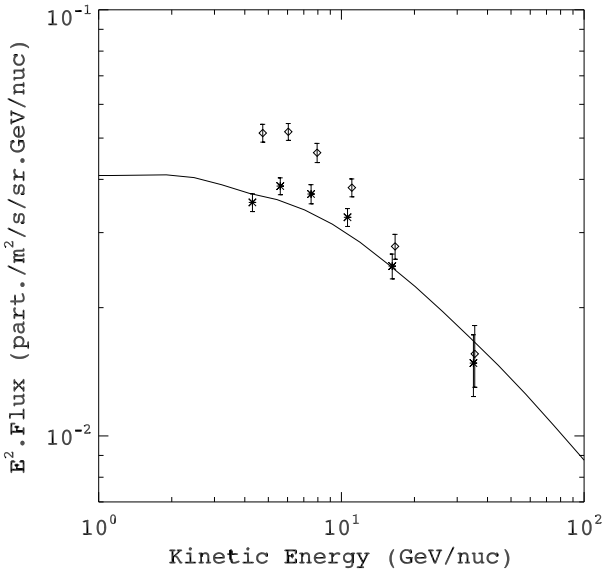

(d) Manganese LIS

Figure 6.6: Similar to Figure 6.4, but showing the Secondary CR component LIS: Boron, Phosphorus, Fluorine and Manganese.

This mutual exclusion of some experimental data points is accepted in this study, as we wanted to include as many different sets of data as possible and ranking of the different experiments is beyond the scope of this study. Different experiments are not always consistent in measuring the same LIS and that makes fitting the LIS difficult for more than one data set at a time using the χ^2 test.

The χ^2 value for the Mixed group is also large, but does not have the same problem of a large data set influencing the χ^2 values as the Primary group. The difficulty in fitting the Mixed group thus does not necessarily stem from mutually excluding data points.

Choosing a data set from a single reliable CR experiment to compare with the LIS would be the recommended next step for a similar parameter study.

6.4.3 Comparison with results from other authors

Table 6.8 lists the values that differ between the best fit models found in Section 6.4.1 and the parameter values used in the plain diffusion model by Ptuskin et al. (2006), using the GALPROP code, as contained in the Galdef file presented in Appendix A. The K_0 values are all at the reference rigidity of 4 GV. The δ value for the Ptuskin model is above the break (at 3 GV) in their model. The values of α for the Ptuskin model are for below and above the reference rigidity of 40 GV, respectively. In this study, no break was included in the source spectrum index.

Table 6.8: Best fit parameters compared to values obtained by Ptuskin et al. (2006)

Parameter	Ptuskin	Primary	Mixed	Secondary	Units
K_0	2.61	2.86	1.02	1.92	$10^{28}\,\mathrm{cm^2 s^{-1}}$
α	2.15 and 2.30	2.66	2.79	2.21	
δ	0.6	0.10	0.10	0.77	

All the Ptuskin et al. (2006) LIS presented in Figures 6.7 and 6.8 are much lower than those obtained in this study at energies below 10 GeV. Except for the Sodium and Nitrogen LIS, the Ptuskin et al. (2006) LIS do correspond to the obtained LIS at higher energies. These differences can possibly be attributed to the dependence of the fitting to the data sets. Using different data sets or excluding data from certain experiments will have a meaningful effect on finding the best fit LIS. Also, the method of including modulation is important, as choosing a modulation parameter for the force field model can be done arbitrarily.

Table 6.9: Best fit α and δ values compared to those obtained by Maurin et al. (2002) and Putze et al. (2009, 2010)

Parameter	Maurin 2002	Putze 2009	Putze 2010	Primary	Mixed	Secondary
α	> 2.0	2.14 - 2.17	—	2.66	2.79	2.21
δ	< 0.6 - 0.7	0.55 - 0.6	0.65	0.10	0.10	0.77

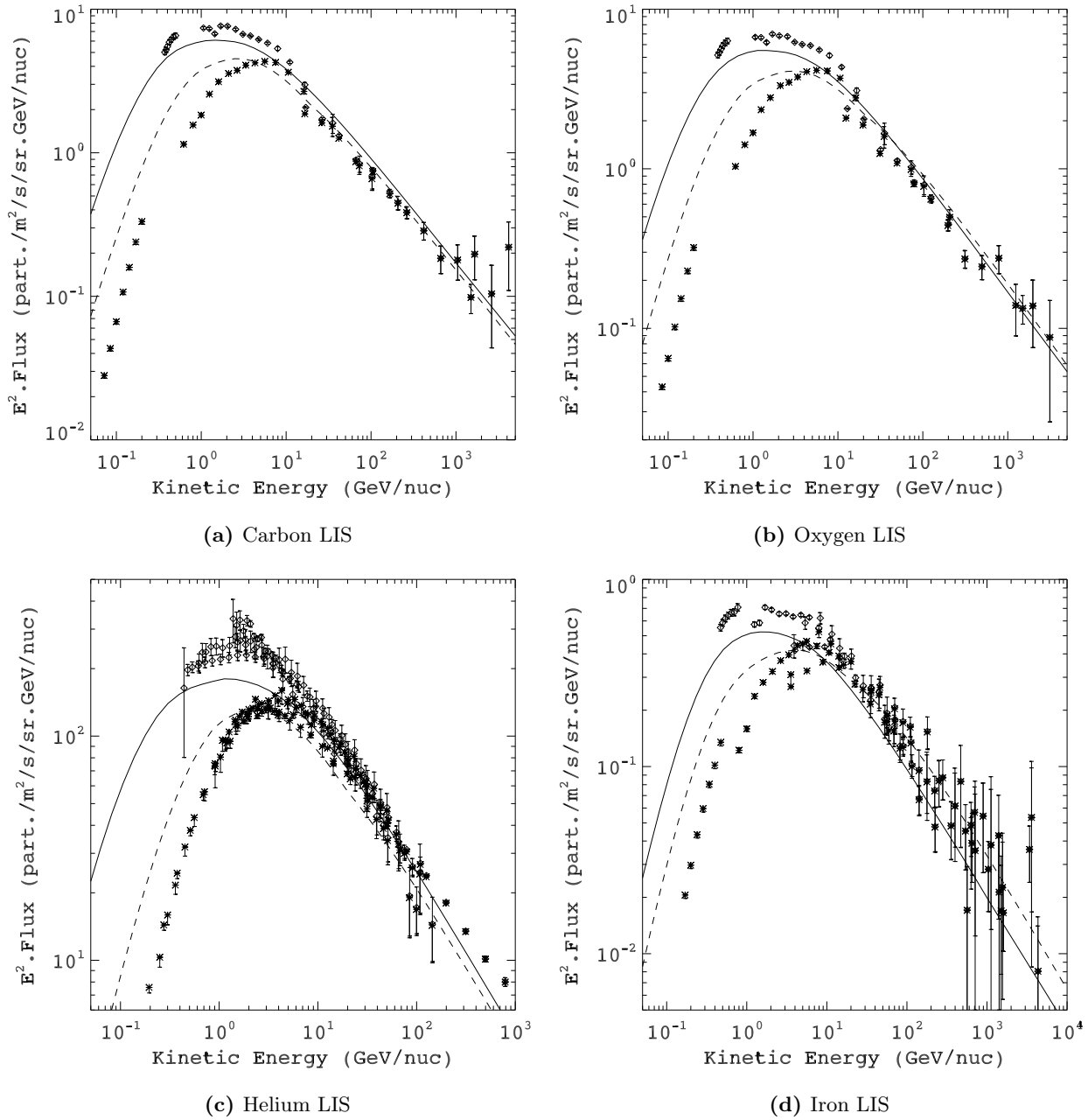

(a) Carbon LIS

(b) Oxygen LIS

(c) Helium LIS

(d) Iron LIS

Figure 6.7: LIS for the Primary CR component compared to experimental data (∗) and the demodulated experimental data used to calculate the χ^2 (◇). The LIS for Carbon, Oxygen, Helium and Iron are shown (solid curve), as well as the corresponding LIS calculated by Ptuskin et al. (2006) (dashed curve).

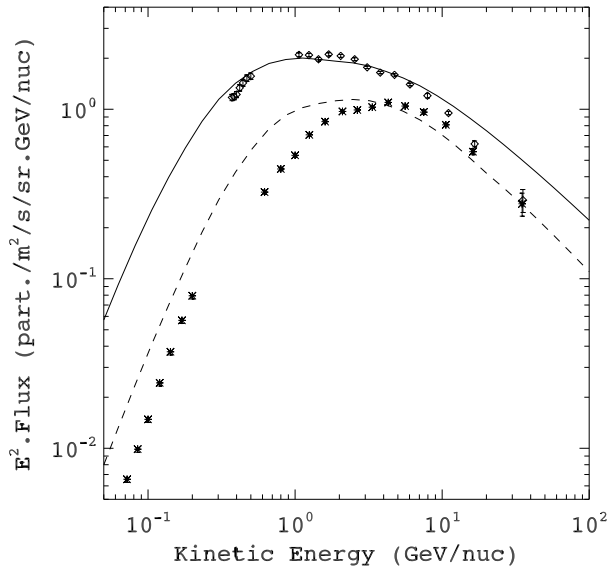

(a) Nitrogen LIS

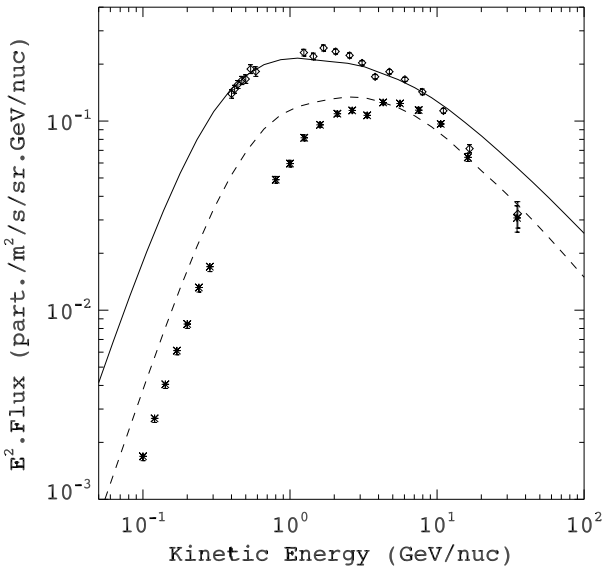

(b) Sodium LIS

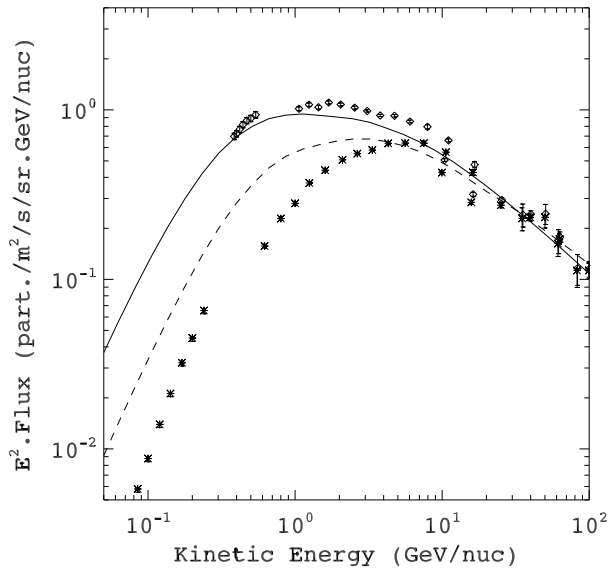

(c) Neon LIS

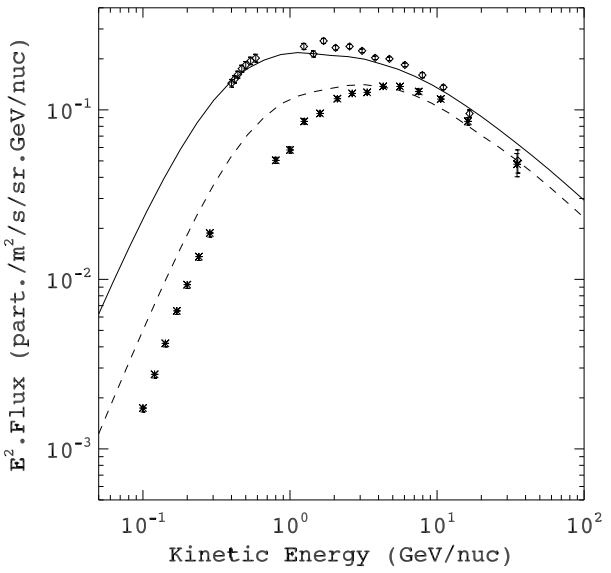

(d) Aluminium LIS

Figure 6.8: Similar to Figure 6.7, but for the Mixed CR component LIS: Nitrogen, Sodium, Neon and Aluminium.

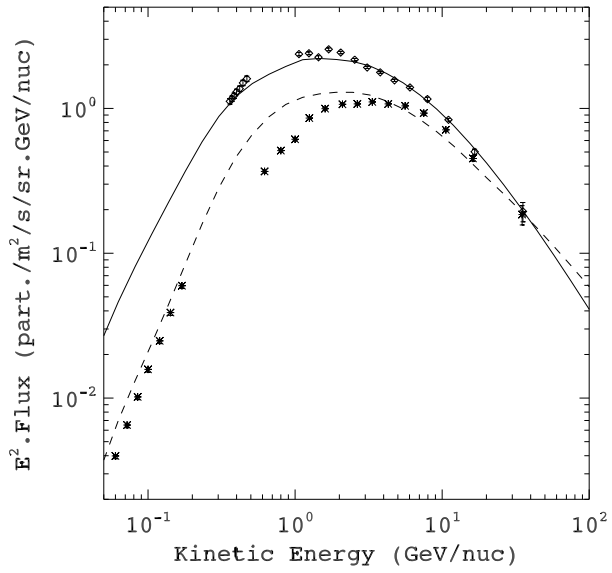

(a) Boron LIS

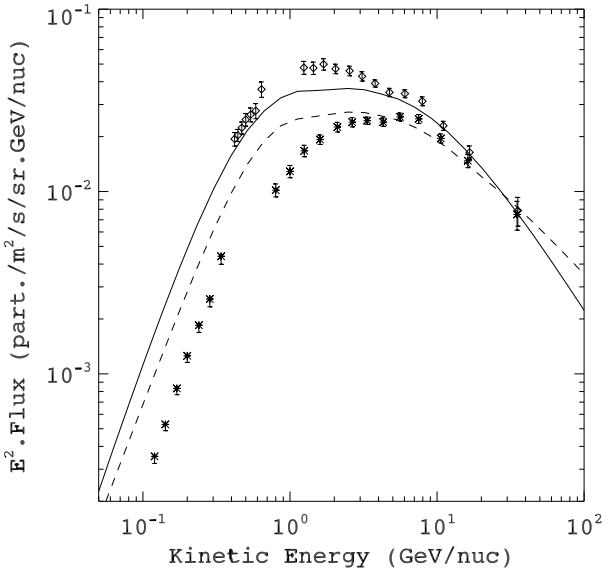

(b) Phosphorus LIS

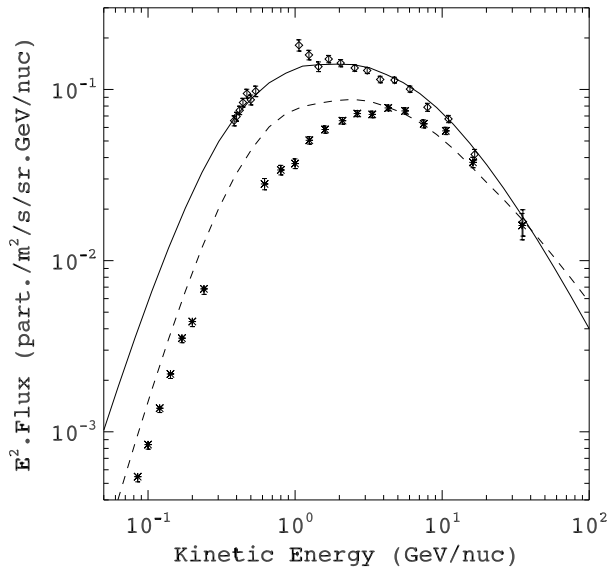

(c) Fluorine LIS

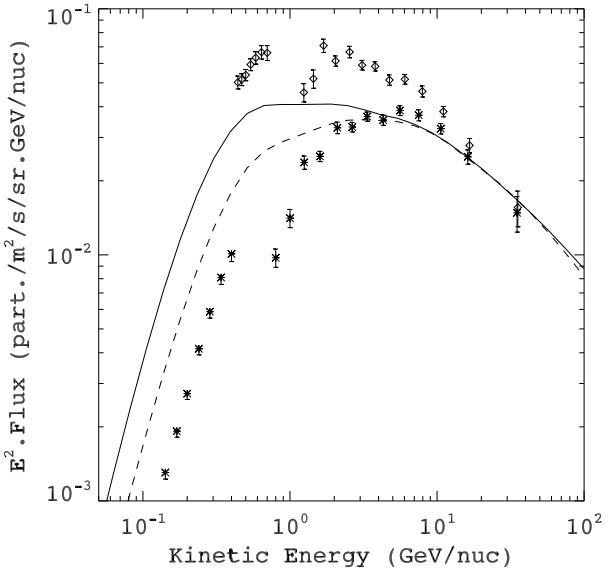

(d) Manganese LIS

Figure 6.9: Similar to Figure 6.7, but for the Secondary CR component LIS: Boron, Phosphorus, Fluorine and Manganese.

A comparison of α and δ values to values obtained in studies conducted by Maurin et al. (2002) and Putze et al. (2009, 2010) is shown in Table 6.9. Maurin et al. (2002) studied the relation $\alpha + \delta = 2.8$ with a 2D diffusive propagation code similar to GALPROP and found the preferred values for α to be > 2.0 and for δ to be < 0.6 - 0.7. Putze et al. (2009) used a Monte Carlo technique with a Leaky-Box model and by keeping the relation $\alpha + \delta = 2.65$ fixed found that α should have a value of about 2.14 to 2.17 and δ a value of about 0.55 to 0.6. The follow up study by Putze et al. (2010) found a value of $\delta = 0.65$ with $\alpha+\delta = 2.65$ fixed for a plain diffusion model.

The α and δ values found for the Secondary component compare favourably with those found by Maurin et al. (2002) and Putze et al. (2009, 2010). The values for the Primary and Mixed components deviate more, with α larger than those found in the other studies, and δ significantly smaller. This again suggests the model being better suited for secondaries.

6.5 Summary and conclusions

Primary and secondary CR species are produced by different physical processes in the Galaxy. Primary CRs are most probably accelerated at SNRs, transient point-like sources, so that 2D modelling might be limited in its capability to handle primary CRs adequately, but it has been shown that the 2D model sufficiently describes CR secondaries. The main goal of this study is to compare the LIS obtained from the 2D GALPROP code with experimental data, for the primary and for secondary CR species, respectively. To accomplish this goal a parameter study was conducted by varying three of the parameters in the 2D plain diffusion model by Ptuskin et al. (2006). The set of free parameters adjusted in the model for this study are the source spectral index (α), the spectral index of the diffusion coefficient (δ) and the magnitude of the diffusion coefficient at particle rigidity 4 GV (K_0).

The LIS produced by the models as described in Section 6.2, are compared to experimental CR data. The data sets used in this study were taken from the 11 Nov 2009 version of the CR database maintained by Strong (2009). The individual CR species were divided up into three groups according to the fraction of secondary and primary nuclei in each. The modelled LIS of the CR species in the three components were then compared to the experimental data using a χ^2 test. The parameter values found for the best fit models, differ between the Primary, Mixed and Secondary CR component groups. The χ^2 contours are also quite different, showing that the dependence of the χ^2 value on the three parameters, differs for the three components.

The Ptuskin et al. (2006) LIS were seen to be much lower at larger energies than those obtained in this study. Certain LIS do correspond to the Ptuskin et al. LIS at higher energies. Comparison of α and δ values found with those reported by Maurin et al. (2002) and Putze et al. (2009, 2010) showed that the Secondary component values are closer to those of the other studies than the Primary and Mixed component values.

The secondary CRs were found to be more easily fitted than the primaries or the mixed component group. This implies that the model used is better suited to secondaries than primaries.

Chapter 7

Summary and Conclusions

The main objective of this study was to look for evidence of nearby CR point sources in the observed CR chemical composition. To accomplish this, the 3D implementation of the GALPROP code was investigated. This led to the discovery of problems in the numerical scheme of the 3D code, so it could not be used further. So only the 2D implementation of the GALPROP code was available and was used instead. By means of 3D time-dependent calculations, Büsching et al. (2005) showed that a 2D model was sufficient to describe the secondary component of galactic CRs, but failed to describe the local CR primary flux if nearby point sources are present. Taking advantage of this fact and looking at CR primaries and secondaries separately, evidence of nearby CR point sources might be found with the 2D code. The 2D code, a rotational symmetric model in cylindrical coordinates, assumes sources distributed evenly over the whole Galaxy in the angular direction, which do not necessarily result in the same local CR flux as the one produced by real local point-sources. Therefore, if there are nearby point-like sources, the 2D code will not be adequate to describe the CR primary component originating from these sources. In this case, working with secondary, tertiary, or higher CR nuclei may thus yield a better description of galactic CR propagation than primary CR nuclei. Conducting a parameter study, this should be seen in the different best fit values for CR primaries and secondaries, as the flux of the secondary (and higher) CR component does not depend on the local source history (Büsching et al., 2005).

First, the 3D implementation of the GALPROP code was tested with the aim of using this code to study local CR point sources. Unfortunately, the present version (v.50.1p) of the publicly available 3D code was found to be insufficient, due to the non-spherical spread of the CR density from a single point source. Thus, for this study, only the 2D implementation of GALPROP was available, as mentioned above.

To test and verify the 2D GALPROP code, but also to ensure its correct implementation, the results by Ptuskin et al. (2006) were successfully reproduced.Thus, it can be concluded that the code was implemented correctly and could be used further in this study. The numerical

stability of the GALPROP code was tested next, by decreasing the grid sizes in the z-axis and the r-axis, respectively. The variations due to the smaller grid sizes were found to be negligible and also did not improve the accuracy of the model.

To be able to fit LIS to experimental data at Earth, heliospheric modulation has to be taken into account. For this purpose, initial attempts were made to add a 2D drift model to the GALPROP code, but because of compatibility issues (matching the Fortran code of the heliospheric drift model to the C++ code of GALRPOP), the difficulty of making the more complex drift model user-friendly and the high numerical costs, the effort took much longer than anticipated. The force field approximation was chosen instead for this study, as the approximation is valid at Earth and the observations used in this study have been taken only from Earth orbiting satellites and balloon experiments. Only CR nuclei were studied and time-dependence was not considered, thus the disadvantages of the force field were largely avoided. Testing of the force field approximation showed that it agrees favourably with the output of the 2D drift code for the application in this study. In addition, the force field approximation had already been implemented by Strong and Moskalenko (2001) and packaged alongside the GALPROP code.

A parameter study was conducted to obtain best fit values separately for CR primaries and secondaries. This was done by using the GALPROP code to model CR propagation through the Galaxy. Three of the parameters in the 2D plain diffusion model used by Ptuskin et al. (2006) were varied: the source spectral index (α), the spectral index of the diffusion coefficient (δ) and the magnitude of the diffusion coefficient at a particle rigidity of 4 GV (K_0). The LIS produced by the models were compared to experimental CR data taken from the 11 Nov. 2009 version of the CR database maintained by Strong (2009) by means of a χ^2 test. Each set of data from different experiments was demodulated using the force field parameter estimated to roughly correspond to the period in the solar cycle when the data were measured. The individual CR datapoints were then divided up into three component groups, according to the fraction of primary and secondary nuclei in each species. The LIS of the three components, the Primary, Secondary and Mixed components, were fitted separately to the data.

When comparing the best fit models found for each CR component group, the parameter values for these best fit models are seen to differ between the Primary, Mixed and Secondary CR component groups. The χ^2 contours are also quite different, showing that the dependence of the χ^2 value on the three parameters differs between the three components. The best fit value for a given group also has a rather large χ^2 value when using the best fit parameters of another group. These larger χ^2 values indicate that the best fit models are statistically exclusive.

Comparing the best fit LIS found in the parameter study to the Ptuskin et al. (2006) LIS, their LIS are seen to be much lower at larger energies than those obtained in this study, but certain LIS do agree favourably at higher energies. A comparison of α and δ values found with those

reported by Maurin et al. (2002) and Putze et al. (2009, 2010), shows the Secondary component values to be closer to those of other studies than the Primary and Mixed component values.

The secondary CRs were found to be more easily fitted to data than the Primary component or the Mixed component group. This implies that the 2D GALPROP model as used is indeed better suited for secondaries than for primaries. Thus, when only comparing CR data to LIS of secondary CRs the model can be used successfully. The results, together with the manner in which the 2D model handles CR sources, imply that there may be local sources of CRs that, so far, are not being taken into account. Such a local source necessitates the use of more involved models, capable of taking point-like sources into account, than the one used in this study.

The difference between fitting the Secondary component and the Primary component may also be due to the wider spread of data points and thus larger χ^2 values, especially for the primary CR species. This difference between data sets of various experiments measuring the same LIS, makes fitting the LIS difficult for more than one data set at a time. The χ^2 value for the Mixed group is large as well, but does not have the same problem with the data sets as the Primary group. The difficulty in fitting the Mixed group does not necessarily stem from the data used. This study cannot distinguish between the two possibilities and neither can be ruled out. A follow-up study where a data set from a single reliable CR experiment is chosen, would help to answer this problem.

Suggested further studies are:

- Choosing a single, but reliable experimental data set, such as that of the PAMELA experiment, is recommended instead of a large data compilation.
- A drift approach to heliospheric modulation is beyond the scope of this study due to the complexity of adding it to the GALPROP code. It is highly recommended that for any future studies which include data or models for protons, anti-protons, electrons, positrons or CRs at lower energies, that at least the 2D drift approach is followed.
- The 3D version of the GALPROP code is recommended once the shortcomings found here are addressed.
- A larger parameter space for the parameter study is possible, as this study was only limited to the three most important parameters.

The results of this study were presented at:

- The 2010 COSPAR conference
- The 2011 ICRC conference and published in the proceedings (Bisschoff et al., 2011a)
- The 2011 SAIP conference and published in the proceedings (Bisschoff et al., 2011b)

Appendix A

The Galdef file

In this Appendix the Galdef file 999726, given by Ptuskin et al. (2006), is presented verbatim. The Galdef file is the main input file in the GALPROP code for specifying the adjustable parameters for a single model run. The purpose of each parameter or parameter set is discussed by Strong and Moskalenko (2006) and presented in Section 3.5.

Galdef 999726

```
1  123456789012345678901
2  ======================value
3  Title                = conventional/2D 4 kpc tuned to agree with ACE
4  Title                = source isotopic distr. of an element = solar isot. abund. distr.
5  n_spatial_dimensions = 2
6  r_min                =00.0    min r
7  r_max                =20.00   max r
8  dr                   = 1.0    delta r
9  z_min                =-4.0    min z
10 z_max                =+4.0    max z
11 dz                   = 0.1    delta z
12
13 x_min                =  0.0   min x
14 x_max                =+15.0   max x
15 dx                   =  0.2   delta x
16 y_min                =  0.0   min y
17 y_max                =+15.0   max y
18 dy                   =  0.2   delta y
19
20 p_min                =1000   min momentum (MV)
21 p_max                =4000   max momentum
22 p_factor             =1.50       momentum factor
23
24 Ekin_min             =1.0e1  min kinetic energy per nucleon (MeV)
25 Ekin_max             =1.0e7  max kinetic energy per nucleon
26 Ekin_factor          =1.3        kinetic energy per nucleon factor
27
28 p_Ekin_grid          = Ekin         p||Ekin alignment
29
30 E_gamma_min          = 1.e0   min gamma-ray energy (MeV)
31 E_gamma_max          = 1.e8   max gamma-ray energy (MeV)
32 E_gamma_factor       = 1.4    gamma-ray energy factor
33 integration_mode     = 1      integr.over part.spec.: =1-old E*logE; 0=1-PL analyt.
34
35 nu_synch_min         = 1.0e6   min synchrotron frequency (Hz)
```

```
nu_synch_max         = 1.0e10  max synchrotron frequency (Hz)
nu_synch_factor      = 2.0         synchrotron frequency factor

long_min             =  0.50   gamma-ray intensity skymap longitude minimum (deg)
long_max             =359.50   gamma-ray intensity skymap longitude maximum (deg)
lat_min              =-89.50   gamma-ray intensity skymap latitude  minimum (deg)
lat_max              =+89.50   gamma-ray intensity skymap latitude  maximum (deg)
d_long               =  1.00   gamma-ray intensity skymap longitude binsize (deg)
d_lat                =  1.00   gamma-ray intensity skymap latitude  binsize (deg)

D0_xx                =2.2e+28          diffusion coefficient at reference rigidity
D_rigid_br           =3.0e3            reference rigidity for diffusion coefficient in MV
D_g_1                = 0.000000e+00    diffusion coefficient index below reference rigidity
D_g_2                = 6.000000e-01    diffusion coefficient index above reference rigidity
diff_reacc           = 0   0=no reacc; 1,2=diff.reacc; -1=beta^3 Dxx; 11=Kolmogorov+damping; 12=Kraichnan+damping
v_Alfven             = 0.0             Alfven speed in km s-1

damping_p0           = 1.e6    MV -some rigidity (where CR density is low)
damping_const_G      = 0.02    a const derived from fitting B/C
damping_max_path_L   = 3.e21   Lmax~1 kpc, max free path

convection           =0        1=include convection
v0_conv              =0.       km s-1        v_conv=v0_conv+dvdz_conv*dz
dvdz_conv            =3.       km s-1 kpc-1  v_conv=v0_conv+dvdz_conv*dz

nuc_rigid_br         =4.0e4    reference rigidity for nucleus injection index in MV
nuc_g_1              =2.30     nucleus injection index below reference rigidity
nuc_g_2              =2.15     nucleus injection index index above reference rigidity

inj_spectrum_type    = rigidity     rigidity||beta_rig||Etot nucleon injection spectrum type

electron_g_0         =2.40     electron injection index below electron_rigid_br0
electron_rigid_br0   =4.0e3    reference rigidity0 for electron injection index in MV
electron_g_1         =2.40     electron injection index below reference rigidity
electron_rigid_br    =1.0e3    reference rigidity for electron injection index in MV
electron_g_2         =2.4      electron injection index index above reference rigidity

He_H_ratio           =0.11     He/H of ISM, by number
X_CO                 =0.4E20,0.4E20,0.6E20,0.8E20,1.5E20,10.0E20,10.0E20,10.0E20,10.0E20 conversion factor from CO
  integrated temperature to H2 column density for CO rings  0.0; 1.5; 3.5; 5.5; 7.5; 9.5; 11.5; 13.5; 15.5; 50 kpc
fragmentation        =1        1=include fragmentation
momentum_losses      =1        1=include momentum losses
radioactive_decay    =1        1=include radioactive decay
K_capture            =1        1=include K-capture

start_timestep       =1.0e7
end_timestep         =1.0e2
timestep_factor      =0.25
timestep_repeat      =20     number of repeats per timestep in  timetep_mode=1
timestep_repeat2     =0      number of timesteps in timetep_mode=2
timestep_print       =10000  number of timesteps between printings
timestep_diagnostics =10000  number of timesteps between diagnostics
control_diagnostics  =0      control detail of diagnostics

network_iterations   = 2     number of iterations of entire network

prop_r               = 1  1=propagate in r (2D)
prop_x               = 1  1=propagate in x (2D,3D)
prop_y               = 1  1=propagate in y (3D)
prop_z               = 1  1=propagate in z (3D)
prop_p               = 1  1=propagate in momentum

use_symmetry         = 0  0=no symmetry, 1=optimized symmetry, 2=xyz symmetry by copying(3D)

vectorized           = 0  0=unvectorized code, 1=vectorized code

source_specification = 0     2D::1:r,z=0 2:z=0  3D::1:x,y,z=0 2:z=0 3:x=0 4:y=0
source_model         = 1     0=zero 1=parameterized  2=Case&B 3=pulsars 4= 5=S&Mattox 6=S&Mattox with cutoff
source_parameters_1  = 0.5   model 1:alpha
source_parameters_2  = 1.0   model 1:beta
```

```
source_parameters_3  = 20.0  model 1:rmax


n_cr_sources         = 0     number of pointlike cosmic-ray sources   3D only!
cr_source_x_01       = 10.0  x position of cosmic-ray source 1 (kpc)
cr_source_y_01       = 10.0  y position of cosmic-ray source 1
cr_source_z_01       = 0.1   z position of cosmic-ray source 1
cr_source_w_01       = 0.1  sigma width of cosmic-ray source 1
cr_source_L_01       = 1.0   luminosity of cosmic-ray source 1
cr_source_x_02       = 3.0   x position of cosmic-ray source 2
cr_source_y_02       = 4.0   y position of cosmic-ray source 2
cr_source_z_02       = 0.2   z position of cosmic-ray source 2
cr_source_w_02       = 2.4  sigma width of cosmic-ray source 2
cr_source_L_02       = 2.0   luminosity of cosmic-ray source 2


SNR_events           = 0         handle stochastic SNR events
SNR_interval         = 1.0e4     time interval in years between SNR in 1 kpc^-3 volume
SNR_livetime         = 1.0e4     CR-producing live-time in years of an SNR
SNR_electron_sdg     = 0.00      delta electron source index Gaussian sigma
SNR_nuc_sdg          = 0.00      delta nucleus  source index Gaussian sigma
SNR_electron_dgpivot = 5.0e3     delta electron source index pivot rigidity (MeV)
SNR_nuc_dgpivot      = 5.0e3     delta nucleus  source index pivot rigidity (MeV)

HI_survey            = 9         HI survey 8=orig 8 rings  9=new 9 rings
CO_survey            = 9         CO survey 8=orig 8 rings  9=new 9 rings

B_field_model        = 050100020           bbbrrrzzz    bbb=10*B(0)  rrr=10*rscale zzz=10*zscale
ISRF_file            = MilkyWay_DR0.5_DZ0.1_DPHI10_RMAX20_ZMAX5_galprop_format.fits          input ISRF file
ISRF_factors         = 1.0,1.0,1.0         ISRF factors for IC calculation: optical, FIR, CMB

proton_norm_Ekin     = 1.00e+5 proton kinetic energy for normalisation (MeV)
proton_norm_flux     = 4.90e-9 to renorm nuclei/flux of protons at norm energy (cm^-2 sr^-1 s^-1 MeV^-1)

electron_norm_Ekin   = 34.5e3  electron kinetic energy for normalisation (MeV)
electron_norm_flux   = .40e-9  flux of electrons at normalisation energy (cm^-2 sr^-1 s^-1 MeV^-1)

max_Z                = 28      maximum number of nucleus Z listed
use_Z_1              = 1
use_Z_2              = 1
use_Z_3              = 1
use_Z_4              = 1
use_Z_5              = 1
use_Z_6              = 1
use_Z_7              = 1
use_Z_8              = 1
use_Z_9              = 1
use_Z_10             = 1
use_Z_11             = 1
use_Z_12             = 1
use_Z_13             = 1
use_Z_14             = 1
use_Z_15             = 1
use_Z_16             = 1
use_Z_17             = 1
use_Z_18             = 1
use_Z_19             = 1
use_Z_20             = 1
use_Z_21             = 1
use_Z_22             = 1
use_Z_23             = 1
use_Z_24             = 1
use_Z_25             = 1
use_Z_26             = 1
use_Z_27             = 1
use_Z_28             = 1
use_Z_29             = 0
use_Z_30             = 0

iso_abundance_01_001 = 1.06e+06   H
```

```
iso_abundance_01_002 =     34.8
iso_abundance_02_003 =    9.033   He
iso_abundance_02_004 = 7.199e+04
iso_abundance_03_006 =        0   Li
iso_abundance_03_007 =        0
iso_abundance_04_009 =        0   Be
iso_abundance_05_010 =        0   B
iso_abundance_05_011 =        0
iso_abundance_06_012 =     2819   C
iso_abundance_06_013 = 5.268e-07
iso_abundance_07_014 =    182.8   N
iso_abundance_07_015 = 5.961e-05
iso_abundance_08_016 =     3822   O
iso_abundance_08_017 = 6.713e-07
iso_abundance_08_018 =    1.286
iso_abundance_09_019 = 2.664e-08   F
iso_abundance_10_020 =    312.5   Ne
iso_abundance_10_021 = 0.003556
iso_abundance_10_022 =    100.1
iso_abundance_11_023 =    22.84   Na
iso_abundance_12_024 =    658.1   Mg
iso_abundance_12_025 =     82.5
iso_abundance_12_026 =    104.7
iso_abundance_13_027 =    76.42   Al
iso_abundance_14_028 =    725.7   Si
iso_abundance_14_029 =    35.02
iso_abundance_14_030 =    24.68
iso_abundance_15_031 =    4.242   P
iso_abundance_16_032 =    89.12   S
iso_abundance_16_033 =   0.3056
iso_abundance_16_034 =    3.417
iso_abundance_16_036 = 0.0004281
iso_abundance_17_035 =   0.7044   Cl
iso_abundance_17_037 = 0.001167
iso_abundance_18_036 =    9.829   Ar
iso_abundance_18_038 =   0.6357
iso_abundance_18_040 = 0.001744
iso_abundance_19_039 =    1.389   K
iso_abundance_19_040 =    3.022
iso_abundance_19_041 = 0.0003339
iso_abundance_20_040 =    51.13   Ca
iso_abundance_20_041 =    1.974
iso_abundance_20_042 = 1.134e-06
iso_abundance_20_043 = 2.117e-06
iso_abundance_20_044 = 9.928e-05
iso_abundance_20_048 =   0.1099
iso_abundance_21_045 =    1.635   Sc
iso_abundance_22_046 =    5.558   Ti
iso_abundance_22_047 = 8.947e-06
iso_abundance_22_048 = 6.05e-07
iso_abundance_22_049 = 5.854e-09
iso_abundance_22_050 = 6.083e-07
iso_abundance_23_050 = 1.818e-05   V
iso_abundance_23_051 = 5.987e-09
iso_abundance_24_050 =    2.873   Cr
iso_abundance_24_052 =    8.065
iso_abundance_24_053 = 0.003014
iso_abundance_24_054 =   0.4173
iso_abundance_25_053 =    6.499   Mn
iso_abundance_25_055 =    1.273
iso_abundance_26_054 =    49.08   Fe
iso_abundance_26_056 =    697.7
iso_abundance_26_057 =    21.67
iso_abundance_26_058 =    3.335
iso_abundance_27_059 =    2.214   Co
iso_abundance_28_058 =    28.88   Ni
iso_abundance_28_060 =     11.9
iso_abundance_28_061 =   0.5992
iso_abundance_28_062 =    1.426
iso_abundance_28_064 =   0.3039
```

```
246
247 total_cross_section  = 2      total cross section option: 0=L83 1=WA96 2=BP01
248 cross_section_option = 012    100*i+j  i=1: use Heinbach-Simon C,O->B j=kopt j=11=Webber, 21=ST
249
250 t_half_limit         = 1.0e4  year - lower limit on radioactive half-life for explicit inclusion
251
252 primary_electrons    = 1
253 secondary_positrons  = 1
254 secondary_electrons  = 1
255 secondary_antiproton = 2    1=uses nuclear scaling; 2=uses nuclear factors by Simon2008
256 tertiary_antiproton  = 1
257 secondary_protons    = 1
258
259 gamma_rays           = 0    1=compute gamma rays, 2=compute HI,H2 skymaps separately
260 pi0_decay            = 0    1= old formalism 2=Blattnig et al.
261 IC_isotropic         = 1    1,2= compute isotropic IC: 1=compute full, 2=store skymap components
262 IC_anisotropic       = 1    1,2,3= compute anisotropic IC: 1=full, 2=approx., 3=isotropic
263 bremss               = 0    1=compute bremsstrahlung
264 synchrotron          = 0    1=compute synchrotron
265
266 comment              = the dark matter (DM) switches and user-defined parameters
267 DM_positrons         = 0   1=compute DM positrons
268 DM_electrons         = 0   1=compute DM electrons
269 DM_antiprotons       = 0   1=compute DM antiprotons
270 DM_gammas            = 0   1=compute DM gammas
271
272 DM_double0           = 2.8    core radius, kpc
273 DM_double1           = 0.43   local DM mass density, GeV cm-3
274 DM_double2           = 80.    neutralino mass, GeV
275 DM_double3           = 40.    positron width distribution, GeV
276 DM_double4           = 40.    positron branching
277 DM_double5           = 40.    electron width distribution, GeV
278 DM_double6           = 30.    electron branching
279 DM_double7           = 50.    pbar width distribution, GeV
280 DM_double8           = 40.    pbar branching
281 DM_double9           =3.e-25  <cross_sec*V>-thermally overaged, cm3 s-1
282
283 DM_int0              = 1      isothermal profile
284 DM_int1              = 1
285 DM_int2              = 1
286 DM_int3              = 1
287 DM_int4              = 1
288 DM_int5              = 1
289 DM_int6              = 1
290 DM_int7              = 1
291 DM_int7              = 1
292 DM_int9              = 1
293
294 output_gcr_full      = 0  output full galactic cosmic ray array if 1, only at earth for 0
295 warm_start           = 0  read in nuclei file and continue run
296
297 verbose              = 0  verbosity: 0=min,10=max <0: selected debugs
298 test_suite           = 0  run test suite instead of normal run
```

Appendix B

CR species list and the CR database

This Appendix lists the experiments and references included in the 11 Nov 2009 version of the CR database[1], maintained by Strong (2009), from which the data sets were taken for the corresponding CR species used in the parameter study in Section 6.3. Data sets marked with *, were not included in the parameter study, due to the lack of above 4 GeV.

CR database

Experiment	Reference	CR species
AMS01	Aguilar et al. (2002)	^{4}He
BESS	Sanuki et al. (2000)	
CAPRICE98	Boezio et al. (2003)	
IMAX	Menn et al. (2000)	
MUBEE	Zatsepin et al. (1994)	
SANRIKU	Kamioka et al. (1997)	Fe
JACEE	Asakimori et al. (1998)	^{4}He, C+N+O, Ne+Mg+Si, Fe
RUNJOB	Derbina et al. (2005)	
SOKOL	Ivanenko et al. (1993)	
ATIC2	Panov et al. (2007)	^{4}He, He, C, O, CNO, Ne, Mg, Si, Fe
CRIS*	ACE Collaboration (2003)	B, C, N, O, F, Ne, Na, Mg, Al, Si, P, S, Cl, Ar, K, Ca, Sc, Ti, V, Cr, Mn, Fe, Co
HEA03	Engelmann et al. (1990)	Be, B, C, N, O, F, Ne, Na, Mg, Al, Si, P, S, Cl, Ar, K, Ca, Sc, Ti, V, Cr, Mn, Fe, Co
CRN	Müller et al. (1991)	C, O, Ne, Mg, Si, Fe
	Swordy et al. (1993)	C+N+O, Ne+Mg+Si

[1] `http://www.mpe.mpg.de/~aws/propagate.html`

References

Abbasi, R., et al. (2010), Measurement of the anisotropy of cosmic-ray arrival directions with IceCube, *Astrophys. J. Lett.*, *718*, L194–L198.

ACE Collaboration (2003), *Online data: Galactic cosmic ray element spectra for solar minimum and solar maximum from CRIS*, `http://www.srl.caltech.edu/ACE/ASC/DATA/level3/cris/CRISminmax_spectra.txt`.

Aguilar, M., et al. (2002), The Alpha Magnetic Spectrometer (AMS) on the International Space Station: Part I - results from the test flight on the space shuttle, *Phys. Rep.*, *366*, 331–405.

Aharonian, F. A., et al. (2004), High-energy particle acceleration in the shell of a supernova remnant, *Nature*, *432*, 75–77.

Amenomori, M., et al. (2005), Large-scale sidereal anisotropy of galactic cosmic-ray intensity observed by the Tibet air shower array, *Astrophys. J. Lett.*, *626*, L29–L32.

Asakimori, K., et al. (1998), Cosmic-ray proton and helium spectra: results from the JACEE experiment, *Astrophys. J.*, *502*, 278–283.

Balogh, A., L. J. Lanzerotti, and S. T. Seuss (2008), *The heliosphere through the solar activity cycle*, 1st ed., 286 pp., Springer-Praxis, Berlin.

Berezinskii, V. S., S. V. Bulanov, V. A. Dogiel, and V. S. Ptuskin (1990), *Astrophysics of cosmic rays*, North-Holland, Amsterdam.

Bisschoff, D., I. Büsching, and M. S. Potgieter (2011a), Searching for signatures of nearby sources of cosmic rays in their local chemical composition, *Proc. 32nd ICRC, Beijing.*

Bisschoff, D., I. Büsching, and M. S. Potgieter (2011b), Searching for signatures of nearby sources of cosmic rays in their local chemical composition, *Proc. 56th SAIP Conf., Johannesburg.*

Boezio, M., et al. (2003), The cosmic-ray proton and helium spectra measured with the CAPRICE98 balloon experiment, *Astroparticle Phys.*, *19*, 583–604.

Burger, R. A., and M. Hattingh (1995), Steady-State Drift-Dominated Modulation Models for Galactic Cosmic Rays, *Astrophys. Space Sci.*, *230*, 375–382.

Büsching, I. (2004), On the time-dependent propagation of cosmic rays, Ph.D. thesis, Ruhr-Universität, Germany.

Büsching, I., A. Kopp, M. Pohl, R. Schlickeiser, C. Perrot, and I. Grenier (2005), Cosmic-ray propagation properties for an origin in supernova remnants, *Astrophys. J.*, *619*, 314–326.

Caballero-Lopez, R. A., and H. Moraal (2004), Limitations of the force field equation to describe cosmic ray modulation, *J. Geophys. Res.*, *109*, A01,101.

Cronin, J. W., T. K. Gaisser, and S. P. Swordy (1997), Cosmic rays at the energy frontier., *Sci. Am.*, *276*, 32–37.

Derbina, V. A., et al. (2005), Cosmic-ray spectra and composition in the energy range of 10-1000 TeV per particle obtained by the RUNJOB experiment, *Astrophys. J. Lett.*, *628*, L41–L44.

Engelmann, J. J., P. Ferrando, A. Soutoul, P. Goret, and E. Juliusson (1990), Charge composition and energy spectra of cosmic-ray nuclei for elements from Be to NI - Results from HEAO-3-C2, *Astron. Astrophys.*, *233*, 96–111.

Fahr, H. J., T. Kausch, and H. Scherer (2000), A 5-fluid hydrodynamic approach to model the solar system-interstellar medium interaction, *Astron. Astrophys.*, *357*, 268–282.

Ferreira, S. (2002), The heliospheric transport of galactic cosmic rays and jovian electrons, Ph.D. thesis, P.U. for C.H.E., South Africa.

Ferreira, S. E. S., M. S. Potgieter, and B. Heber (2003), Particle drift effects on cosmic ray modulation during solar maximum, *Adv. Space Res.*, *32*, 645–650.

Foukal, P. V. (2004), *Solar astrophysics*, 2nd ed., 466 pp., Wiley, Weinheim.

Gabici, S. (2008), Gamma ray astronomy and the origin of galactic cosmic rays, *Proc. 21st ECRS, Košice*.

Ginzburg, V. L., and S. I. Syrovatskii (1964), *The origin of cosmic rays*, 1st ed., 423 pp., Pergamon, Oxford.

Gleeson, L. J., and W. I. Axford (1968a), Modulation of galactic cosmic rays, *Astrophys. J.*, *154*, 1011–1026.

Gleeson, L. J., and W. I. Axford (1968b), The solar radial gradient of galactic cosmic rays, *Can. J. Phys.*, *46*, S937–S941.

Gleeson, L. J., and I. A. Urch (1973), A study of the force-field equation for the propagation of galactic cosmic rays, *Astroph. Space Sci.*, *11*, 288–308.

Gombosi, T. I. (1998), *Physics of the space environment*, 1st ed., 339 pp., Cambridge Press, Cambrige.

Han, J.-L., and R. Wielebinski (2002), Milestones in the observations of cosmic magnetic fields, *Chin. J. Astron. Astrophys.*, *2*, 293–324.

Hanslmeier, A. (2002), *The sun and space weather*, 1st ed., 243 pp., Kluwer, Dordrecht.

Hattingh, M. (1998), The modulation of galactic cosmic rays in athree-dimensional heliosphere, Ph.D. thesis, P.U. for C.H.E., South Africa.

Heber, B., and M. S. Potgieter (2006), Cosmic rays at high heliolatitudes, *Space Sci. Rev.*, *127*, 117–194.

Herbst, K., A. Kopp, B. Heber, F. Steinhilber, H. Fichtner, K. Scherer, and D. Matthiä (2010), On the importance of the local interstellar spectrum for the solar modulation parameter, *J. Geophys. Res.*, *115*, D00I20.

Ivanenko, I. P., V. Y. Shestoperov, and L. O. Chikova (1993), Energy spectra of cosmic rays above 2 TeV as measured by the "SOKOL" apparatus, *Proc. 23rd ICRC, Calgary*, *2*, 17–20.

Kamioka, E., et al. (1997), Azimuthally controlled observation of heavy cosmic-ray primaries by means of the balloon-borne emulsion chamber, *Astroparticle Phys.*, *6*, 155–167.

Kampert, K. H. (2007), Cosmic rays from the knee to the ankle status and prospects, *Nucl. Phys. B*, *165*, 294–306.

Krüger, T. P. J. (2005), The effect of fisk-parker hybrid magnetic field on cosmic rays in the heliosphere, Master's thesis, N.W.U., South Africa.

Langner, U. (2000), Effects of different local interstellar spectra on the heliospheric modulation of cosmic rays, Master's thesis, P.U. for C.H.E., South Africa.

Langner, U. (2004), Effects of termination shock acceleration on cosmic rays in the heliosphere, Ph.D. thesis, P.U. for C.H.E., South Africa.

Langner, U. W., and M. S. Potgieter (2004), Solar wind termination shock and heliosheath effects on the modulation of protons and antiprotons, *J. Geophys. Res.*, *109*, A01103.

Langner, U. W., M. S. Potgieter, and W. R. Webber (2003), Modulation of cosmic ray protons in the heliosheath, *J. Geophys. Res.*, *108*, 8039–8048.

Longair, M. S. (2004a), *High energy astrophysics: Volume 1, Particles, photons and their detection*, 2nd ed., Cambridge Press, Cambrige.

Longair, M. S. (2004b), *High energy astrophysics: Volume 2, Stars, the Galaxy and the Interstellar Medium*, 2nd ed., Cambridge Press, Cambrige.

Mashnik, S. G., A. J. Sierk, K. A. Van Riper, and W. B. Wilson (1998), Production and validation of isotope production cross section libraries for neutrons and protons to 1.7 GeV, *SARE 4 Workshop, Knoxville.*

Maurin, D., R. Taillet, and F. Donato (2002), New results on source and diffusion spectral features of galactic cosmic rays: I B/C ratio, *Astron. Astrophys.*, *394*, 1039–1056.

Menn, W., et al. (2000), The absolute flux of protons and helium at the top of the atmosphere using IMAX, *Astrophys. J.*, *533*, 281–297.

Moldwin, M. (2008), *An introduction to space weather*, 1st ed., 134 pp., Cambridge Press, Cambridge.

Moskalenko, I. V., and A. W. Strong (1998), Production and propagation of cosmic-ray positrons and electrons, *Astrophys. J.*, *493*, 694–707.

Moskalenko, I. V., A. W. Strong, J. F. Ormes, and M. S. Potgieter (2002), Secondary antiprotons and propagation of cosmic rays in the Galaxy and heliosphere, *Astrophys. J.*, *565*, 280–296.

Müller, D., S. P. Swordy, P. Meyer, J. L'Heureux, and J. M. Grunsfeld (1991), Energy spectra and composition of primary cosmic rays, *Astrophys. J.*, *374*, 356–365.

Nkosi, G. S., M. S. Potgieter, and W. R. Webber (2011), Modelling of low-energy galactic electrons in the heliosheath, *Adv. Space Res.*, *48*, 1480–1489.

Panov, A. D., J. H. Adams, H. S. Ahn, G. L. Bashindzhagyan, K. E. Batkov, et al. (2007), The results of ATIC-2 experiment for elemental spectra of cosmic rays, *Bull. Russ. Acad. Sci. Phys.*, *71*, 494–497.

Parker, E. N. (1958), Dynamics of the interplanetary gas and magnetic fields, *Astrophys. J.*, *128*, 664–676.

Parker, E. N. (1965), The passage of energetic charged particles through interplanetary space, *Planet. Space Sci.*, *13*, 9–49.

Potgieter, M. S. (1984), The modulation of galactic cosmic rays as described by a three-dimensional drift model, Ph.D. thesis, P.U. for C.H.E., South Africa.

Potgieter, M. S. (2008), Solar cycle variations and cosmic rays, *J. Atmos. Terr. Phys.*, *70*, 207–218.

Potgieter, M. S. (2011), Cosmic Rays in the Inner Heliosphere: Insights from Observations, Theory and Models, *Space Science Reviews, Online First*, pp. 1–12.

Potgieter, M. S., and U. W. Langner (2004), Heliospheric modulation of cosmic-ray positrons and electrons: effects of the heliosheath and the solar wind termination shock, *Astrophys. J.*, *602*, 993–1001.

Potgieter, M. S., and H. Moraal (1985), A drift model for the modulation of galactic cosmic rays, *Astrophys. J.*, *294*, 425–440.

Ptuskin, V. S., I. V. Moskalenko, F. C. Jones, A. W. Strong, and V. N. Zirakashvili (2006), Dissipation of magnetohydrodynamic waves on energetic particles: impact on interstellar turbulence and cosmic-ray transport, *Astrophys. J.*, *642*, 902–916.

Putze, A., L. Derome, D. Maurin, L. Perotto, and R. Taillet (2009), A Markov Chain Monte Carlo technique to sample transport and source parameters of galactic cosmic rays. I. Method and results for the leaky-box model, *Astron. Astrophys.*, *497*, 991–1007.

Putze, A., L. Derome, and D. Maurin (2010), A Markov Chain Monte Carlo technique to sample transport and source parameters of galactic cosmic rays. II. Results for the diffusion model combining B/C and radioactive nuclei, *Astron. Astrophys.*, *516*, A66.

Sanuki, T., et al. (2000), Precise measurement of cosmic-ray proton and helium spectra with the BESS spectrometer, *Astrophys. J.*, *545*, 1135–1142.

Scherer, K., H. Fichtner, R. D. Strauss, S. E. S. Ferreira, M. S. Potgieter, and H.-J. Fahr (2011), On Cosmic Ray Modulation beyond the Heliopause: Where is the Modulation Boundary?, *Astrophys. J.*, *735*, 128.

Schlickeiser, R. (2002), *Cosmic ray astrophysics*, 1st ed., Springer, Berlin.

Silberberg, R., C. H. Tsao, and A. F. Barghouty (1998), Updated partial cross sections of proton-nucleus reactions, *Astrophys. J.*, *501*, 911–919.

Stanev, T. (2004), *High energy cosmic rays*, 2nd ed., Springer-Praxis, Berlin.

Stix, M. (2002), *The sun: an introduction*, 2nd ed., 490 pp., Springer, Berlin.

Strauss, R. D. (2010), Modelling of anomalous cosmic rays, Master's thesis, N.W.U., South Africa.

Strong, A. W. (2009), *CR database*, `http://www.mpe.mpg.de/~aws/propagate.html`.

Strong, A. W., and I. V. Moskalenko (1998), Propagation of cosmic-ray nucleons in the Galaxy, *Astrophys. J.*, *509*, 212–228.

Strong, A. W., and I. V. Moskalenko (2001), Models for galactic cosmic-ray propagation, *Adv. Space Res.*, *27*, 717–726.

Strong, A. W., and I. V. Moskalenko (2006), *GALPROP C++ v.50: Explanatory supplement*, `http://galprop.stanford.edu/download/manuals/manual50.pdf`.

Strong, A. W., I. V. Moskalenko, and V. S. Ptuskin (2007), Cosmic-ray propagation and interactions in the Galaxy, *Ann. Rev. Nucl. Part. Sci.*, *57*, 285–327.

Swordy, S. P., J. L'Heureux, P. Meyer, and D. Muller (1993), Elemental abundances in the local cosmic rays at high energies, *Astrophys. J.*, *403*, 658–662.

Webber, W. R., and D. S. Intriligator (2011), Voyagers 1 and 2 in a shrunken and squashed heliosphere, *J. Geophys. Res.*, *116*, A06105.

Zatsepin, V. I., et al. (1994), Energy spectra and composition of primary cosmic rays in the energy range above 10 TeV per particle, *Phys. Atom. Nucl.*, *57*, 645–650.

Acknowledgements

I would like to express my gratitude to the following people and institutions for their assistance and support:

- Prof. M.S. Potgieter, my supervisor, for his guidance and expertise throughout this study and over the length of my tertiary education.
- Dr. I. Büsching, my co-supervisor, for teaching me everything I know about Astrophysics and his willingness to help with all problems that arouse in this study, even if it required frequent calls from halfway across the world.
- Dr. A. Kopp, for his insights and advice in writing this dissertation.
- Mrs. A. Burger, for evaluating the spelling and grammar of this work.
- Mrs. M.S. Sieberhagen, for administrative assistance.
- The High Performance Computing (HPC) Centre of the North-West University, for making their cluster available for the computing required throughout this study.
- The Center for Space Research for providing resources, facilities and financial support.
- The South African National Research Foundation (NRF) for partial financial support.
- My parents for their unconditional love and support over the past quarter century, and providing me with motivation when I needed it most.

Driaan Bisschoff
North-West University, Potchefstroom Campus
December 2011